12-2022

On Interpreting Eddy Covariance In Small Area Agricultural Situations With Contrasting Site Management.

Joel Oetting
joetting@vols.utk.edu

To the Graduate Council:

I am submitting herewith a dissertation written by Joel Oetting entitled "On Interpreting Eddy Covariance In Small Area Agricultural Situations With Contrasting Site Management.." I have examined the final electronic copy of this dissertation for form and content and recommend that it be accepted in partial fulfillment of the requirements for the degree of Doctor of Philosophy, with a major in Environmental and Soil Sciences.

Neal Eash, Major Professor

We have read this dissertation and recommend its acceptance:

Bruce Hicks, James Zahn, John Goddard, Dayton Lambert, Tom Sauer

Accepted for the Council:

Dixie L. Thompson

Vice Provost and Dean of the Graduate School

(Original signatures are on file with official student records.)

On Interpreting Eddy Covariance in Small Area Agricultural Situations With Contrasting Site Management.

A Dissertation Presented for the
Doctor of Philosophy
Degree
The University of Tennessee, Knoxville

Joel N. Oetting
December 2022

ABSTRACT

This dissertation examined the carbon sequestration potential of a low C:N soil amendment and its incorporation into the soil over a rolling agricultural field. A segmented planar fit was developed to assess and correct the systematic errors the topography introduces on the carbon dioxide fluxes. The carbon dioxide fluxes were then be partitioned into gross primary productivity and soil respiration to understand the influence of the contrasting management practices, using flux variance partitioning. Concomitant with the partitioning, high resolution temporal and spatial scale remote sensing images were interpolated and standardized to conduct hypothesis testing for treatment effects.

TABLE OF CONTENTS

LIST OF TABLES

LIST OF FIGURES

INTRODUCTION

Agricultural management practices are global sources for carbon dioxide emissions and nitrogen pollution. Carbon dioxide is a major global greenhouse gas and excess nitrogen fertilization significantly harms terrestrial and aquatic life. Quantifying carbon dioxide emissions for conventional agricultural practices is necessary to provide crop producers with recommended practices under a changing climate. While many farms exist on rolling (i.e., complex) landscapes, measuring field scale emissions on these regions are confounded by the topography.

Monitoring the environmental impact of common agricultural practices is challenging. Many measurement protocols require large amounts of destructive sampling or costly monitoring methods that can potentially influence the soil environment (such as soil chambers). The eddy covariance method overcomes these limitations by providing a nondestructive, direct measure of field scale net carbon dioxide exchange. However certain assumptions, such as horizontal topography, must be satisfied for the measurements to be deemed reliable. The eddy covariance (EC) method must be improved to account for systematic errors arising from complex topography.

The improved eddy covariance processing to account for nonuniform topography with a dynamic canopy can provide farmers and scientists reliable estimates on agricultural water use and carbon dioxide flux. This knowledge can then be used to support more sustainable agricultural management practices.

Justification for this study

We are living in the Anthropocene- a time period where nature is mostly under human influence. For example, by 2050 the global population will increase by 2.3 billion and global food demand is predicted to increase by 100%. Feeding the increased population will have to be met by land clearing and intensive use of croplands. About one-quarter of global greenhouse gas emissions result from land clearing, crop production and fertilization. The effect of fertilization further harms terrestrial and aquatic life. We must achieve greater yields while also having a lower environmental impact (Tilman et al., 2011). Increasing knowledge of how environmental variables and crop production practices affect yield is necessary to slow down our destructive logistics.

Agriculture and land use changes have accelerated the alteration of soil forming processes around the globe (Lin, 2011). The acceleration further degrades the soil's quality both as an economic and ecological service. Of major importance is soil organic matter (SOM). SOM greatly increases a soil's intrinsic resilience and further prevents increased soil degradation and enhances chemical, biological, and physical soil properties (Swift, 2001). Since the agricultural and green revolution, there have been two major inputs into the terrestrial biogeochemical cycle: carbon dioxide and reactive nitrogen (Vitousek et al., 1997). Agricultural practice is fundamentally about manipulating these cycles.

Outside of human alteration, photosynthesis is the ultimate source of soil organic carbon (SOC), and microbial fixation of dinitrogen gas is the source of soil N; the soil environment reduces or oxidizes these inputs whether acting as a sink or a source. Other N sources include atmospheric deposition and fertilizer inputs (Johnson et al., 1995). Changes in SOM occur due to the imbalance between carbon inputs, dead plant material, and outputs, mainly caused by decomposition, leaching, and erosion. Thus, a recommended approach for decreasing agriculture's impact on accelerating SOM decomposition is to reduce tillage. This disturbance reduction maintains the soil aggregate structure which protects SOM from microbial consumption (Johnson et al., 1995; Swift, 2001). Besides reduced tillage, there are other practices that could stabilize SOM. These methods directly control reactive nitrogen and carbon inputs. Such inputs include mineral fertilizers or organic soil amendments, and/or incorporation of crop residues. The effect of nutrient inputs and incorporation on the soil system will be the proposal's key investigation.

There is an intrinsic positive feedback process where assimilation of carbon dioxide occurs through photosynthesis and results in increases in soil carbon. For example, more soil carbon tends to increase carbon capture which then increases crop residue, and the process begins anew. Unfortunately, the feedback can also be negative because the loss of soil carbon not only emits carbon dioxide but increases the risk of less efficient crop growth (Lal, 2007). Enhanced SOC content promotes plant growth but paradoxically the crop yield is derived from the decay of SOC. A positive feedback of soil carbon on yield, therefore, may be most likely in previously C-depleted or degraded soils. Where incremental plant growth responses to soil carbon are greatest and benefits derive from mechanisms other than decay (Janzen, 2014).

Overview of Study

This study attempted to understand the impact of no-till and recently converted tillage systems and two different nitrogen inputs on a split plot maize field. Eddy Covariance will be used to monitor water vapor and carbon dioxide exchange for the different practices. Using micro-meteorological instrumentation, this research will measure water and carbon dioxide fluxes over an agricultural field with two different nutrient inputs and two different surface practices. The measured fluxes will then be partitioned into two sources: the soil and the crop system. Site heterogeneity and representatives of the measured fluxes were assessed with high resolution remote sensing. The study examined the effects on evaporation and transpiration. Specifically, the study examined how the treatments respond to stress (if it occurs), as well as crop productivity.
The study used EC systems to measure net ecosystem exchange (NEE) and evapotranspiration (ET) and differences across treatments will be quantified. The NEE will be partitioned into gross primary productivity (GPP) and ecosystem respiration (R_e) to give information on the carbon dioxide emissions from the soil and crop productivity. The partitioning procedure was accomplished with the

Scalon and Sahu (2008) partitioning method. Evaporation and transpiration were also quantified.

Site Description

The study area is located in Loudon County, TN. The approximately 20-hectare farm lies towards the outlet of Sweetwater Creek watershed. The climate is humid subtropical, influenced predominately by the gulf coast. The average annual temperature is 14.9°C and the average annual precipitation is 1290 mm. Eighty percent of the watershed is dominated by the soil order ultisols, followed by inceptisols (eleven percent) and alfisols (five percent). The soil series that dominate the site are Decatur (Fine, kaolinitic, thermic Rhodic Paleudult) and Emory (Fine-silty, siliceous, active, thermic Fluventic Humic Dystrudepts). Both soils formed in old valley fill material and residuum weathered from limestone. The site's mean elevation is 270 meters with a maximum elevation of 275 meters and a low of 262 meters. The average slope of the site is 3 ±3 % compared to the average slope of Sweetwater creek of 10 ±7 %.

Site Manipulation

This study investigated the effects of applying two soil amendments on an upland maize field analyzed with a split plot design. The first treatment will be typical (NPK) inorganic fertilizer. The second treatment will use the soil amendment TilthMax3G. This amendment is a biologically stable organic soil conditioner processed from organic fermentation inputs. The study also examined incorporating TilthMax3G with vertical tillage to 8 cm.

WHY EDDY COVARIANCE?

The eddy covariance (EC) method provides a nondestructive, direct measure of the flux density across an atmosphere-(agro)ecosystem interface. The fluxes measure the mass balance of vegetation and soil and how the ecosystem responds to environmental drivers and stresses. Information on trace gas fluxes is a variable quantification of ecosystem performance and health (Baldocchi, 2014).

Most studies of terrestrial-atmospheric exchange in the agricultural and ecological literature have relied on chamber techniques. These methods are inherently limited since they alter the local environment and are logistically difficult. Furthermore, it is difficult to run chambers for long-term, continuous measurements. Deploying enough chamber replicates to obtain statistically reliable results compounds the problems. Some of the logistical and statistical problems are solved with the use of micrometeorological techniques (Baldocchi, 2014; Baldocchi et al., 1988). Boundary layer turbulence transports the gases from the biosphere to the atmosphere. Micrometeorology provides alternatives to measure exchanges between the biosphere and the atmosphere. Micrometeorological techniques also have many advantages. First, they do not disturb the environment around the plant canopy. Second, these techniques allow continuous measurements. And third, time-averaged micrometeorological

measurements at a point provide an area-integrated, ensemble average of the exchange rates between the surface and the atmosphere. EC techniques are based on high-frequency measurements of three-dimensional wind speed, carbon dioxide and H_2O. In short, the EC method is an accurate, direct and defensible approach to measure gas fluxes (Baldocchi et al., 1988)
The EC system effectively measures net ecosystem exchange (NEE). NEE is a measure of net ecosystem production which quantifies the net accumulation of organic matter:

$$NEE = R_e + GPP$$

Were R_e (ecosystem respiration) is respiration from the heterotrophic and autotrophic sources and GPP is Gross primary productivity. While the NEE measures both plant and soil carbon dioxide exchange, inferring NEE as a direct measure of SOM decomposition is limited (Kuzyakov, 2006). While NEE yields a valuable measure of ecosystem carbon exchange, it does not describe the processes responsible for the flux. We can gain a greater (but not complete) understanding of different management practices' effect if we know how soil respiration and GPP are impacted. Because only some of the carbon dioxide exuded from the soil is produced by the decomposition of soil organic matter, measuring and partitioning the NEE will not yield information on whether the soil is a net source or sink.

Once the R_e and GPP are partitioned from the NEE, site managers will only have a broad understanding of soil respiration. Plants are the most important autotrophs contributing to carbon dioxide efflux from soil by root respiration. Since plant C sources frequently amount to more than half of the total soil carbon dioxide flux (Hanson et al., 2000; Larionova et al., 2003), the flux of plant-derived carbon dioxide masks the contribution of SOM-derived carbon dioxide when measuring carbon dioxide fluxes from planted soils.
Kuzyokov (2006) summarized five sources of respired Carbon Dioxide. The first source is basal respiration or microbial decomposition of SOM (distinct of plant remains) in root-free soil. Second, microbial decomposition of SOM in root affected or plant residue affected soil. Third, microbial decomposition of dead plant remains. Root exudates from living roots are also decomposed which contributes to the fourth source of Carbon Dioxide. The fifth source is autotrophic derived respiration or respiration from roots.

Only the first source- microbial decomposition of SOM in the root-free soil- contributes to the carbon dioxide flux containing organic matter. Because of their fast turnover times, the four other carbon dioxide sources, microbial decomposition of plant residues and root exudates, and root respiration, have no significant effect on C sequestration in the short or long-term. And it is only the respired SOM that contributes to long-term losses of soil C assuming residue application is constant (Kuzyakov, 2006). One approach is to partition total respiration from soil into root-derived carbon dioxide and SOM- derived carbon dioxide is assuming linear relation between root biomass and root-derived Carbon Dioxide. This method was first developed by Kucera and Kirkham (1971).

With the partitioning method finished we can then estimate the remaining sources of carbon dioxide that we can attribute to SOM and vegetation induced respiration. If the crop productivity and root biomass is relatively constant between treatments, the difference between respiration for untreated and treated plots will reflect difference in turnover of the various organic pools. Only incubation and isotope labeling experiments will be able to parse out the sources of the respiration. To put this in perspective, adding highly labile C and N sources will increase the soil respiration but this can be attributed to higher turnover rates of the microbial biomass leaving us to guess how much of carbon was derived from the SOM or the TilthMax3G™.

Effect of C and N Input

The priming effect was defined by Jenkinson (1966) as a positive or negative change in the decomposition rate of SOM caused by the addition of fresh organic matter (Jenkinson, 1966; Jenkinson et al., 1985). The priming effect can impact SOM decomposition rates from a 50 percent reduction to 380 percent increase. Priming effects at the global scale may control as much as 50 percent of the total carbon dioxide released from terrestrial ecosystems. Thus, the priming effect is emerging as a crucial mechanism in terrestrial ecosystems (Cheng et al., 2013).

There are three effects which adding nitrogen will have on SOM: decrease SOM, increase SOM, or have no effect on SOM. There is certainly enough evidence to support each of these pathways. In forest environments there have been various, conflicting results including increases, decreases, or unchanged rates in carbon sequestration (Bowden et al., 2004; Mo et al., 2006; Vose et al., 1995). There have been conflicting results in agricultural experiments as well. While long term studies involving organic and mineral fertilizers show a general increase in SOM, Kwon et al. (2017) found N additions increased the decay rate of SOM. Measuring short-term ecosystem responses to mineral and organic fertilizer will illuminate the coupling of C and N. This study will help to parse out the sensitivity of the priming effect to global environmental change particularly in anthropogenic N deposition. Overall, the priming effect emerges as a key mechanism in mobilizing and possibly stabilizing SOM, forming a key link between plant functions and soil functions in terrestrial ecosystems (Clemmensen et al., 2013; Jastrow et al., 2000).

The nitrogen priming effect has two mechanisms where nitrogen fertilizer alters SOM: (1) Nitrogen fertilizer may augment SOM by promoting plant growth and increasing degradation of recalcitrant material or (2) Nitrogen fertilizer may lead to enhanced loss of SOM by accelerating oxidation rates of crop residue and SOM (Ladha et al., 2011). Alternatively, there could be no effect because these mechanisms are not mutually exclusive. For example, nitrogen input enhances plant dark respiration, stimulates root respiration, and increases root biomass (Burton et al., 2004; Liljeroth et al., 1994). The root biomass growth increases the possibility for a net accumulation of SOM because the die off of

fine roots within aggregates can be protected. D. W. Johnson and Curtis (2001), conducted a meta-analysis of 48 global experiments and concluded that N addition was the only forest management practice with a clear positive effect on the soil organic carbon pool.

Decomposition of cellulose or other labile compounds in residue and SOM are stimulated by nitrogen addition. However more recalcitrant compounds of litter and SOM (such as lignin) are inhibited by nitrogen addition. Craine et al. (2007), argued N additions lower decomposition rates of residue. This follows from the “microbial nitrogen mining” hypothesis. Microbes use labile C to decompose recalcitrant organic matter to acquire N. Thus, ecosystem C storage would increase with greater N availability because mining of recalcitrant C for N is suppressed. This might explain observed declines in decomposition with N addition. Increasing N availability, whether through fertilization or residue N content will have no effect on the size of the labile C pool but would decrease the rate of decomposition of recalcitrant C (Craine et al., 2007). If there is higher nutrient resource availability, both plants and microbes will be less dependent on each other’s strategy, thus reducing priming intensity. This prediction is partially supported by the common decrease in soil respiration upon N fertilization in forests (Cheng et al., 2013).

How does inorganic versus organic nutrient effect nutrient cycling? There have been many studies comparing the effect of organic versus inorganic N inputs. The organic inputs studied are typically cattle manure. Manures have a greater effect on increasing SOC and soil N and improving soil physical properties. While manured soils tend to have higher SOC contents, the mineral fertilizers do not lessen the SOC content (Meng et al., 2005). Monaco et al., (2008) found agricultural soil treated with different organic materials increased SOM and N-supplying capacity and potential soil respiration compared with inorganic or unfertilized soil. Diacono and Montemurro (2010) reviewed many long-term experiments. They found that long-lasting applications of organic amendments increased organic carbon up to 90 percent versus unfertilized soil and up to 100 percent versus chemical fertilizer treatments. Nardi et al., (2004) found forty years of manure fertilization improved the recalcitrant humus production. And, of course, the Rothamsted experiment is the longest running manure application study successfully showing the buildup of SOC (Jenkinson and Rayner, 1977). On the contrary, the absence of organic fertilizer inputs determined the opposite, producing more non-complex and lightweight humus. On shorter time scales Lazcano et al. (2012), found uncomposted manure (more labile C) increased microbial activity. Manure amended soils exhibited higher microbial activity than the inorganic fertilizer treatment. This higher activity maintains the supply-capacity for inorganic N and P compared to inorganic fertilizers. Ladha et al. (2011) found inorganic fertilizer significantly reduced the rate at which SOM is declining in agricultural soils. The authors did not support the conclusion that inorganic fertilizer caused the decrease in SOM. It appears organic fertilizer prolongs the supplying capacity of nutrients and on a longer time

scale increases SOM. There is further need to understand both responses to typical fertilizers and organic soil amendments. From the above we can hypothesize that application of TilthMax3G could mitigate SOM loss while potentially increasing it. Paradoxically higher emissions could be observed due to higher microbial turnover rates and plant production.

SITE ACTIVITIES SUMMARY

The site was first vertically tilled in June 2017 and again in the fall (November) see table. TilthMax3G was applied in the May 2016, June 2017 and December 2017. After a soil sampling a campaign, the fall of 2017, found water extracted pH than 1.5 pH units less than the conventional farmer practice. This is most likely due to the decomposition of the amino acids (see Fig. 1). While there were continuous flux measurements, two time lapse cameras were oriented to monitor crop and agro-ecosystem phonology [WCT-00122 TimelapseCam, Wingscapes Alabaster, AL]. Digital repeat photography has become a useful method for ecological and agricultural applications due to its low cost and maintenance and high-resolution data in red, green, and blue (RGB) channels. Digital cameras used for phenology observation have improved the detection of leaf phenology dynamics and crop emergence and vegetative stages through the analysis of RGB color changes over time. Digital repeat photography provides several clear advantages over human observations of phenology because of the ability to collect automatically repeated images at high temporal resolution (daily or hour scale) and wider spatial scales. From this Green Chromatic Coordinate (GCC) can be calculated:

$$GCC = \frac{\text{Green}_{DN}}{\text{Red}_{DN} + \text{Green}_{DN} + \text{Blue}_{DN}}$$

Where *Red* $_{DN}$, *Green* $_{DN}$, and *Blue* $_{DN}$ are the red, green, and blue color channels respectively. The trail camera represents the color as digital numbers (DN) stored in the high resolution (8 MGP) JPEG format. Figure 2 illustrates the behavior of GCC over the two years of measurement. GCC is the most reliable index to monster plant phenology from time lapse photography (Klosterman et al., 2014). The figure also illustrates the behavior significant events denoted in table 1. GCC has been shown to reduce noise to highlight the phenology signal (Burke and Rundquist, 2021). Vertical tillage was applied twice to the field in 2017, except for a small strip running on both sides of the soil amendment treatments. The strip changed in size during both events by about 0.6 hectares See Fig. 3. The areas of SMB and FP remained the same during the experiment 8.38 and 10.03 hectares. The no till strip was 1.87 and 2.51 hectares.

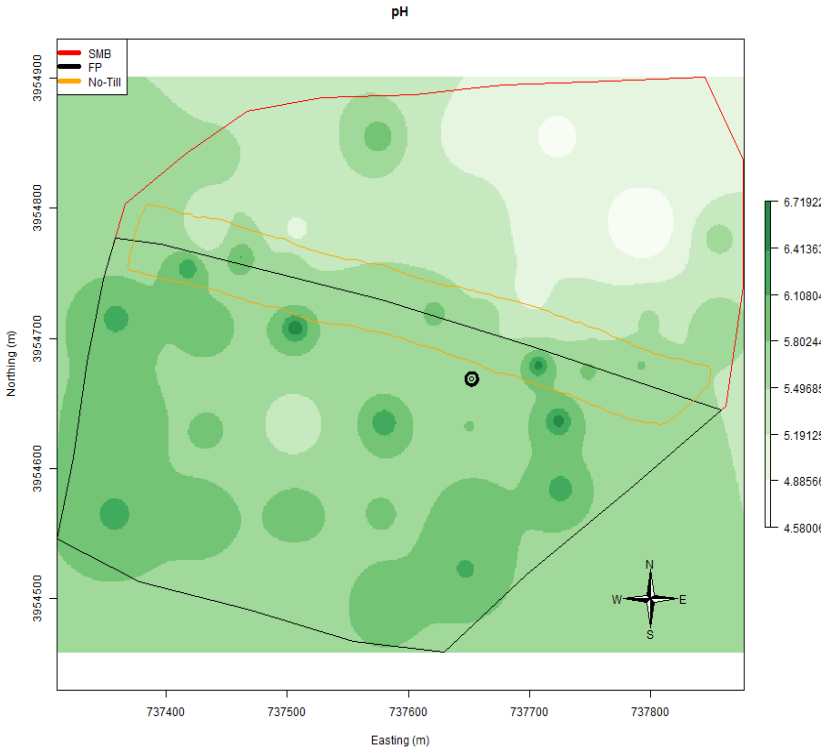

Figure 1. Interpolated site pH fall of 2017 after harvest. Note the low pH values towards the north where the TilthMax3G was applied.

Table 1. The table summarizes the events occurring on the site from 2017 to 2018.

TIMESTAMP	EVENTS
4/19/2017	BUSH HOGGED
5/30/2017	Roundup/atrazine herbicide
6/12/2017	First application TilthMax3G
6/13/2017	Second application TilthMax3G
6/14/2017	THIRD application TilthMax3G
6/15/2017	FOURTH Application TilthMax3G, TURBOTILLED, 100-40-80 applied
6/16/2017-6/17/2017	PLANTING
6/21/2017	VE
7/20/2017	top dressed
8/12/2017	VT
11/15/2017	Harvest
12/4/2017	SMB applied
12/13/2017	TILLED
4/2/2018	2 tons lime applied
4/30/2018	Roundup/atrazine herbicide
5/10/2018	100-40-80 applied
5/21/2018	Planting
5/27/2018	VE
7/12/2018	VT
10/30/2018	South Field Harvested
11/03/2018	North Field Harvested

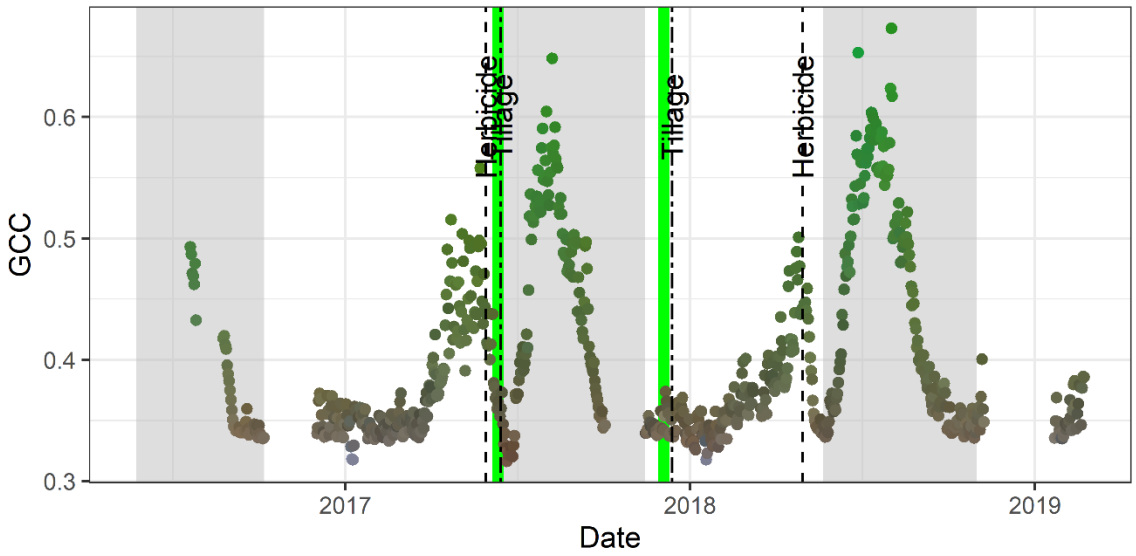

Figure 2. GCC trends over time. The grayed areas correspond to the maize planting season. The green lines correspond to the application of TilthMax3g. The die off with the application of herbicide can be clearly seen.

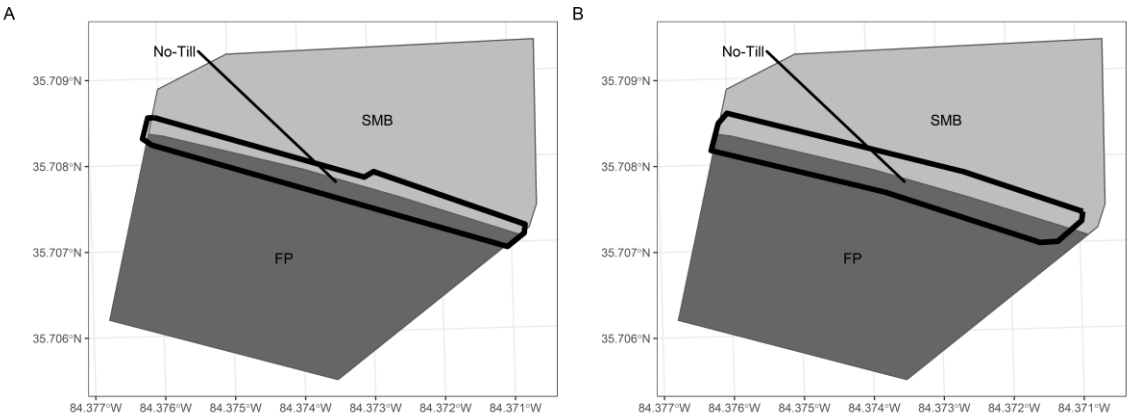

Figure 3. Site Treatments for both tillage treatments. A tillage event occurred on 6/15/2017 and B occurred 12/13/2017 where the No-Till area increased by 0.6 Hectares. SMB is the location of TilthMax3G and FP in darker gray is farmer practice.

CHAPTER 1
DEVELOPING A SEGMENTED PLANAR FIT FOR IMPROVED EDDY COVARIANCE COORDINATE ROTATION

Abstract

This chapter illustrates the practicality in a model based recursive partitioning algorithm for finding optimal criteria to understand the strengths and weaknesses of coordinate rotation methods. The algorithm as helpful to create individual wind sectors and accounting for variables that may impact the fits. The MOB algorithm was crucial to find what variables have the largest effect on combining or switching different parametric models; the variables with the largest explanatory power are *DOY*, solar altitude and wind direction (for the planar fit). Furthermore, the double rotation has deleterious effects in stable conditions and assigns incorrect CO_2 fluxes. Thus, even in rolling landscapes, using the unrotated fluxes or more complicated rotation methods such as the planar fit is preferable to double rotation.

Introduction

The eddy covariance (EC) method provides a non–destructive, direct measure of the flux density across an atmosphere–ecosystem interface. Measurement of the fluxes enables the mass balance of quantities like CO_2 to be inferred, along with guidance regarding an ecosystem's response to environmental drivers and stresses (Baldocchi, 2014). However, quantification of the fluxes involves consideration of measurement difficulties that are often not recognized or addressed. Although eddy covariance measurement can be taken as a precise evaluation of what a crop surface is experiencing, the method is fundamentally statistical and yields estimates of average fluxes. The statistical uncertainties involved are consequently readily estimated. It is rarely warranted that field studies support the expectation that any half–hour flux quantification possesses a standard error of less than 10% with (Hicks and Baldocchi, 2020). Moreover, there are fundamental questions that remain unanswered, such as how should eddy covariance instruments be erected regarding momentum and scalar flux variables and how should the sensor outputs be analyzed.

In the context of such questions, water vapor is a problematic variable. As water vapor is buoyant, the average water vapor flux of interest is influenced by gravity. Interpretation of fast–response observations should therefore be such that measurement coordinates are adjusted so that the derived evaporative eddy flux is oriented with respect to the gravitational normal. On the other hand, the flux dominating meteorological thinking is usually that of momentum (the drag upon the surface imposed by the wind) and is therefore physically tangential to the surface (Lee et al., 2004). For the present, note that meteorologists tend to rotate their anemometer's internal coordinate system so that the flux of momentum is (correctly) normal to the planar tangent to the local surface. In many applications, it is assumed (often without explanation) that the same reference plane applies for determination of the rate of evaporation from a crop. This paper will explore the uncertainties that arise by examining flexible

coordinate systems that can change as prevailing circumstances change, especially atmospheric stability and wind direction.

This paper addresses the practicality of using coordinate rotation methods to analyze data obtained over a rapidly changing canopy, with varying height of eddy covariance measurement. Consideration is given to the potential need for separate tangent planes for differing atmospheric conditions. For example, during highly unstable conditions the daytime convective fluxes (of sensible heat and water vapor) are expected to be largely independent of the slope of the surface and the only correction needed to the reference frame could be due to slight inconsistencies of the anemometer relative to gravitational normal and to any obstruction caused by the instrumentation.

To help answer these questions, many coordinate rotation models will be examined. In particular, a recursive model-based partitioning procedure (MOB) will be used to account for changes in instrument height, wind speed and atmospheric stability during the duration of the experiment (from January 2017 to January 2019) and to examine how different planar fits over subsets of the data offer opportunities to account for changes as the crop grew. The method of differently segmented planar fits with subsets that can vary in size over different environmental and/or experimental conditions will be denoted the recursively partitioned planar fit or RPF.

The intent is to develop an optimal coordinate rotation system that changes through the year as the crop height changes. Using this system, the goal is then to derive improved estimates of the fluxes of water vapor and carbon dioxide, these being the quantities of main interest in the context of crop productivity.

Coordinate Rotation

The central requirement in eddy covariance measurement is that the average vertical velocity is zero. This can be accomplished by any of many methods, first among which was the original use of a “brute force” approach, requiring that covariances accumulated over a particular sampling period be corrected on the basis of average values derived simultaneously. (Here, the issues that arise when it is assumed that the required average is that of air rather than the velocity of it will be ignored. That is, the emphasis is on making $\overline{w} = 0$, not on making $\overline{\rho w} = 0$ where ρ is air density and w is the vertical wind velocity with the overbar denoting a time average; (q.v. Lee et al. (2004)). In later developments, the requirement that $\overline{w} = 0$ was met by the simple expedient of imposing a high-pass filter on the analog w signal. With the advent of digital computing, these simple approaches evolved into coordinate rotation methods using post-event analysis of recorded fast-response data streams.

The most common coordinate rotation methodology now used considers observations obtained over a defined block of time (a “run” is typically fifteen to thirty minutes). A first rotation orients the x-axis along the direction of the mean wind. A second rotation ensures that the average vertical velocity is zero. This

method is often called the double rotation method (DR). The DR method is a simplification of the methodology developed by Wesely (1970) who was challenged by the requirement to extract robust eddy covariances from the outputs of pressure-sphere anemometers on a run-by-run basis. In the Wesely approach, a third rotation was invoked to drive the covariance $\overline{u'v'}$ (where u' and v' are the longitudinal and lateral wind velocity deviations) to zero.

An alternative approach examines, by linear regression, how ensembles of observations made over a longer period can be used to correct the wind statistics and to ensure that the vertical wind averages out to zero. A crucial difference between this planar fit (PF) methodology (q.v. Wilczak et al. (2001)) and the DR methodology discussed above is that the planar fit uses large amounts of data for the fit while the DR method considers the turbulence statistics within a single measurement period. By choosing a coordinate system averaged over a large length of time, the PF procedure avoids problems with large tilt angles in low wind speed conditions (Wilczak et al., 2001). Planar fit and its related methods are important to use in complex terrain, where the velocity normal to the tangential plane will not always align with gravity while the fluxes of buoyant properties must necessarily be influenced gravitationally.

In nonideal terrain with a rapidly changing canopy, a single plane is not the best system to use. A sector planar fit method was introduced by (Mammarella et al., 2007), to account for variations in the coordinate plane as a function of wind direction. However, this method involves splitting the data into sectors and leads to discontinuities at the boundaries between planar sectors (Ross and Grant, 2015). An alternative method fits a bivariate regression on the three average velocities such that, $\bar{W} = b_0 + b_1\bar{U} + b_2\bar{V}$ (Wilczak et al., 2001) and applies this to correct all measurements of the vertical velocity. There are several variations on this method. All of these considerations affect the installation of instruments at any test area being considered.

There is continuing debate about whether three-dimensional sonic anemometers should be installed with alignment to gravity or normal to the plane of local streamlines. As already mentioned, during unstable conditions, water vapor and carbon dioxide fluxes are primarily associated with the virtual heat flux which is aligned with gravity. In contrast, in stable conditions the gases will be transported by momentum exchange and a more appropriate “vertical” would be normal to the plane of the mean streamlines. In many field applications, consideration of coordinate rotation is complicated further when the height of the sensors is changed to maintain an appropriate distance above a rapidly growing crop. In the field experiment of interest here, the crop was maize.

Whereas conventional multiple regression or regression tree analyses can be used to determine the appropriate zero plane and relevant coordinate rotation for many experimental situations, the changing of sensor height and the use of several sonic anemometer systems with different configurations and deployments impose the need to account for changes resulting from “categorical” modifications of the set of observations such as changes in the height of

measurement of covariances. The addition of such a categorical variable examined here complicates the use of such standard methodologies. The partitioning process utilized here (e.g., Hothorn et al. (2006)) permits an opportunity to extract statistically optimal representations of the data, even when such categorical changes are included. The process as utilized here permits extraction of a best-fitting statistical “model” describing observations including categorical data, in a way that includes considerations of parsimony.

Data source

The experimental situation of relevance here is complicated by the changes in sensor height required to maintain adequate separation from the growing crop and the use of different sonic anemometer systems with different configurations and deployments. Observations were made at an experimental field location in Loudon, Tennessee (-84.374°, 35.708°), carrying a crop of maize (*zea Mays*). Figs. 4a and 4b depict the local topography and variation in local slope, respectively. Site locations are shown in Fig. 5. The study started June 2016 and concluded January 2019. Continuous eddy covariance measurements were made at three locations, at heights that were changed as the crop grew so as to maintain an average instrument height from the canopy — 1.5 to 2 m. The wind direction was unimodal; constrained by the ridge and valley orientation (see Fig.5). At two locations (stations 1 and 2), conventional Bowen ratio energy balance (BREB) measurements were made, supported by downward-looking infrared thermometers. Eddy flux towers were set up at three locations (stations 3, 4 and 5, as indicated in Fig. 4). Station 3 was fitted with an open path H_2O and CO_2 measurement system [LI-COR 7500 Biosciences, Lincoln, NE], accompanied by an RM Young 8100 sonic anemometer [R. M. Young Company, Traverse City, MI]. The RM Young anemometer was oriented, so the supporting mast was to the Northwest, normal to the prevailing wind direction. Stations 4 and 5 employed integrated open path gas analyzers and sonic anemometers [IRGASON Campbell Scientific, Inc., Logan, UT]. The IRGASONs were orientated into the dominant wind direction, from 225°.

The dataset now considered extended without interruption for 19 months, encompassing two complete growing seasons of the maize crop. Weekly adjustment of the height of the BREB and covariance instrumentation ensured that measurements were made at the design levels above the canopy – at about 0.5 m and 2 m in the case of the BREB instrumentation at sites 1 and 2 and about 1.5 m above the top of the canopy for the covariances at sites 3, 4 and 5. Figure 6 shows the changes in crop height through the two seasons now considered and the heights of operation of the covariance sensors yielding the observations used in the analysis to follow.

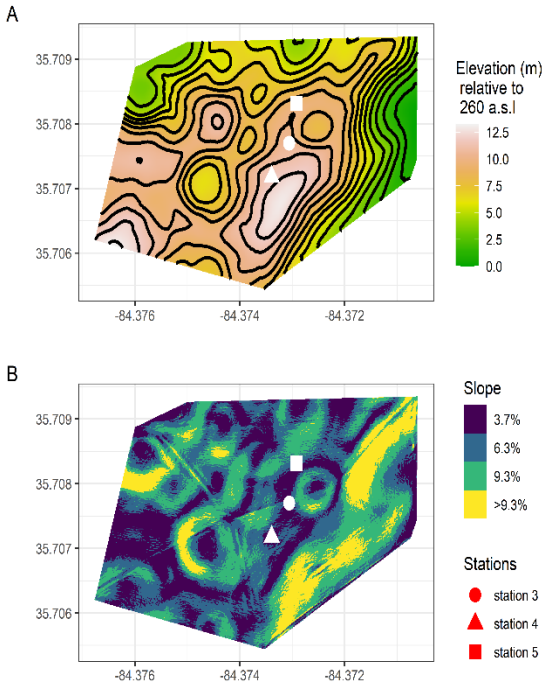

Figure 4. The range of elevations for the field and the percent slope. Note how the stations (as identified in red) are close to relatively steep areas.

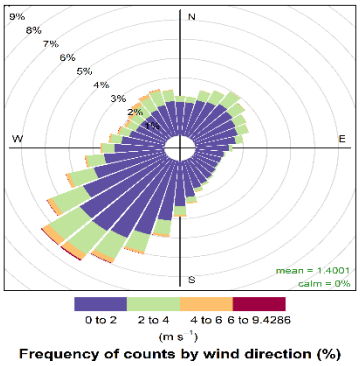

Figure 5. Wind rose showing two years of wind speed and direction as reported by the three eddy covariance systems.

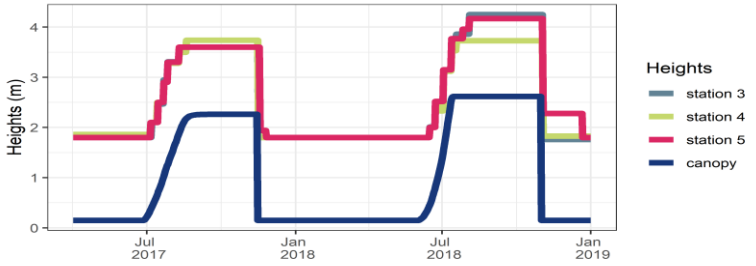

Figure 6. Instrument and Canopy heights. Canopy heights in the vicinity of the measurement locations were measured weekly.

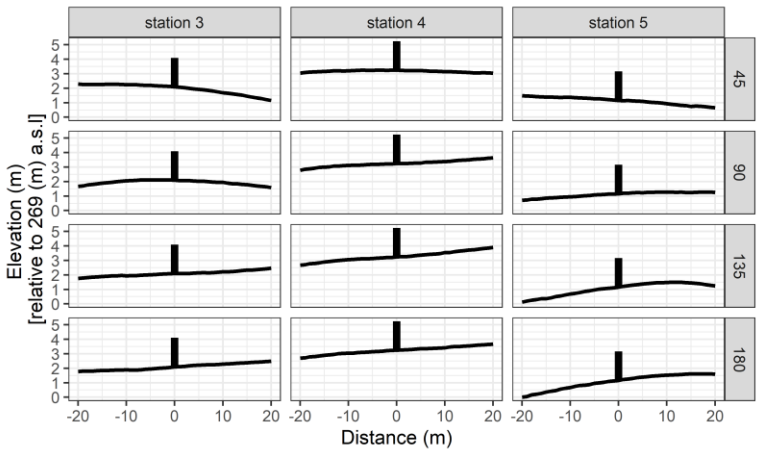

Figure 7. Elevation profiles for each station (columns) for various bearings (rows). The vertical exaggeration is 5 to 1; positive distance corresponds to the labeled bearing. The station heights are to scale with the different line thickness indicating minimum.

Figures 7 and 4 shows that the local slopes were such that the influence of gravity flow (especially at night) could not be ignored. Inspection of Fig. 4a indicates that nocturnal drainage flows would be expected to be strongest for sites 4 and 5, from about 135 deg. for both locations. Station 3 would likely experience milder downslope flow, in this case from about 45 deg. To emphasize the importance of considering this feature in the context of the coordinate rotation to be discussed below, Fig. 7 presents examples of local slope along four 45 deg. axes aligned according to the dominant wind direction. The slopes evident in the diagrams are exaggerated by a factor of five.

The various site complexities provide an opportunity to test familiar and conventional coordinate rotation methods and to investigate a way to overcome introduced subjectivity by applying the model–based recursive partitioning (MOB) approach (Zeileis et al., 2008). In essence, the MOB procedure involves repeated examinations of how different combinations of influential variables can be combined statistically, to minimize the unexplained variance in the flux that is associated with the best "*model*" so prescribed. MOB provides an ordered way to conduct what is basically an extended multiple regression examination of a collection of data and then to identify the most appropriate result from the many *models* so derived. In particular, the MOB process uses an objective methodology to identify the optimum result from among the numerous *models* that are developed. (Here, italicized *model* is used to provide clear distinction of the present result of statistical regression from the numerical models that are otherwise familiar, the latter being numerical simulations bringing together understanding of the processes involved.) The resulting *model* has then been subjected to procedures designed to ensure that it is parsimonious, rigorous, reproducible and easily interpretable.

Model–based Recursive Partitioning

In the specific context of interest here, involving the optimization of coordinate rotation required to analyze data obtained in studies of a growing crop of maize, the more modern MOB procedure uses raw data to derive a description of streamlines that is then used to correct the coordinate system. Accounting for local slope of the terrain can be accomplished with several alternative refinements, such as consideration of differences according to wind direction, on the basis of which a planar fit results (Wilczak et al., 2001). Rapid crop growth and the use of different measurement systems introduce additional complexities. Model–based recursive partitioning, an extension of familiar classification and regression tree analyses (Zeileis et al., 2008), offers an opportunity to progress. The MOB procedure finds subsets of the data in which a parametric model is best fit. The subsets are defined by finding ranges or categories of explanatory variables here called partitioning variables for example, wind speed, wind direction, solar altitude, atmospheric stability, height of measurement and sensor

used. The last two of these quantities introduce the need to consider different kinds of data — continuous, ordinal and categorical.

The MOB process is a synthesis of theory–based and data–driven (i.e., machine learning) approaches. The immediate benefit is that a theory–driven parametric description of the available observations model can be incorporated into a recursive partitioning algorithm based on multiple regression when categorical variables are included. The algorithm checks whether other interactions or variables that do not have strong contributions would alter the parameters or formulation of the final product. The analytical process is detailed by Kopf et al. (2013) and in the original paper by (Zeileis et al., 2008).

To quickly illustrate the parametric model needed to be fitted to correct for a proper coordinate rotation system, an initial regression is of $\bar{w}$ on $\bar{u}$ and $\bar{v}$. In other words, the initial parametric *model* needed to calculate the parameters for the planar fit rotation matrix is fitted to the entire range of observations. Residuals are calculated as $\overline{w} - \hat{w}$ where $\hat{w}$ is the predicted vertical velocity. The analysis considered at present is structured to minimize the sum of squares of these residuals: $\Sigma(\overline{w} - \hat{w})^2$; this sum is the present realization of the relevant "objective function" discussed in the foundational literature as identified above. A next step is to select which of the remaining contributing properties should now be considered.

Thus, it is of interest to find out whether the parametric model parameters are stable with respect to each partitioning variable. This is determined by testing for structural stability by ordering the estimation function by the order of each of the partitioning variables using a structural SupLM test for continuous partitioning variables (q.v. Hansen and Seo (2002)). The estimating function that identifies this partitioning is the derivative of the objective function with respect to the parameter considered (see Zeileis (2006)). After ordering according to the partitioning variable the cumulative sum is taken of the estimation function. If there is no structural change in the resulting sequence of values, there will be no change points. The strength of the change points can be compared with other potential partitioning values and corresponding *p*-values can be computed (Zeileis and Hornik (2007)). The strongest change point found will then later be used to define a cut point within a variable. The decision whether the partitioning variable with the lowest *p*-value is selected for splitting the data. If the variable being considered is unordered and categorical, all combinations need to be tested against each other.

The procedure is continued until no more statistically significant cut points can be determined, or until imposed constraints are attained (e.g., the number of data points remaining for statistical examination is too small or the number of nodes becomes excessive). There will be several terminal nodes, each corresponding to a path through the "tree" of nodes and branches.
For every terminal node, there will be a parametric *model* corresponding to the imposed planar fit result: $\bar{W} = b_0 + b_1\bar{U} + b_2\bar{V}$. To find the conditions for which a specific parametric *model* is applicable requires consideration of all of the nodes

leading to the terminal node in question. For example, given an arbitrary 30 minutes to calculate a flux, partitioning variables are identified, and the relevant parametric model is chosen.

In the present application, the originating data were averaged into thirty–minute periods and detrended by running average. The fluxes were corrected using a spectral correction factor by comparing the measured cospectrum with an analytical cospectrum (Moncrieff et al. (1997)) and compensated for density fluctuations following Webb et al. (1980). The data were then quality controlled by following the statistical tests and screening of Vickers and Marht (1997). For the MOB fitting procedure, outliers were identified and excluded when the pitch angle (ϕ) angle departed by more than 10° from a 99-point running median after sorting by wind direction. Furthermore, extreme wind speeds of the lower and upper quantiles (2.5%, 97.5%) were removed as well as friction velocities less then $0.05\ m\ s^{-1}$. Unlike past examinations, the observations were not confined to neutral stability regimes.

Nominations of partitioning variables

The first partitioning variable is choice of five stability regimes that will act as a categorical variable. The stability parameter $\frac{(z-d)}{L}$ was aggregated into five classes following the categories found in Dupont and Patton (2012). The stability regimes were defined after inspection of momentum and heat covariance as functions of the stability parameter $\frac{(z-d)}{L}$. Where d is the estimated displacement height and z the height of the anemometer. L is calculated according to its definition:

$$L = -\frac{\rho c_p T_p u_*^3}{\kappa g H_v}$$

where H_v in this context is the virtual heat flux, ≈ (H + LwE/14). T_p is the potential temperature (K), $\kappa = 0.41$ is the von Kármán constant $g = 9.81$ m s^{-2} is the acceleration due to gravity and c_p is the specific heat of air at constant pressure. Strong convection (SC) is characterized by large heat flux with low momentum flux while stable conditions have constant but low negative heat covariance ($\overline{w'T'}$) and near-zero momentum covariance ($\overline{w'u'}$). The boundaries for these conditions were determined subjectively by inspecting aggregated graphs of $\overline{w'T'}$ and $\overline{w'u'}$ as shown in Fig. 8. The boundaries for strong convection were defined as: $-100 < \frac{(z-d)}{L} \leq -0.45$, moderate convection (MC) $-0.45 < \frac{(z-d)}{L} \leq -0.03$, near neutral (NN) $-0.03 < \frac{(z-d)}{L} \leq 0.007$, transition to stable (TS) $0.007 < \frac{(z-d)}{L} \leq 0.56$ and stable (S) $0.56 < \frac{(z-d)}{L} \leq 100$.

There are many issues arising in the quantification of stability, mainly since its quantification is affected by the imposed coordinate rotation.

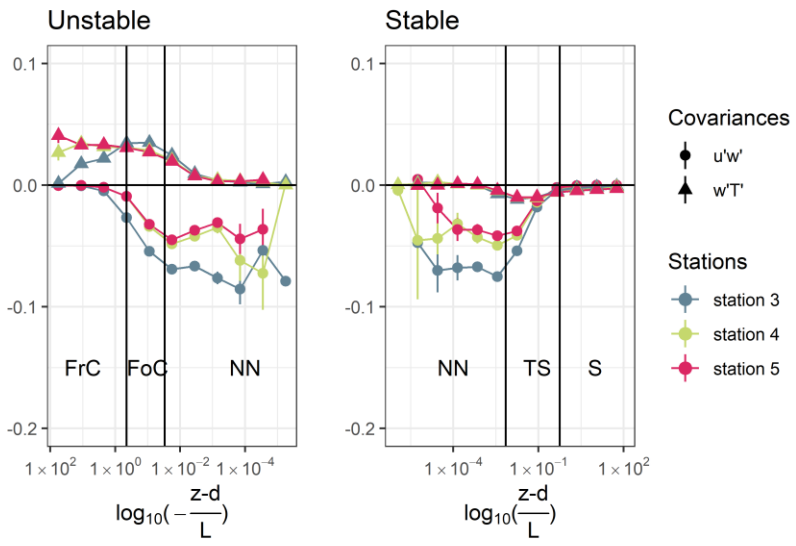

Figure 8. Five proposed stability regimes. The triangles indicate w'T' (K m s-1) while the circles indicate w'u' (m2 s-2). As these values are calculated from the initial DR one can see offset of w' u' as it does not approach zero. MC-Moderate Convection

To help understand the physical behaviors involved, an alternative to the stability categories described above has been tested, based on solar altitude and therefore independent of sonic anemometer orientation. Thus, solar altitude is the second partitioning variable. The data indicate that this can capture the diurnal stability extremes provided use is made of wind speed as a complimentary partitioning variable. It is possible that the recursive procedure could identify different direction segmentations independently of the coordinate reference frame.

In the discussion to follow, results from using these two stability classifications will be compared. Also examined will be the consequences of changes in the heights of the sonic anemometers. The assumption that different planar fit models are needed whenever the sonic anemometers are raised or lowered will be investigated to see if the fit is improved or if *models* can be aggregated across different height regimes. Using height regimes further simplifies and speeds up the recursive analysis procedure. This speed up happens because the height regimes are also categorical data.

Another important partitioning variable is wind direction. In isolation of other partitioning variables finding separate planar fits for various segments of the wind will be identical to the sector-wise planar fit procedure. Except as opposed to finding separate wind sectors educated guesses, the MOB can find separate wind sectors statistically and allow them to vary in size over time. Which leads to the final partitioning variable considered here is time — simply taking the day of year aggregated into six-hour periods.

Sorting of pitch angles $(\phi)\ defined\ as{:}\ \phi = \text{atan}\left(\frac{\overline{w}}{\overline{u}}\right)$ according to these stability regimes revealed a similar pattern, except for stable conditions and free convection. These two mechanically different regimes are similar in that they have the lowest wind speeds. The effect of buoyancy during unstable regimes on the ϕ angle is expected to be relatively independent of the surrounding topography but close inspection of the measurements indicates otherwise. (In comparison, studies of surface energy budgets in mountainous terrain have shown that differential solar heating associated with changes in local slope is an issue.) The aggregated pitch angles have different dependences on stability, wind speed and wind direction, perhaps partially due to differences in construction of the sonic anemometers and/or differences in their deployment. Regardless of this uncertainty, the role of stability must be included as a potential causative factor in the MOB procedure.

Measured pitch angles are illustrated in Fig. 9. A striking feature of Fig. 9 is that the results derived from the sonic anemometer used at site 3 differ from those from sites 4 and 5 (see above for the models). It is unknown whether the differences evident in Fig.9 relate to this difference on construction and exposure or to some other cause specific to the manufacturer. The data now obtained emphasize the need for careful assessment of anemometer performance, taking the results of detailed examinations (such as by Kochendorfer, (2012)) into account. It must be noted, however, that the anemometers deployed at sites 4

and 5 were erected on cross arms pointing into the predominate wind direction and that their bulk would have caused an updraft to be detected regardless of the wind direction (due to the imposed streamline deformation). The finding of about -10 degrees pitch for these two systems (Figs. 9) is compatible with this deformation expectation but appears more than would be expected. The current dataset is not adequate to test this further. Certainly, the anemometer at site 3 was not so affected.

Below 1 m s^{-1} wind speed the pitch angles derived from raw data exceed five degrees, but all anemometer deployments indicate that this angle decreases towards zero as the wind speed increases. Results from stations 4 and 5 differ markedly from the results from station 3, in line with expectations based on the topography illustrated in Fig. 4 but also possibly a result of the different anemometer constructions and deployments, as mentioned above and as explored by Kochendorfer et al. (2012). Consequences of the influence of gravity on buoyancy are evident in Fig. 9B, where it is seen that the pitch angles derived for stations 4 and 5 for highly unstable conditions are consistently less than those detected in other stratification regimes, with the surprising irregularity of the strongly stable results. The station 3 results indicate little stability variation of pitch with wind direction — this station was located in a less complicated surroundings.

Partitioning Variable Selection

Given the many possible partitioning variables, the task then becomes choosing the best method to select the simplest but best performing combination of them. The task of variable selection cannot be performed by the MOB procedure. The solution was to perform cross-validation over different combinations of the partitioning variables. The process includes a series of “cross-validations” in which unexplained variances are computed at the end of each *model* improvement before the *model* in question is augmented by adding into consideration the most contributing of the remaining variables. Cross validation is a statistical method aid in comparing and selecting models (see Hastie et al. (2009)). Cross validation quantifies how well a *model* with a combination of parameters corresponds to “unseen” observations. The intent is to determine the best performing model (defined by a low RMSE.) with the lowest number of terminal nodes. In our case, the available observations were randomly split into five subsets of equal size. The *model* derived at a specific node where a further step is warranted was fitted to a dataset made up of four of the five equally sized sub-sets of data and the results tested using the fifth sub-set. The procedure was repeated for each of the five sub-sets, yielding five quantifications of the unexplained variance. The partitioning variable combination with the lowest, significant RMSE is then optimal.

In the present application, the mutually exclusive partitioning variables were stability class, solar altitude, height of measurement, day of year (henceforth *DOY*) and wind direction

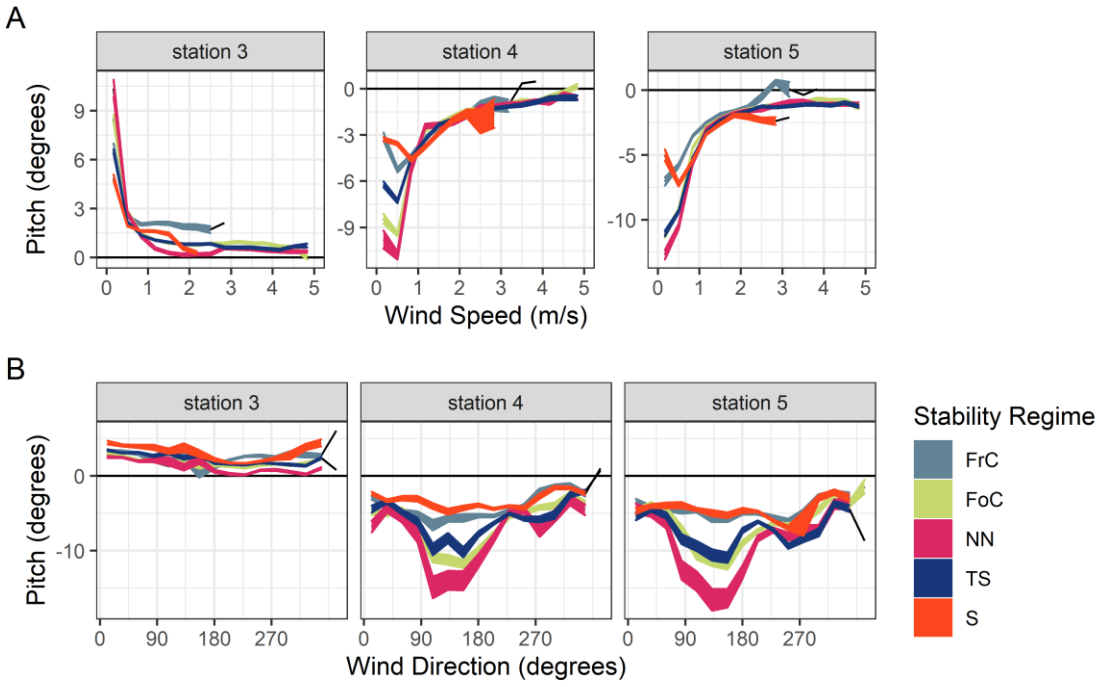

Figure 9. The shapes of the pitch angle as functions of wind speed, stability regimes and wind direction. The width of the shapes corresponds to one standard error from the mean.

Wind direction was added to permit examination of an RPF. The mutually exclusive partitioning variables were consequently never simultaneously partitioned. The comparison is not one to one as the stability and height regimes are categorical as defined here while altitude, *DOY* and wind direction are continuous. For each of the three eddy covariance measurement locations, five–fold cross–validation tests were conducted for each combination of variables indicated by the MOB process as each node was encountered. While the combination significance varied across stations, the overall trend remained the same. The lowest significant RMSE occurred when all four variables were included and the worst performing variable combination was the stability class as the sole main effect.

Choosing the most parsimonious *model* presents additional difficulties. The RMSE varies inversely with the number of terminal nodes as the number of contributing variables increases and sample sizes are reduced. This is neither profound nor surprising. Figure 10 presents a summary of the intermediate and final results obtained through the process of decision-tree development now considered. Inspection of Fig. 10 reveals that including the change of heights of the instrument causes a systematic improvement of the model. Except for station 3, the *models* including change of heights provided no significant improvements in the overall *model* fit. The terminal nodes number in range from five to 206. However, while the model complexity does not decrease, the number of decisions can be reduced whenever the wind direction (denoted as WindSector) is included. This reduction is possible because the RPF can be interpreted as the SPF.

The best improvement occurs when all variables are included but the number of terminal nodes is then large — in the range 185 to 203. Note the only categorical variables are height regime and stability. This explains why the five stability classes by themselves can resolve into a model with five terminal nodes. The continuous partitioning variables can have a large range of terminal nodes, depending where the splits occurred. Adding *DOY* yields the greatest improvement — to be seen in a comparison of results comparing *DOY* to height regime. However, there is a large sacrifice for parsimony as the number of terminal nodes increases, by up to ten–fold. In comparing partitioning variable combinations with a total of two combinations, *DOY* and wind direction have the greatest improvement and even a slight reduction in the number of terminal nodes. The improvement is greatest for station 3 and insignificantly improved in station 4 and station 5 to the other two– partitioning variable *models*. *DOY* and solar altitude have more of an advantage for station 4 and 5 at the cost of increased terminal nodes. In comparing three–variable partitioning to four–partitioning variable there is no improvement and no single performing partitioning scheme. *DOY* and wind direction appear to be the most consistent partitioning variables while solar altitude and wind speed are more inconsistent. Including a WindSector variable is convincing because it does increase the number of rules, but it does not increase the overall error. Furthermore, this

choice can take advantage of the MOB algorithm and one does not have to worry about sparse data due to short height regimes durations and predominate wind directions. This is a convincing proof of concept if a researcher wants to keep the coordinate rotation within the planar fit framing.

Results of the Recursively Partitioned Planar Fit Analysis

Figure 11 illustrates the partitioning involved during the growing season of 2018. In the upper diagram, the colored line segments correspond to different terminal *models* as appropriate for the different prevailing circumstances. It can be seen that wind sector depiction changes as the season progresses, with sector dimensions changing from the spring (before crop emergence) until the crop was mature. Some sectors were characterized by longer temporal stability that was evident as the crop grew (and as the length of sectors increased). In the lower diagram, crop height is plotted in green, anemometer height (for station 4) in black. It can be seen that wind sector depiction changes as the season progresses, with sector dimensions changing from the spring (before crop emergence) until the crop was mature.

Figure 12 shows the partitioning by solar altitude (the angle of the direct solar beam from the horizontal). The patterns, between stations had less consensus and thus the causative/physical under consideration are obfuscated. Segmentation derived using the Station 3 data appears the most consistent. From April to June there was no contribution of solar altitude to the segmentation, it should be noted that for Stations 4 and 5 there were some wind sectors that were not sensitive to solar altitude. Station 4 had a 30-degree demarcation from February to June 2018. Station 5 was less sensitive to solar altitude having only four splits and (marking where there are statistically significant variations in the way solar altitude contributes to the model) the statistics indicate starting in May 2018. The May to mid-June split over 10 degrees and from mid-June to August there was a split around -10 degrees. September and October had two splits: 0 degrees and 40 degrees. It is tempting to relate these estimates to the penetration of the slanting solar beam into the crop canopy, varying as the crop grows. Further study and additional data would be required to explore this further.

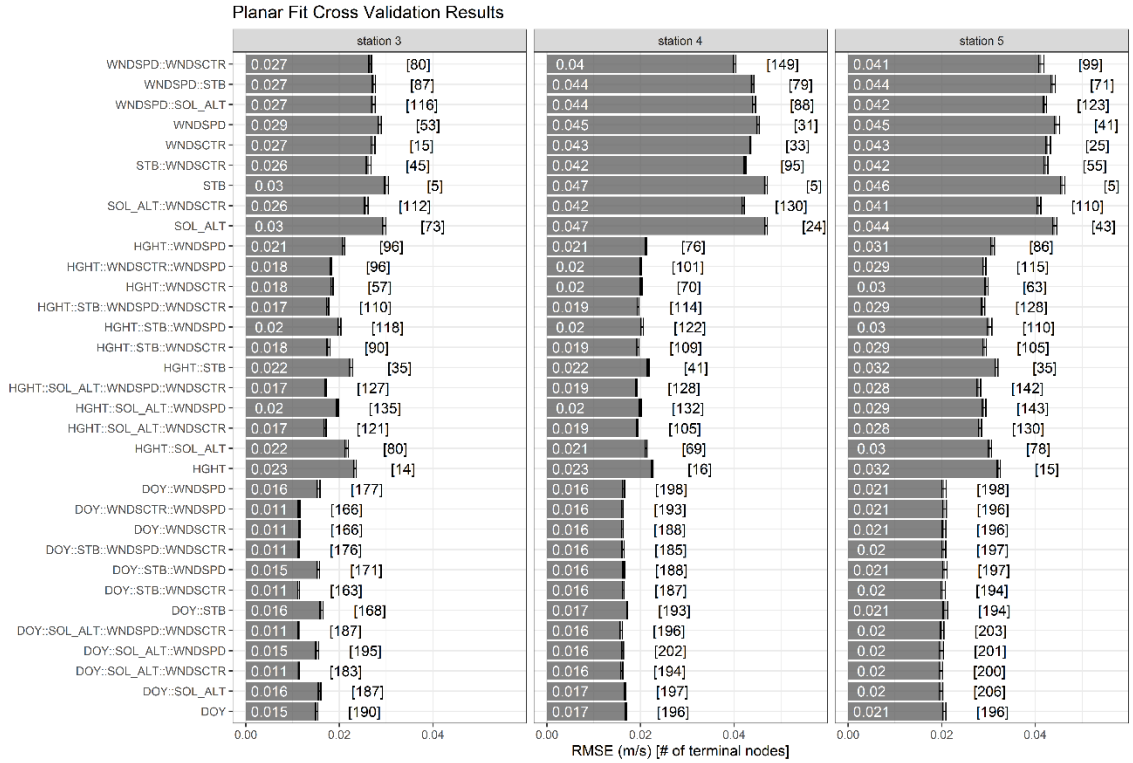

Figure 10. The average root mean square for the five–fold cross–validation for the RPF procedure. The width the error bars correspond to the 95% confidence interval. The values in square brackets correspond to the maximum number of terminal nodes.

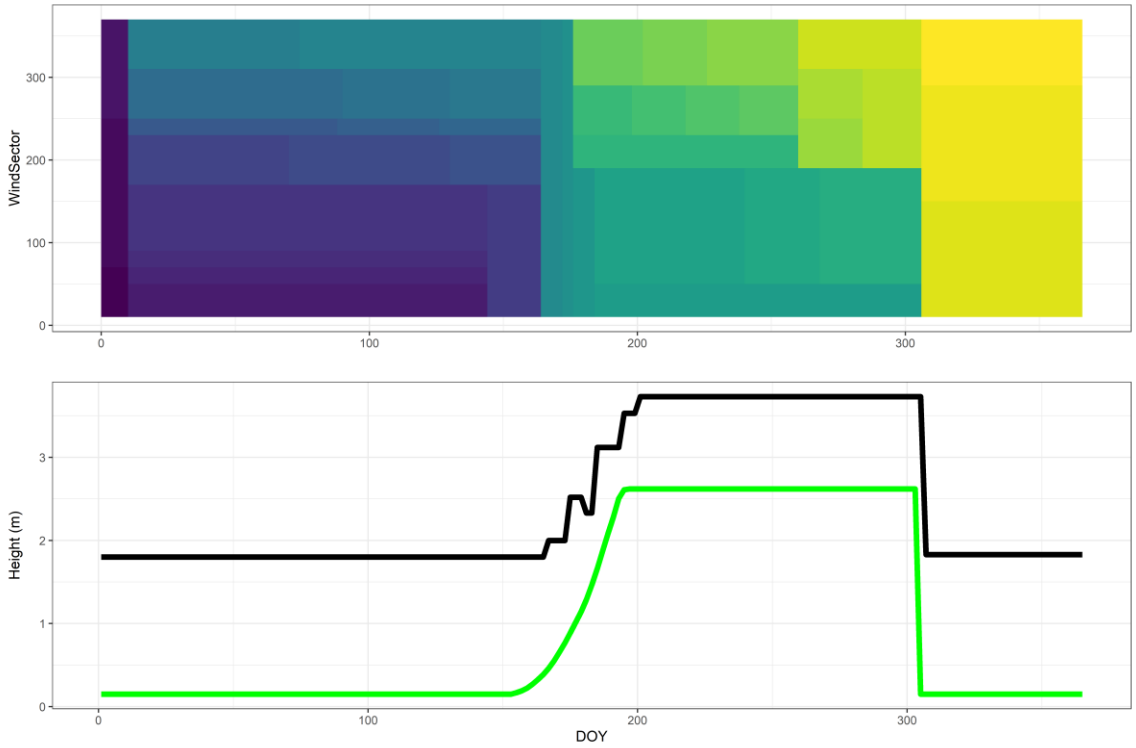

Figure 11. Segmenting results for station 4 observations of 2018. The colors in the upper diagram correspond to different segments as identified by the MOB procedure used here. In the lower diagram, the height of the growing crop is shown in green.

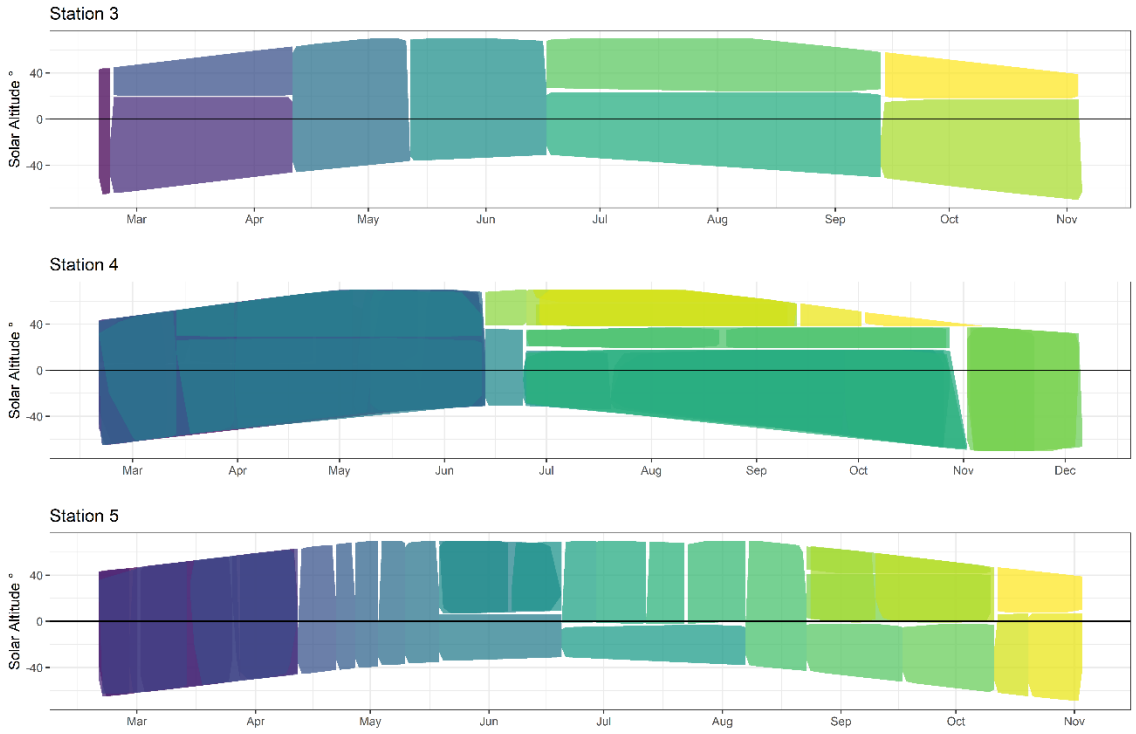

Figure 12. Illustrating the segmentation results derived using the 2018 set of observations. The y axis is the solar altitude.

Micrometeorological Inferences

Having derived optimal sensor orientation adjustments using the decision tree methodology now described, it remains to examine the consequences. To this end, consider comparisons of the results obtained using three alternative procedures — 1. No rotation (i.e., accept raw observations derived with anemometry oriented according to gravity), 2. After a double-rotation correction as is common in the micrometeorological literature and 3. Following application of the present MOB analysis. These alternatives are identified as NR, DR and RPF, respectively. Table 1 summarizes results derived using the entire dataset. Four sets of observations are represented by the results listed in Table 1: the fluxes (or covariances) corresponding to momentum, heat, water vapor and CO_2 exchange.

Examination of the results of Table 2 reveals that Site 3 provides the most consistent results. For the determination of $\overline{w'u'}$, the NR alternative is certainly unacceptable. For $\overline{w'T'}$ the results suggest that the no rotation alternative is as good as either of the alternatives. This could be interpreted as support for the expectation that gravity is the controlling factor in orientation of the vertical when $\overline{w'T'}$ is computed. In the case of the water vapour flux, it appears that the NR case is once again acceptable. Gravity is also then a controlling factor and evaporation goes along with sensible heat exchange. The situation for CO_2 is more complex, since the direction of the flux changes with time of day, from negative in the daytime when CO_2 is being taken up by the foliage to positive at night when CO_2 emission from the soil is a controlling factor. The present tabulations do not permit an easy conclusion to be drawn. It is clear, however, that the different sensor systems now used yield different results. To demonstrate this, Fig. 13 shows average diurnal cycles of CO_2 covariances as derived for the three separate sensing systems and for analyses assuming the different coordinate rotation methods already mentioned.

The average diurnal cycles of fluxes (as shown in Fig. 13) indicate strong agreements across all coordinate rotation methods for water vapor (also see Table 1). This agreement is as expected, because the exchange of water vapor is buoyancy dominated and therefore aligns with gravity, like for the sensible heat flux. At night, the departure of the DR results for *CO₂* exchange from the others (clearly evident in Fig. 13) is presently interpreted as evidence of local gravity flows responding to the terrain and entrapment in them of *CO₂* emanating from the soil. The water vapor flux results do not show this nighttime departure.

Table 2. Results of regressions for the coordinate rotation methods.

Water Vapor Flux (mmol m^{-2} s^{-1})

	Station 3		Station 4		Station 5	
	R	Slope	R	Slope	R	Slope
DR::PF	0.998	1.023±0	0.995	0.936±0.001	0.99	0.927±0.001
DR:NR	0.997	0.996±0.001	0.995	0.941±0.001	0.989	0.915±0.001
PF::NR	0.998	0.973±0	0.999	1.004±0	0.998	0.986±0.001

Carbon Dioxide Flux (µmol m^{-2} s^{-1})

	Station 3		Station 4		Station 5	
	R	Slope	R	Slope	R	Slope
DR::PF	0.946	1±0.002	0.741	0.864±0.003	0.633	0.818±0.003
DR:NR	0.955	0.986±0.002	0.739	0.86±0.003	0.622	0.798±0.003
PF::NR	0.981	0.985±0.001	0.988	0.991±0.001	0.982	0.976±0.001

$\overline{w'T'}$ (K m s^{-1})

	Station 3		Station 4		Station 5	
	R	Slope	R	Slope	R	Slope
DR::PF	0.999	1.024±0	0.995	0.949±0.001	0.997	0.948±0
DR:NR	0.999	1.017±0	0.995	0.951±0.001	0.996	0.943±0
PF::NR	0.999	0.993±0	0.999	1.001±0	0.999	0.994±0

$\overline{w'u'}$ (m^2 s^{-2})

	Station 3		Station 4		Station 5	
	R	Slope	R	Slope	R	Slope
DR::PF	0.987	1.024±0.001	0.843	1.056±0.004	0.835	1.075±0.004
DR:NR	0.285	0.321±0.006	0.428	0.38±0.005	0.504	0.416±0.004
PF::NR	0.287	0.311±0.006	0.468	0.332±0.004	0.427	0.274±0.003

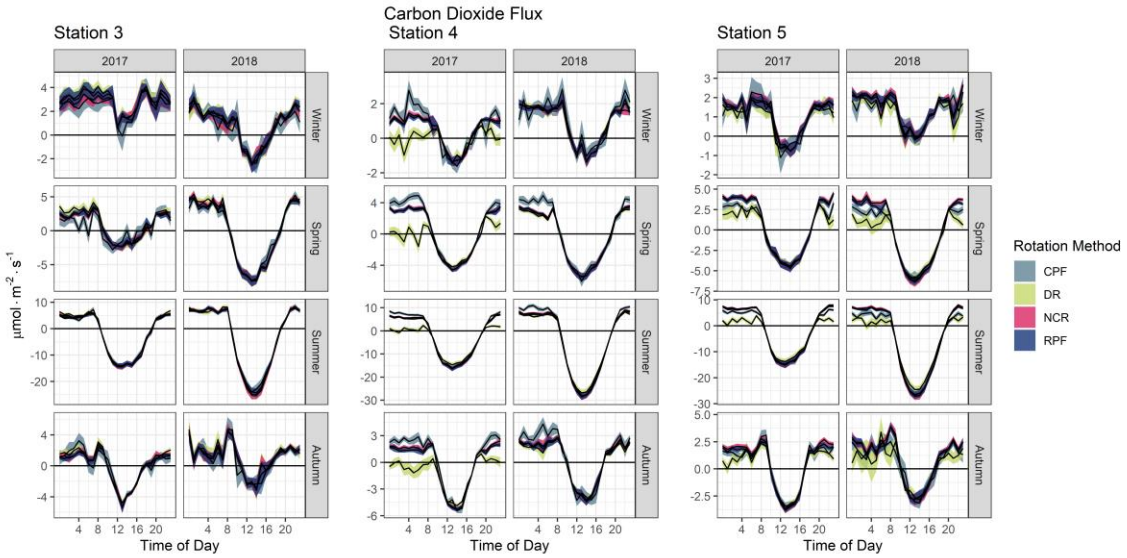

Figure 13. Diurnal trends of carbon dioxide fluxes (µmol m-2 s-1). The green curves relate to no coordinate adjustment (NR), yellow to the RPF described above and mauve to the familiar DR approach.

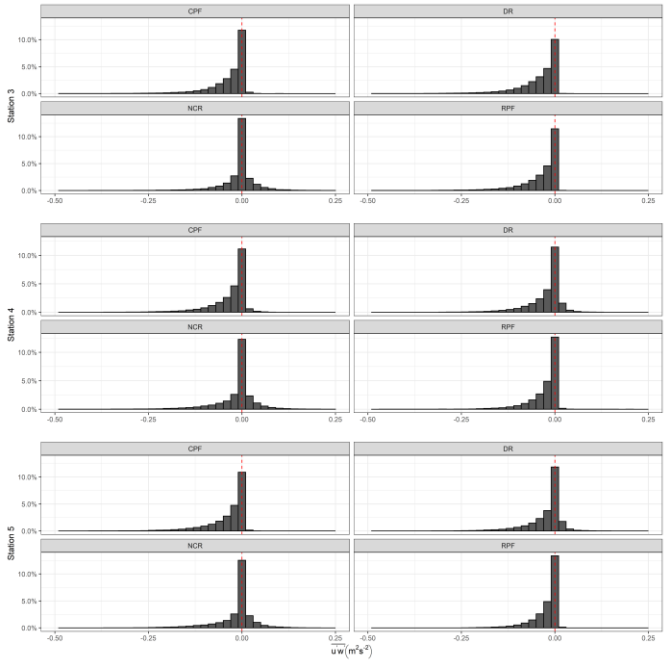

Figure 14. Frequency distributions of the momentum flux ¯(u^' w^') for different coordinate rotations.

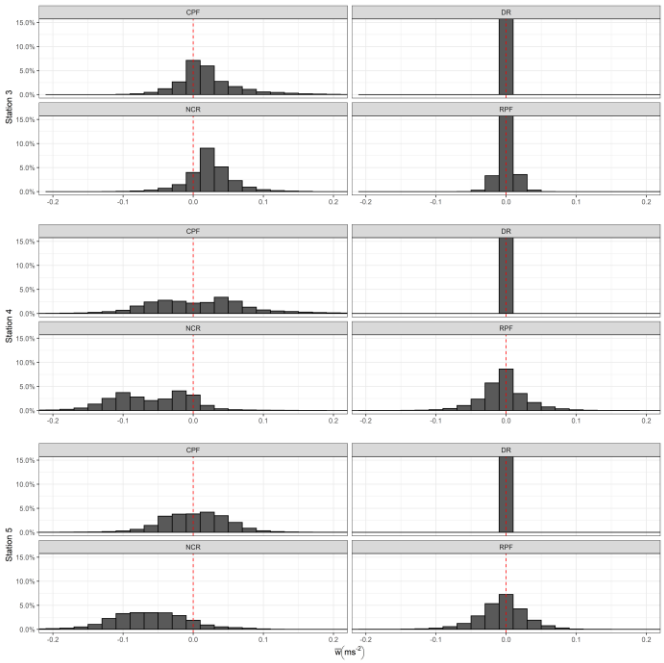

Figure 15. Frequency distributions of half-hourly w for different coordinate rotations. The DR depiction corresponds to the inherent constraint that w = 0 for all time intervals.

A simpler method to assess the effectiveness of the coordinate rotations is to examine the number of times $\overline{u'w'}$ appears to exceed zero. While positive values can arise if the flow is not steady, the values most likely appear if the coordinate system is not aligned appropriately. A positive value implies that momentum is being produced rather than consumed at the surface which is clearly inaccurate. Figure 14 shows that the frequency of detection of positive values is reduced by the RPF method now exercised, for all three installations. The DR method appears to work well for the Station 3 dataset, more so than for the other two sites. Station 4 and 5 share a similar behavior — they shared the same sonic anemometer design. Results were obtained from a fourth rotation scheme using constant planar fit (CPF) are included in the deliberations to follow. If the formalisms derived from segmented planar analysis, described above, do not differ significantly from the CPF the benefits do not warrant the additional complexity of the RPF.

The distributions of vertical velocities illustrated in Fig. 15 are especially revealing. The no-rotation datasets reveal that the anemometer at station 3 experienced a small positive bias, as must be expected from the deployment configuration. The R.M. Young instrument was on top of a vertical pole, such that the obstruction to streamlines presented by its presence would result in a local updraft regardless of wind direction or any other consideration. The Station 4 and 5 sensors were mounted at the end of horizontal arms directed into the dominant wind direction. These yielded vertical velocity determinations that appear anomalous — with consistent downdrafts. It cannot be determined whether these resulted from sensor configuration (Kochendorfer, 2012) or from the surrounding slope, but in either case the RPF methodology appears to provide a satisfying response with a distribution like a normal about zero. Using a simplified planar fit routine, CPF, centers the distribution but the spread increases. The CPF represents the mean streamlines over a rapidly changing environment and change in the height of measurement. Clearly the CPF is too simple, this is by design so it can function as a null model. The RPF easily accounted for this instrumental bias. Note that in Fig. 15 the distribution for Station 4 is bimodal. Detection of this caused the instrument to be recalibrated. However, the best overall performance appears to have been using the Station 3 data after applying the sector planar methodology as described here.

The different coordinate rotation methods yield covariance quantifications that differ in detail but do not necessarily influence the average situations that are likely to be of relevance in studies of crops. This is illustrated in Figs. 16 through 19, where results obtained over a two-week period have been combined into average time trends, for daytime and nighttime situations. Central daytime and nighttime periods are considered, defined as 1000 to 1600 LT and 2200 to 0400 LT respectively (local time = UTC – 4 h). Measurements made at Station 3 are used. The intent is to show differences that would arise if instrumentation was erected according to gravity.

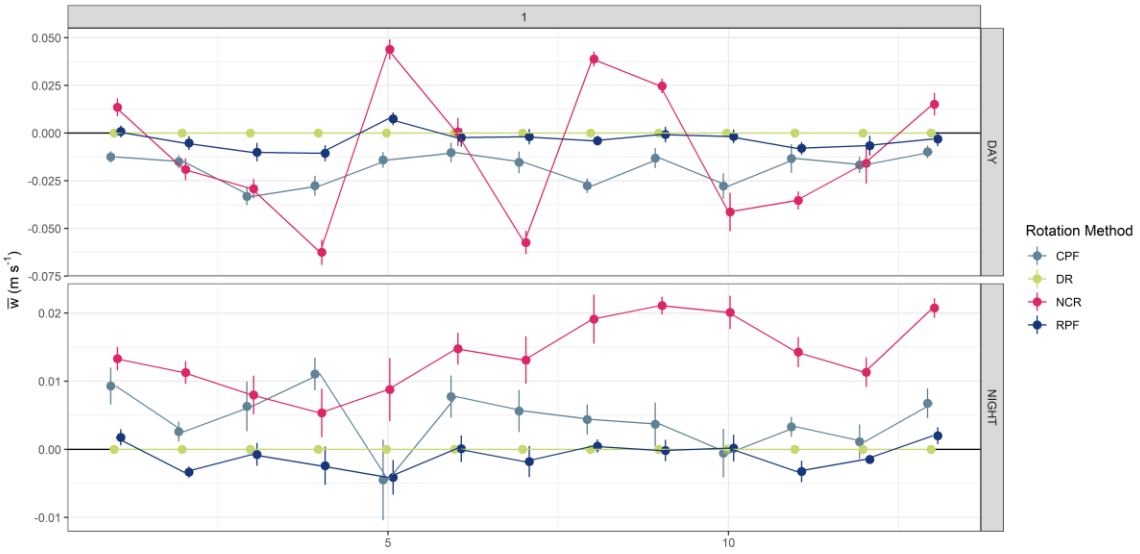

Figure 16. Daily averages of vertical velocity partitioned into day (1000 to 1600 LT) and night 2200 to 0400 LT for 1-14 of August 2017. Error bars correspond to one standard error departures from the mean.

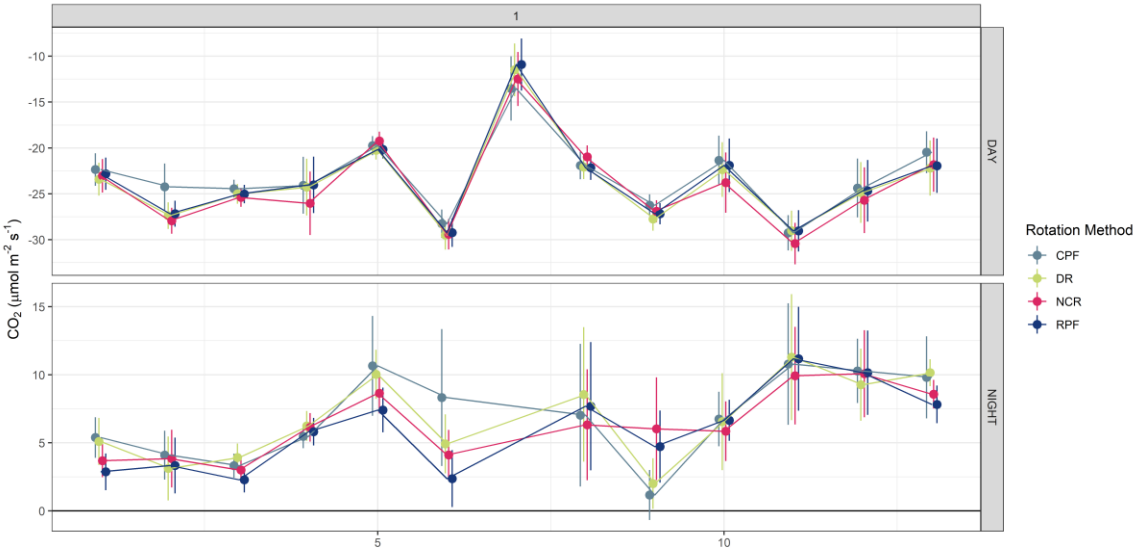

Figure 17. Daily averages of Carbon dioxide fluxes partitioned into day (1000 to 1600 LT) and night 2200 to 0400 LT for 1-14 of August 2017. Error bars correspond to one standard error departures from the mean.

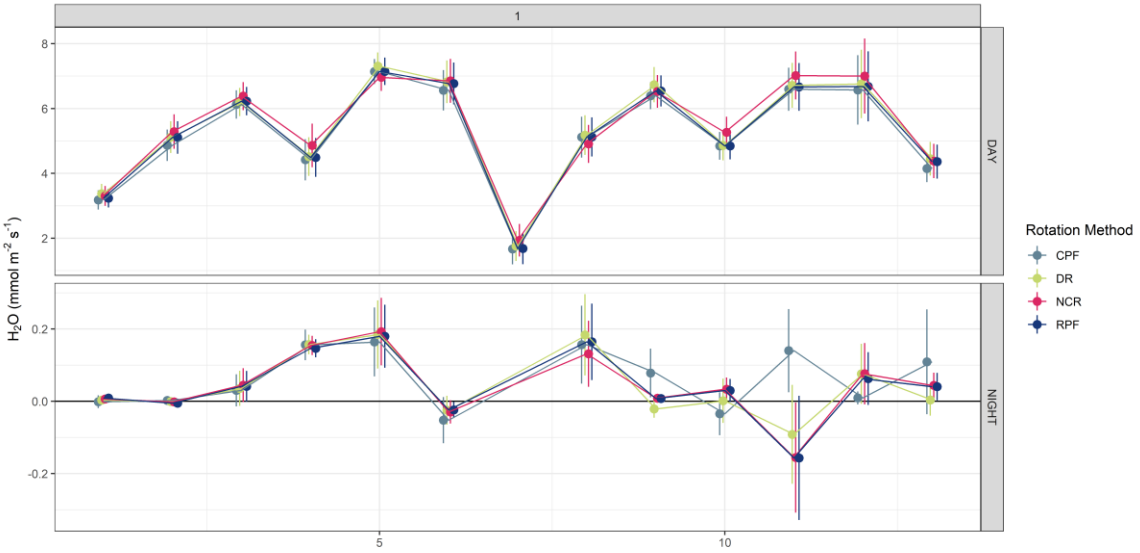

Figure 18. Daily averages of water vapor fluxes partitioned into day (1000 to 1600 LT) and night 2200 to 0400 LT for 1-14 of August 2017. Error bars correspond to one standard error departures from the mean.

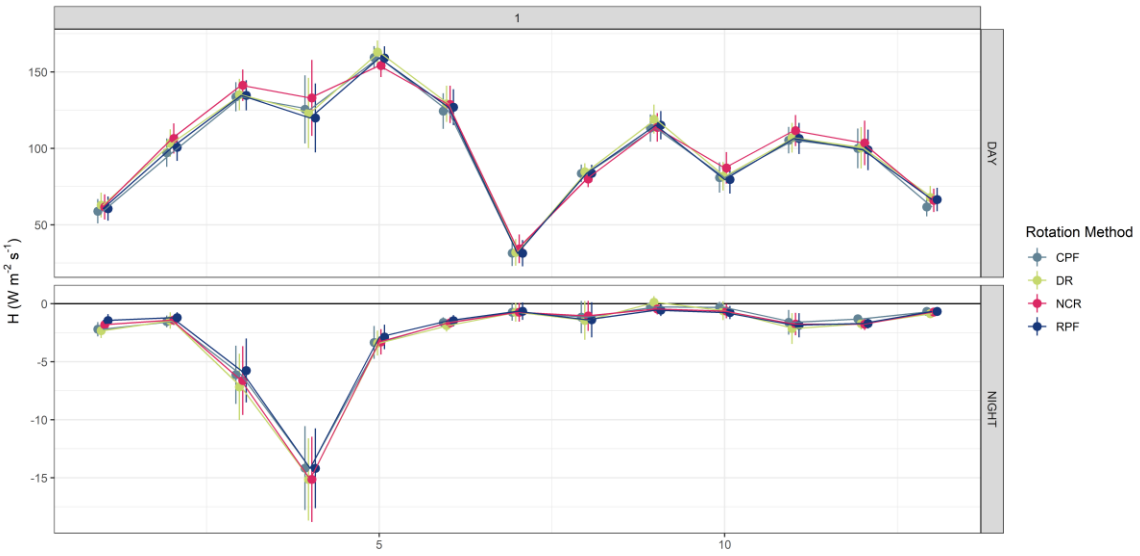

Figure 19. Daily averages of sensible heat fluxes partitioned into day (1000 to 1600 LT) and night 2200 to 0400 LT for 1-14 of August 2017. Error bars correspond to one standard error departures from the mean.

Figure 19 shows the uncorrected data reveal a highly variable downdraft in daytime and a more consistent updraft (1 to 2 cm s^{-1}) at night. The standard error bars indicate that the average recalculated vertical velocity estimates are well determined, with the familiar double-rotation method yielding zero values at all times (as required). It is not clear as to how much of the nighttime updraft can be attributed to sensor-induced streamline departure or to local topography, but regardless of this uncertainty the RPF as discussed here appears to correct for almost all of the $\overline{w}$ departure accounting well for changes in the slope with wind direction. In comparison, the CPF appears deficient. While this interpretation appears to conform to expectations, it remains to be seen if the differences affect eddy covariance determinations.

The alignment of convective exchange with gravity leads to the expectation that the alternative coordinate adjustment systems now considered should agree well, among themselves, for the case of sensible heat exchange. Each method is then adjusting towards an alignment that will differ slightly from actual vertical, with the error margin amounting to little more than the sine of the angle of tilt adjustment. In the momentum covariance case, the optimal alignment differs. The sensible heat case is shown in Fig19.

The sensible heat flux results indicate that during the night, there is good agreement among all rotation methods, while during the day DR appears to overestimate the covariance and the no-rotation method yields results consistently slightly above those from the other choices. While most of the overestimation is not significant this is an interesting trend and should be noted with caution. During night, the differences between DR and RPF are significant. Because the flux of water vapor also aligns with gravity but is less well determined (sensing of humidity with rapid response remains a challenge, relative to the measurement of temperature), it is anticipated that the agreement among the rotation options will be much as is seen in Fig. 19 for the daytime case. At night, the situation is complicated by the continuing but slow release of water vapor from the soil as well as by non-stomatal water vapor loss from the plants.

The standard error bars in Fig. 19 are substantially greater than those of Fig. 16 and differences among the rotation alternatives are such that simple methods could be adequate. However, the constant planar option appears an outlier. During the day there are no significant differences, while at night the CPF often departs from the alternatives.

The case of CO_2 (see Fig. 17) exchange follows in this sequence. The DR method appears to overestimate carbon dioxide fluxes in comparison to the RPF. The CPF and the DR methods yield the largest scatter and the largest standard errors. The nighttime situation is complicated, as expected because of the contribution of gravity flows at the surface and the pooling within them of CO_2 emitted from the soil. The DR method appears to overestimate the amount of carbon dioxide fluxes in comparison to the RPF method. The constant planar and DR methods result in the largest scatter and the largest standard errors.

Considering all of the covariance cases now examined, it seems that during the CPF disagrees the most. The 1st order coordinate rotation or no rotation appears to underestimate the fluxes for a majority of the time, however the underestimation is rarely significant. The RPF closely follows the DR. During night, the story differs, the differences between DR and RPF are significant. The DR appears to overestimate the amount of carbon dioxide fluxes in comparison to the RPF. The constant planar and the 1st order rotation have the largest scatter and the largest standard errors. There is more agreement with all rotation methods when looking at the water vapor fluxes see 18. During the day there are no significant differences, while at night the CPF estimates depart most from the others.

DISCUSSION

The discussion so far has focused on one of the three sets of data collected, from Station 3 such that the differences that occur when a different sensor system is employed and to demonstrate the time-of-day limitations of assuming gravitational control of scalar fluxes, Fig. 14 shows results from Stations 3 and 4, for sensible heat exchange (a) and for CO2 fluxes (b). Results plotted are correlation coefficients derived by regressing DR results against no rotation and segmented planar rotation against the same no rotation data, as well as the CPF acting as a null model. It is seen that neither of the rotated coordinate results yields differences greatly different from the un-rotated for daytime (actually for the period of unstable stratification), but that strong differences arise for nighttime (stable) conditions. Bearing in mind that the CO2 fluxes at night are influenced by gravitational flows and the build-up of CO2 in them from respiration processes.

For example, in highly unstable portions of the day when the streamlines become more independent of topography, there are high correlations to the rotated fluxes. This can be seen with Fig. 20 where the highest correlations occur in unstable hours 0900 to 1800 LT (local time = UTC – 4 h). Regardless of the coordinate system, lower correlations with unrotated fluxes occur outside of the unstable times of day. This is not necessarily an indictment of the coordinate system because the unrotated system would also become more invalid as stable stratification was approached. However, it appears that the DR for the IRGASON actively contaminates the fluxes. Fig. 20 also shows how the heat flux is contaminated by the DR method. However, the correlation between the two planar fit heat flux results and the unrotated heat fluxes are almost invariant with time of day and are consequently less sensitive to the choice of coordinate rotation. Care must be taken outside of unstable conditions especially for carbon dioxide fluxes (e.g., in consideration of flux partitioning), however during the unstable conditions the choice of a coordinate system, even in complex

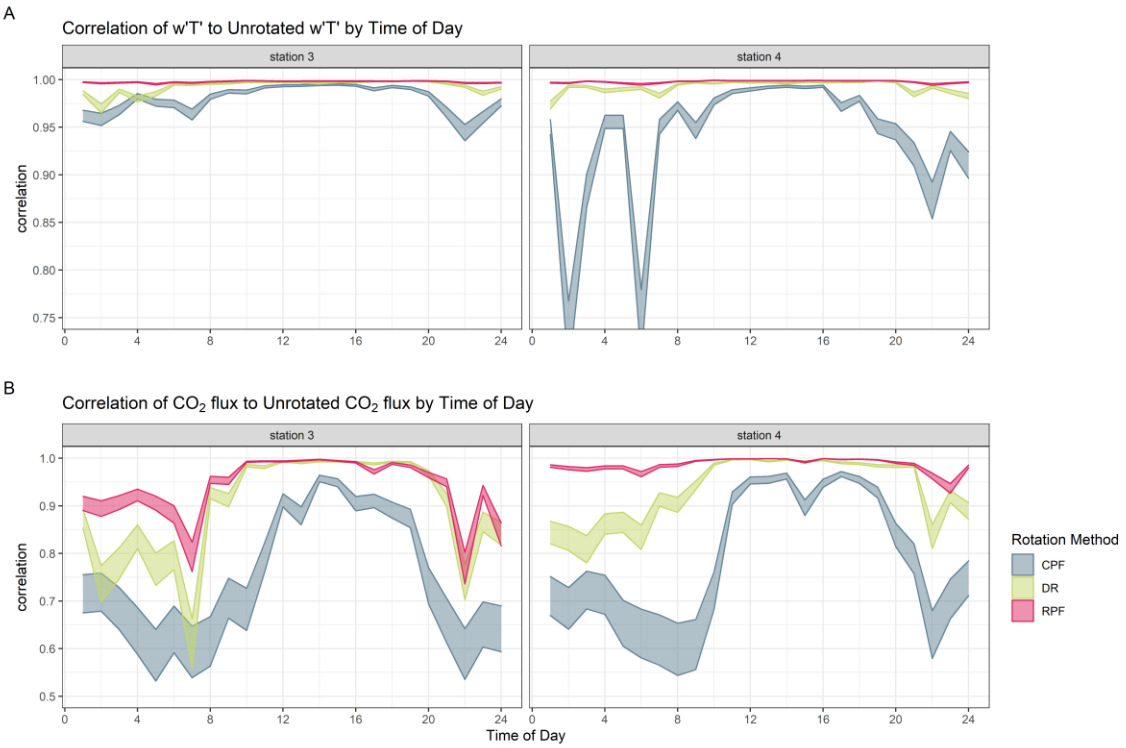

Figure 20. Correlation of coordinate rotated temperature flux and carbon dioxide flux to unrotated temperature flux by time-of-day LT (LT=UTC - 4 h). The width of the lines corresponds to ± one standard error departures from the mean.

topography, is less an issue. The CPF that was purposefully oversimplified to consider the long-term streamlines forced by the topography and represented by a single plane, has a systematically lower correlation. The reason for this is that DR and the RPF can account for unstable conditions dominated by buoyancy and so behave much more similarly during this time.

In simple concept, an optimal coordinate system should allow for vertical exchange dominating convection and streamline-normal mixing driving the momentum flux. In this context, heurism would suggest that the no-rotation option would be preferred for the sensible heat flux, provided streamline deformation by the sensor itself requires attention. In this case, use of any other coordinate system would impose a reduction in the covariance then measured. However, water vapor is less buoyant that heated air and therefore there must be a need to inject an element of evaporative mixing that recognizes transfer by the mechanical (moment-driven) turbulence. Hence, using a vertically oriented system would yield a slight underestimate of the water vapor exchange, but probably by an amount too small to identify with statistical confidence. Finally in the train of heurism, CO_2 is not buoyant and so the departure from gravity orientation of coordinates must then be greater than for the water vapor case.

Conclusions

The MOB segmental partitioning described here is a useful and objective method to identify different direction-dependent regimes for coordinate rotation; it identifies different wind sectors for planar fits by introducing a capability to integrate categorical considerations into an objective analysis of observational results. The application of the new methodology to a long-term continuous record of covariance data collected at a research site in Tennessee has revealed several issues that are of importance in the interpretation of field data as are used in micrometeorological studies but also as might be used by the agricultural community.

In particular, the analyses show that in quantifying scalar fluxes during the day, especially of sensible heat flux, evapotranspiration and carbon dioxide exchange, there is little need for coordinate rotation and less reason to choose an optimum coordinate rotation method. Alignment according to gravity is adequate. This is as expected, assuming that the controlling cause of the flux-carrying turbulence is buoyancy and hence that the sensible heat exchange is the dominant consideration. The expected alignment of the daytime fluxes with the gravitational vertical is supported and hence unrotated scalar covariances appear adequate.

The exchange of momentum is different. The RPF method then identifies a need for a different rotation — gravity is no longer a controlling influence and the influence of surface slope and differences in it are central. At night, or in stable or near-stable stratification the use of a gravity alignment is likely to result in incorrect momentum fluxes. The measurement of scalar fluxes in these circumstances requires adoption of a coordinate rotation methodology like (or the

same as) that which is best for the momentum case. In concept, the transfer of scalar quantities in these circumstances is by the same turbulence that transfers momentum, without a strong contribution of buoyancy (excepting its minor mediating influence on vertical motions).

Differences among the results from alternative coordinate rotation systems maximize for the case of momentum exchange, especially in stable conditions, but any of them would be preferable to assuming vertical exchange according to gravity. The data also show that the construction and deployment of anemometers could be an issue; the different systems deployed at Stations 3 and 4 of the present experiment provide different results when the DR technique is considered. This could be a consequence of the topographic surroundings of the two locations, but it is also noted that the DR method yields adjusted covariances that differ substantially from the present segmented planar approach. The data considered here indicate that the DR of the IRGASON wind velocity actively contaminates the flux determinations. Fig. 20 shows how the heat flux evaluation is also contaminated by the DR method.

This study illustrated the practicality of the MOB algorithm for finding optimal criteria to understand the strengths and weaknesses of coordinate rotation methods. The MOB algorithm is helpful for creating individual wind sectors and accounting for variables that may impact the fits. The method allowed a determination of which variables have the greatest influence on combining or switching different parametric *models*; the variables with the largest explanatory power are *DOY*, solar altitude and wind direction.

Thus, for the measurement of scalar fluxes and even in complex landscapes, using the unrotated fluxes or more complicated rotation methods such as the planar fit would probably is preferable to DR. This finding is not universal as the most likely explanation for the poor performance of the DR methodology in the present study is the configuration of the sensors rather than other environmental factors. However, the finding is relevant to the interpretation of research results, further highlighting the need for more research comparing coordinate rotation methods.

CHAPTER 2
FLUX IMPUTATION AND PARTITIONING

Abstract

The flux variance approach to partitioning eddy covariance fluxes was successfully implemented. A deep neural network was able to quantify the aleatoric uncertainty of the fluxes. For the two maize growing seasons, the no-till strip sequestered the most carbon dioxide at -2.58 (-3.23, -1.9) [2017] and -6.54 (-7.65, -5.45) [2018] daily grams of carbon compared to the farmer practice of -0.36 (-1.11, 0.43) [2017] and -2.66 (-3.91, -1.34) [2018] for the farmer practice and 2.31 (1.54, 3.1) [2017] and -2.93 (-4.07, -1.79) [2018] daily grams of carbon per square meter for the SMB application. This is due by lower R_e values which is supported by the partitioning results. The above ground for 2018 was analyzed using an anova and tukey honest significance test to find no significant difference of the biomass.

Introduction

The EC system effectively measures net ecosystem exchange (NEE). NEE is a measure of net ecosystem production which quantifies the net accumulation of organic matter.

$$NEE = R_e + GPP$$

While NEE yields a valuable measure of ecosystem carbon exchange, it does not describe the processes responsible for the flux. Inferring two dependent variables ecosystem respiration (R_e) and gross primary production (GPP) is a challenge because there is not a unique solution. R_e is the carbon dioxide emitted from the respiring compartments of the ecosystem (this includes litter, soil and autotrophic and heterotrophic respiration). GPP is the carbon dioxide flux originating from primary production, i.e, photosynthetic assimilation. It is not possible to identify one superior method given flux observations and an unknown “true” flux. Nevertheless, choosing an appropriate method given the constraints and larger goals of the experiment will be preferred. What follows will be a brief explanation of some of the popular methods used to partition NEE.

Overview of Partitioning Methods

To better understand and model the agro-ecosystem, the sources of the measured fluxes need to be partitioned. The water vapor fluxes are partitioned into evaporation and transpiration while carbon dioxide is partitioned into photosynthesis and ecosystem respiration. Nighttime and daytime models are often used to accomplish this partitioning procedure (Reichstein et al., 2005a). The nighttime data-based methods must be applied after the EC data have been appropriately filtered. The relationship with respiration and temperature functions as the simplest model. GPP is assumed to be zero during nighttime periods implying the measured NEE is composed entirely of R_e. A model is then fit and extrapolated to daytime periods. Air temperature is typically used instead of soil temperature due most likely to the larger percentage of soil respiration occurring

near the surface and soil temperature is often measured at a level too deep for optimal correlation with R_e (Reichstein et al., 2005a).

Method 1 nighttime data-based methods

A very common approach to model Re is the Q_{10} equation where temperature is the dominant driver:

$$R_e = R_{10} Q_{10}^{\frac{\theta-10}{10}}$$

R_{10} is the ecosystem base respiration at 10° C and Q_{10} is the temperature sensitivity parameter. Reichstein et al. (2005) modeled Re using Arrhenius kinetics:

$$R_{\mathrm{e}} = R_{10} \exp\left[E_0 \left(\frac{1}{283.15 - \theta_0} - \frac{1}{\theta - \theta_{\mathrm{ref}}}\right)\right]$$

Where E_0 is an activation energy parameter fitted to the data, and the θ_0 was set to 227.13 K (Reichstein et al., 2005).

Ecosystem respiration responds to more than just temperature alone. Water and nutrient levels are required for biological functioning. However, nutrient levels vary over longer timescales and thus are not typically represented as a separate variable.

Method 2 Daytime Partitioning

Daytime based partitioning generally uses higher quality data (because the EC assumptions are most often satisfied). Nighttime radiation suppresses turbulence and thus impedes mass transfer between surface and atmosphere as approximated by a vertical turbulent flux across a plane. Daytime flux partitioning parameters account for the effect of vapor pressure deficit on NEE, radiation on GPP, and effects of temperature on R_e. NEE is modeled using the rectangular hyperbolic light response curve:

$$NEE = \frac{\alpha \beta R_g}{\alpha R_g + \beta} + R_e$$

where α is the canopy light utilization efficiency and represents the initial slope of the light-response curve, β is the maximum carbon dioxide uptake rate of the canopy at light saturation, R_g is the global radiation. R_e is calculated using the nighttime-based approach. The terms can be accounted for using regression analysis. Lasslop, (2010) further modified β to better reflect vapor pressure deficient limitations of GPP.

Method 3 Flux Variance Similarity Partitioning

High-frequency flux data (5-10 Hz) contain more information about the sources of carbon dioxide than is often acknowledged. Scanlon and Sahu, (2008) proposed a method to estimate assimilation, respiration, evaporation, and transpiration using this high frequency data. They provided an analytical expression based on the leaf-level water-use efficiency for a given crop to partition both carbon and

water vapor fluxes (Palatella et al., 2014). Seasonal patterns of the partitioned flux estimates closely followed canopy development in an agricultural ecosystem. The reasoning behind the method is as follows: 1. According to the Monin-Obukhov similarity theory, scalar time series measured at the same position should exhibit perfect correlation; 2. There exists a spatial separation between the stomatally regulated sources/sinks and non-stomatal sources/sinks; 3. This separation results in different transport mechanisms from the canopy to the atmospheric surface layer.

$$\overline{w'c'} = \overline{w'c'_p} + \overline{w'c'_r}$$
$$\overline{w'q'} = \overline{w'q'_t} + \overline{w'q'_e}$$

Ideally, when only transpiration and photosynthesis occur, the correlation coefficient ρ between water vapor concentration (q'_t) and carbon dioxide concentration (c'_p) should be perfectly negatively correlated. This negative sign results because photosynthesis consumes carbon dioxide while the plant leaves act as sources of water vapor. (4) Direct evaporation and respiration degrade the correlation on the q-c time series. (5) Thus, the degradation magnitude depends upon the relative strength of the individual flux components as well as the degree of the correlation among these components. ρ_{qt,c_p} may indicate how much transpiration and direct evaporation (q'_e) contribute to the total water vapor flux and how much photosynthesis and respiration (c_r) contribute to the total carbon dioxide flux. This method is useful because the only inputs needed are high-frequency time series for vertical wind speed, q, and c and the knowledge of how water use efficiency varies as a function of vapor pressure deficit for the vegetation (Scanlon and Sahu, 2008). The stomatal exchange is controlled by the canopy-level water use efficiency (W). W relates the fluctuations in c'_p and q'_t via $c'_p = Wq'_t$. This flux-variance similarity (FVS) partitioning method has few inputs needed to partition the fluxes. The only estimated variable is the canopy-level water use efficiency. The other variables are carbon dioxide flux, water vapor flux as well the correlation coefficient between the concentrations of water and carbon dioxide.

Method 4 conditionally sampled eddy covariance

The fourth partitioning method briefly explained is the use of conditional daytime sampling, following Thomas et al., (2008). The developed model uses several techniques and theories to identify respiration events and to quantify the respiration flux. The model employed a combination of conditional sampling methods, quadrant analysis and relaxed eddy accumulation with hyperbolic dead bands to identify respiration events. This method would provide additional constraints on daytime R_e estimates using high frequency data. Air from a sub-canopy source is hypothesized to contain above average amounts of carbon dioxide and water vapor and can be identified by w' >0, c'>0 and q'>0, (detrended vertical velocity, carbon dioxide density, and water vapor density respectively). To help limit false classification of values with the normalized c'

and q' space an additional hyperbolic function $\overline{c'q'}(\sigma_c, \sigma_q)$ > H (the sigmas denote standard deviation). H was determined to be ¼. The hyperbolic exclusion determines that sampled data significantly deviate from the negative correlation between daytime c and q. If this method is deemed acceptable, it can be used as another independent measure of daytime respiration (Thomas et al., 2008; Zeeman et al., 2009).

Choice of Partitioning method

In the field experiment now considered, three separate sets of data were obtained from three independent instruments. Data obtained during the growing years of 2017 and 2018 provided key insights into the reasoning behind the choice of partitioning methods. During the maize growth. However, during the off season, this could not be satisfactorily satisfied. The reasoning behind this is that the three stations would often over-sample each other due to the predominate wind direction and deconvoluting which flux came from which treatment became the driving focus. Instead of limiting the sampled flux from the treatment area, integrating multiple stations over the area of interest became a source of strength rather than a limitation.

Clearly a functional or deterministic partitioning methods has its advantages but when applied to an area with site limitations. As it will smooth out the meaningful variability that could easily originate from different treatment effects. Furthermore, these mechanistic methods may not capture inhibition of leaf respiration due to high light exposure nor do the mechanistic method adequately capture the effect of soil moisture upon the canopy (Keenan et al., 2019; Xu et al., 2004). Thus, the flux variance approach or the conditionally sampled eddy covariance approach could complement this requirement. The conditional daytime sampling benefits from a larger interspace canopy structure (such as forests). This leaves the final partitioning method, the flux variance approach.

The Limitations of the Flux Variance Similarity Approach

The crucial weakness of the FVS method is the estimation of the leaf level water use efficiency. As it is the only extraneous variable (not directly related to the EC measurements), there are assumptions such as canopy structure and plant metabolic pathways (C3 vs C4 plants) that may not be satisfied. During the off season the canopy was dominated by C3 plants. Determining the appropriate method to estimate W remains the choice of the analyst. The major unknown with the largest uncertainty is estimating the intracellular concentration c_i of carbon dioxide in the canopy. W is defined as $W = 0.7\frac{\bar{c}_s - \bar{c}_i}{\bar{q}_s - \bar{q}_i}$. The 0.7 results from the differences in diffusion and convection between water vapor and carbon dioxide through stomates. The *q* and *c* are water vapor and carbon dioxide concentrations respectively and the *i* subscript corresponds to the intercellular location and *s* the surface location (Campbell and Norman, 2000; Scanlon and Sahu, 2008).

C4 plants (maize, sorghum) have a higher photosynthesis efficiency than C3 plants. C3 photosynthesis relies solely on the Calvin cycle for fixing carbon dioxide catalyzed by ribulose-1,5-bisphosphate carboxylase (Rubisco). The location of this fixation takes place in the chloroplast of the mesophyll. Rubisco competes with oxygen and carbon dioxide in the chloroplast and can undergo wasteful oxygenation rather than carboxylation. This process is called photorespiration. The C4 plants can overcome this limitation by physically separating the Calvin cycle from the meshophyll. In C4 plants the Calvin cycle occurs in the bundle-sheath cells. The concentration of carbon dioxide in the mesophyll can thus be greater than for C3 plants (Wang et al., 2012).
There are many empirical and analytical models to estimate W (see for example,Medlyn et al. (2011); Katul et al. (2009); Cowan et al. (1977); and Farquhar et al. (2001)). However without measurements of stomatal conductance and C_i, the robust models are moot. Furthermore, there will be spatial disconnects between the measured variables needed to estimate W and what the EC stations measure. Prioritizing more parsimonious models has its advantages. Scanlon et al., (2019), proposed a simplified approach to estimate W without the need to estimate C_i using optimal stomatal theory (Cowan et al., 1977; Katul et al., 2009). Cowan and Farquhar (1977), demonstrated that plants adjust their stomatal aperture to maximize carbon fixation while simultaneously minimizing water loss $\lambda = \frac{\partial \overline{w'c_p'}}{\partial \overline{w'q_t'}}$. Katul et al. (2009), showed that λ can be related to the EC flux-based water use efficiency, W, using water vapor deficit ($\bar{D} \approx \bar{q}_s - \bar{q}_i$) and ambient concentration of carbon dioxide:

$$\lambda = \frac{W^2 a \bar{D}}{\overline{c_s}}$$

The step then is to maximize the objection function $M_{obj} = -\overline{w'c_p'} - \lambda\overline{w'q_t'}$. While an elegant solution, the ratio of intercellular carbon dioxide to ambient carbon dioxide $\overline{C_i}/\overline{C_s} \geq 0.5$ because C4 plants can have much higher intercellular concentrations than the ambient air thus this optimization approach cannot in good faith be applied to C4 vegetation (Scanlon et al., 2019). Fortunately, at the site now considered the maize growing season is short and most of the off-season growth is C3 vegetation. Thus for the remaining analysis the optimization procedure was used to estimate W and a simple empirical model to estimate C4 W was used. To deal with senescencent maize and small maize leaf area index the choice to switch from one C3 to C4 W was chosen to be when the maize plant achieved V3 stage GCC > 0.45. W was then switched back to C3 when the GCC was below 0.45 (see Fig. 2).

For the C4 estimate of C_i and W a simple formulation assuming the ratio of $\overline{C_i}/\overline{C_s}$ decreases linearly as a function of vapor pressure deficit ($\bar{D}$). The choice for this was to maintain the error propagation relatively the same as in the C3 case by using the same input variables: ambient carbon dioxide measurements and $\bar{D}$. The function is $\bar{C}_i = \bar{C}_s \cdot (1 - 2.7^{10-4} \cdot \bar{D})$ (Morison and Gifford, 1983).

Finally $\bar{Q}_l$ is calculated using downward looking infrared to estimate temperature of the leaf to estimate saturated vapor pressure. $\bar{Q}_l$ assumes that there is 100% relative humidity in the intercellular spaces.

Analysis of Partitioned Fluxes

Introduction

As this partitioning process uses high frequency data, when the dataloggers were not recording to external cards or the stations were not operating, no partitioning could result. A summary of the data loss for 30-minute fluxes is seen below. The stomatal fluxes were set to zero when the incoming shortwave radiation (Rg) was less than 10 W/m^2. All fluxes at night were measured by the EC system can be safely assumed to be non-stomatal fluxes.

Friction Velocity filtering

It is well noted that during stable conditions eddy covariance underestimates carbon dioxide fluxes (see for example: Goulden et al. (1996) and Finnigan (2008); as well as Loescher et al. (2006); Zhang et al. (2006) and Jarvis et al. (1997)). From a biological perspective there should be no sensitivity to respiration to friction velocity (u^*) (Goulden et al., 1996). With this behavior the night flux error acts as a selective systematic error because it affects more night nonstomatal flux measurements than when the ecosystem sequesters the carbon during the day. Thus, for any long term measurements including this systematic error will lead to an overestimation of carbon sequestration.

Goulden et al., (1996) offered a simple criterion to discard data below a critical u^* threshold where NEE and u^* are dependent on each other. The data was first sorted into stomatal and non-stomotal fluxes using an Rg threshold of 10 w/m^2 to indicated nocturnal conditions. To determine u^* thresholds over a changing ecosystem, where changes in canopy structure can alter the relation of u^* to NEE, individual scenarios for different seasons were estimated following the procedure of Papale et al. (2006). Briefly the method estimates the u^* threshold in each season and temperature subclass by binning the records to similar u^* and computing the mean NEE and mean u^* for each class. Then a change point method is applied to each bin to determine the threshold. The threshold is then found if a binned NEE is less than 0.95 times the mean of the proceeding 10 binned NEE values (Papale et al., 2006; Wutzler et al., 2018).
While the threshold values did vary throughout the season and by EC station, it averaged around 0.09 m s^{-1}. The higher threshold for station 3 is most simply attributed to the different anemometer and/or mast configuration. Upon determining this specific systematic error, a gap filling method remains the next step to estimate yearly and seasonal sums of the partitioned fluxes.

Gap Filling and Uncertainty Estimation

For this analysis, a gap filling method was needed that predicted the appropriate fluxes based on continuously measured drivers and while also conserving the noise occurring from random errors. Some such methods ranged from using Kalman filtering (Gove and Hollinger, 2006) or a multiple imputation (Hui et al., 2004) can conserve the random noise. However, for this analysis a deep learning approach to quantify the uncertainty based on valid fluxes is proposed. Deep learning has been used to gap fill eddy covariance datasets while conserving the noise in the measurements is a great improvement. Conserving the noise is crucial because it accounts for the random noise from the sensors and the environmental response.

One high performing and common technique to gap-fill EC flux observations is Marginal Distribution Sampling (MDS) first proposed by Reichstein et al. (2005b). MDS considers the flux covariation with meteorological variable as well as considering the autocorrelation of the fluxes. Thus similar meteorological conditions are sampled close to the gap of the measurements. The shorter a valid window, containing complete datasets, the more variables are considered such as incoming shortwave radiation, air temperature and vapor pressure deficit. The longer the gap the fewer variables considered and if the gap is large enough only the incoming shortwave radiation is considered. This method will be considered as a comparison to the proposed imputation model. Total number of missing half hour values after u* filtering.

Variable selection

Because the simultaneous estimation of *NEE*, *ET*, F_{cp} (GPP), F_{cr} (R_e), F_{qt}, and F_{qe}, determining continuous variables to drive the fluxes can be separated into several categories. First two analytical variables drove the distinction between night and day. This was potential radiation where the values vary during the day but are variable during the year at night, the values were constant at zero. To incorporate changing values at night solar altitude was also included. The benefit of these values is they are analytical and not sensitive to power loss or other sensor malfunctions. Second and arguably more biologically important, shortwave radiation and net radiation were included. The short-wave radiation better captures the variability in the response of the plants to diffuse or direct sunlight. The net radiation better captures the evapotranspiration forcing. Finally, in a more biological sense, three temperature variables were measured. The variables were soil temperature at a depth of 3 cm, downward looking infrared to monitor canopy temperature and air temperature. Alongside temperature measurements, vapor pressure deficit and volumetric soil moisture were included to better capture plant available water.

Table 3. u* thresholds (m s-1) thresholds by season.

Season Start	Station 3	Station 4	Station 5
1/1/2017	0.11	0.07	0.07
6/15/2017	0.11	0.09	0.08
11/14/2017	0.12	0.08	0.09
5/22/2018	0.12	0.08	0.09
10/31/2018	0.12	0.09	0.07

Table 4. Total number of missing half hour values after u* filtering.

Year	Station	F_{qe}	F_{cr}	F_{qt}	F_{cp}	*NEE*	F_q
2017	3	12826 (73%)	9531 (54%)	9267 (53%)	9267 (53%)	8389 (48%)	2826 (16%)
2017	4	9364 (53%)	4354 (25%)	4738 (27%)	4738 (27%)	7186 (41%)	391 (2%)
2017	5	9574 (55%)	4672 (27%)	5373 (31%)	5373 (31%)	7273 (42%)	493 (3%)
2018	3	12056 (69%)	8382 (48%)	8069 (46%)	8069 (46%)	8657 (49%)	4139 (24%)
2018	4	11072 (63%)	7401 (42%)	7955 (45%)	7955 (45%)	8949 (51%)	4250 (24%)
2018	5	10609 (61%)	6365 (36%)	6754 (39%)	6754 (39%)	8519 (49%)	3002 (17%)

Probabilistic Deep Learning Model Design and Training

The Probabilistic Neural Networks (PNN) directly models probability distributions to estimate data's uncertainties and to infer predictive probability distributions with its output. While there are plenty of different types of uncertainty quantifications with PNNs (see Abdar et al., 2021), the scope of the PNNs will not be discussed. For this study a Gaussian mixture model was fit to each flux. While the fluxes certainly are not Gaussian, the Gaussian mixture model creates a non-Gaussian distribution composed out of the many different normal distributions. A Gaussian mixture model is a mixture of many different Gaussian distributions weighted by mixing coefficients to, scaled by variance and centered by mean. To estimate the parameters for the output, a loss function is defined to minimize the negative log-likelihood of the linearly combined Gaussians. From this means and uncertainties can be estimated to yield a value with the aleatoric uncertainty. Aleatoric uncertainty, as opposed to epistemic uncertainty, represents the known unknowns or the data's intrinsic randomness. Epistemic uncertainty refers to some form of lack of knowledge within the domain of study.

While this study did not attempt to estimate epistemic uncertainty, to better calibrate the PNN, all three stations were first trained together. Training all datasets together exposed the PNN to the widest range of environmental conditions in the hopes the generalization ability will be higher when. The input variables were normalized to fit within the range of 0-1 to prevent variables with higher magnitude values to dominate the variables with smaller magnitude values. The independent variables estimated did not have any normalization, although overt outliers were removed.

The neural network implemented was relatively simple with only three hidden layers. However, the first hidden layer had 2048 neurons, the second 1024 and the third 512 neurons (see Fig. 21 All the shared layers had a batch normalization layer followed by a leaky rectified linear unit and a dropout layer (Srivastava et al., 2014). To prevent overfitting, three drop out layers with a dropout rate of 55 percent was set for the shared layers. There were six outputs corresponding to the six fluxes. Each output had two more hidden layers with 256 neurons and a Relu activation (Glorot et al., 2011), followed by a dropout layer of 35 percent, the second layer had no activation and was responsible for estimating the mixture coefficients, the mean and the variance, because there were 7 components for the Gaussian mixture model, this layer had 21 neurons. Finally, each six output layers estimated a mixture distribution, with independent normal components. The depth and number of neurons within each layer was found via cross validation.

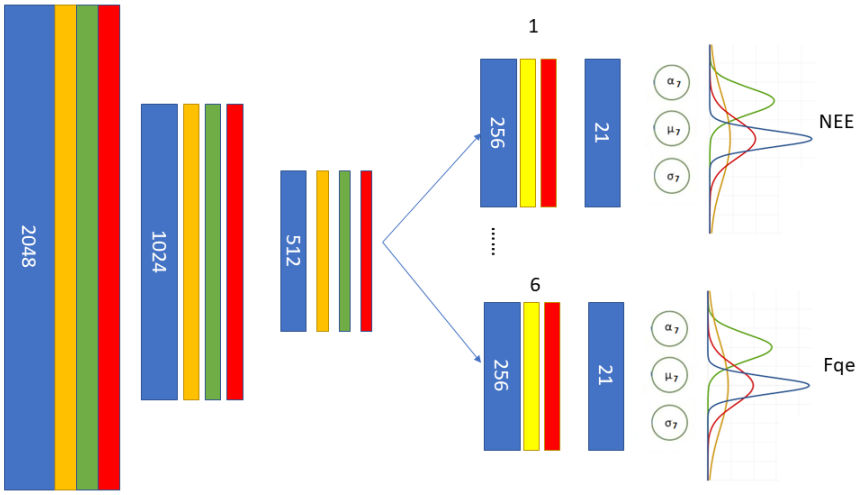

Figure 21 . This figure illustrates the PNN model, the blue is the densely-connected NN layer with the number of neurons specified, the orange corresponds to the batch normalization layer the green to leaky Relu activation, finally the red is the dropout layer.

The PNN was trained for 1500 epochs with a batch size of 64. The first training process took 52 minutes using an NVIDIA GeForce GTX 1080. While this first process will train the network on a wider range of variables and environmental conditions, it will also combine the random noise of all three stations. Thus, using the process of transfer learning, the individual stations were trained on the same network with only the first layer frozen. The remaining layers were allowed to train and achieved much higher accuracy than if the functional model was only exposed to one station's variables at a time. The programs used to train this gap filling model was Tensorflow (Abadi et al., 2015). Adam optimization with a learning rate of $5 \cdot 10^{-4}$ was used for both ensemble training and transfer learning (Kingma and Ba, 2014). Finally, the loss function used to train the different mixture of Gaussian distributions was the negative log likelihood.

In order to transfer what was learned from the PNN model and fine tune theme to each individual station/treatment the first layer was frozen. Freezing a layer simply means the weights are not affected by the backpropagation. The goal fine tune or calibrate the model to reliably preserve the random uncertainty for each separate station. Each new model was then trained for 200 epochs with a batch size of sixty-four. From this data for missing time can be using the estimated probability distribution for specific environmental drivers. Besides only exposing the network to 80% of the data, ten randomly separated weeks of data were withheld entirely. This was to act as an evaluation to ensure the models can generalize well and to perform statistical comparisons between gap-filled and original values.

Results of Probabilistic imputation

To evaluate the method both the Mean Absolute Error (MAE) and bias on all six fluxes were estimated. MDS was used as benchmark only to evaluate the NEE imputation and was implemented using an R package REddyProc 1.3.1 (Wutzler et al., 2018). Assessments of gap length and performance was not evaluated but was kept constant at one-week intervals; additionally, the number of missing values was not a factor in artificially introducing gaps. Bias was calculated by: bias $= \frac{\sum^{Meas.} - \sum^{Imp.}}{n}$ where *Meas.* stands for measured values, and *Imp.* stands for imputed values. Thus, when the bias is negative it means the imputation overestimates the values.

For all fluxes the MAE values ranged from 0.02 to 0.17 gCd^{-1} and from 0.05 to 1.8 $KgH_2Om^{-2}d^{-1}$ with water vapor fluxes (see Fig. 22). The bias involved similar trends with the imputation method overestimating all carbon-based fluxes except for F_{cr} or R_e and underestimating F_q in comparison to F_{qe} and F_{qt} see Fig. 23. The deep learning approach was competitive with MDS on both the bias and MAE metrics see Figs. 22 and 23. While there was higher bias of the *NEE(PNN)* to the *NEE(MDS)*, the accuracy of the *NEE(PNN)* was better. There was worse performance of the partitioned fluxes most likely due to underestimation (see Fig. 24).

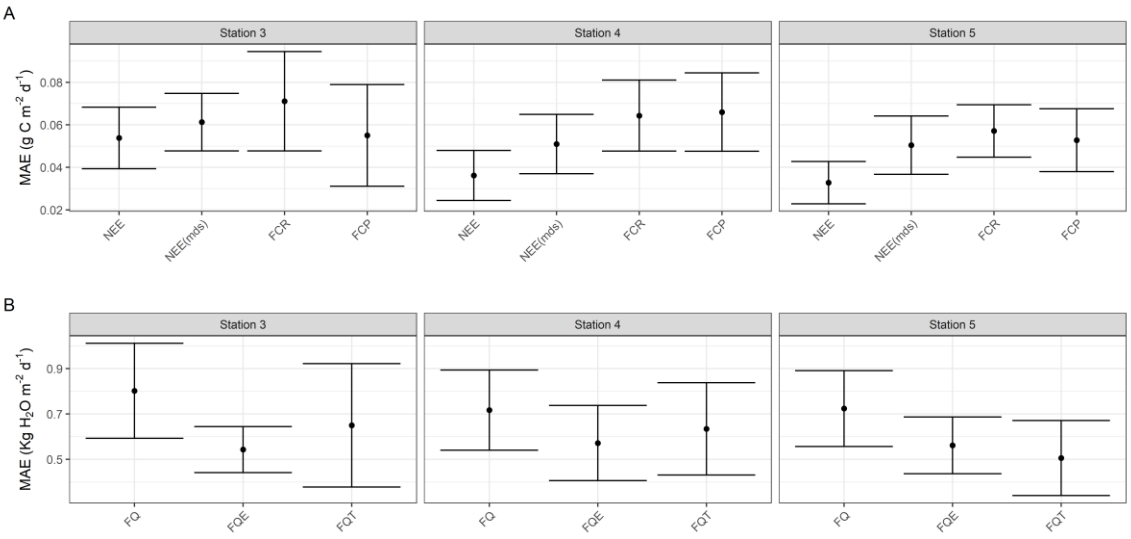

Figure 22. Mean Absolute Errors (MAE). NEE: Net Ecosystem Exchange. NEE(MDS) NEE imputed from marginal distribution sampling.

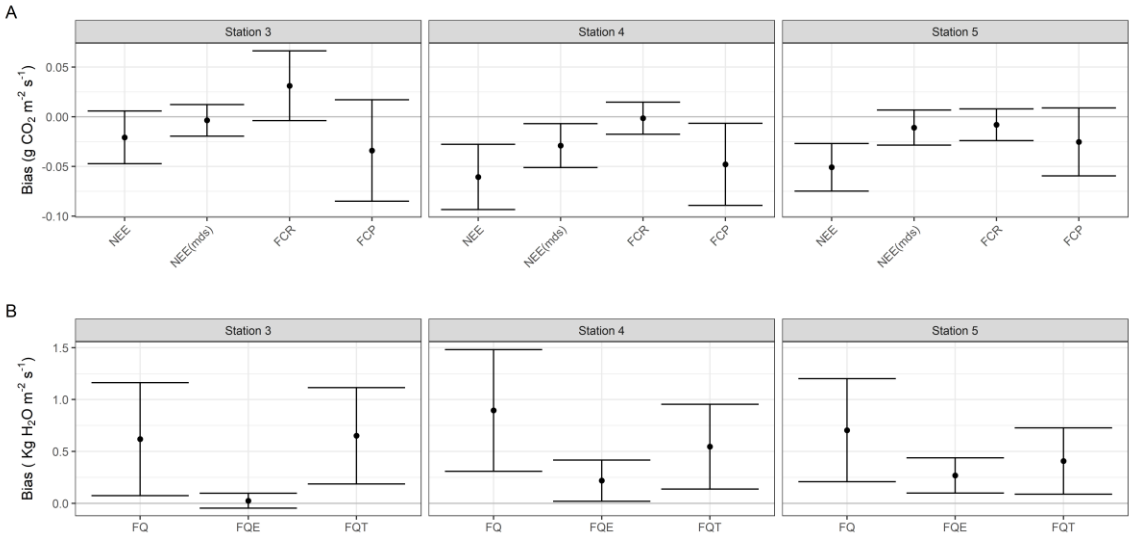

Figure 23. Bias comparing artificial gaps to imputed values.

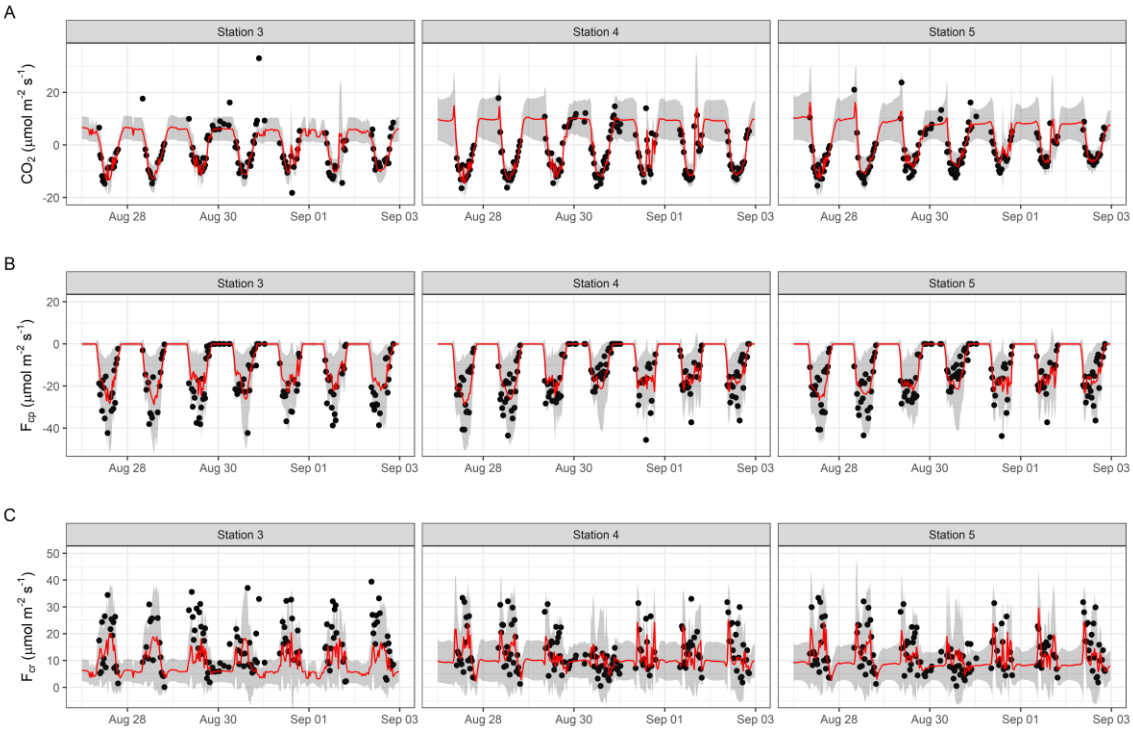

Figure 24. This figure illustrates the imputed values for carbon dioxide fluxes. The shaded area is 2 standard deviations away from the predicted mean from the DNN. Note how well the NEE is predicted but the partitioned variables seem to be underestimated.

Uncertainty and flux aggregation

To aggregate all six fluxes to daily intervals, the PNN imputed values filled any area the missing values occupied. Uncertainty was propagated by taking the standard deviation of each day. When gap lengths were less than a day ($n < 48$), the uncertainty accommodating the imputed values were propagated by inverse variance weighting. However, if the gaps were greater then one day, the uncertainty was taken into account.

Yearly and seasonal aggregates were also calculated with the uncertainties derived from the bootstrap resampling procedure (O'Dell et al., 2018; Tibshirani and Efron, 1993). The daily trends for all variables can be visualized in Figs 25 and 26. The daily trends clearly show growing events as well as herbicide application. For example, the height stress during the growing season of 2017 is clearly seen with a flatten of the F_{cp} and F_{cr}.

The trends by season indicate some interesting behaviors. The SMB and FP surfaces has significantly higher transpiration in comparison to the NT treatment during the second maize growing seasons. While the NT had higher evaporation losses during the second fallow period (see Fig. 27D). This indicates a worse water use efficiency as the GPP or F_{cp} is the same for the growing season (see Figs. 28D and 27D).

Above Ground Biomass and Yield

Over the two maize growing seasons yield was estimated for each treatment effect. During 2017, the maize was planted towards the end of June, almost two months later than is typically planted in Tennessee. This adversely effected the yield; the overall mean was low at 52 dry bushels per acre (3263 kg per hectare). Furthermore, after planting there was only 6 mm of rain over an 18-day period. Using a type II ANOVA with a Bonferroni post-hoc method, found that there is a significant difference between both tillage and fertility factors and the FP Till treatment has significantly lower yields than all the other treatments (see table 6). Of note the SMB fertility effect was significantly greater than the FP. In 2018, the average yield for the entire site was 102 dry bushel per acre (6450 kg per hectare). The ANOVA and Bonferroni post-hoc method found no significance for tillage effects but the interaction effect with soil amendment and fertilizer/soil amendment was significant. In this case the only significant difference between treatments was that the no till strip on the farmer practice side had higher yields than any other treatment (see table 7). The harvesting of the maize was complicated due to higher weed competition, which could have affected the harvest with the combine. There was much more weed competition on the tilled SMB side.

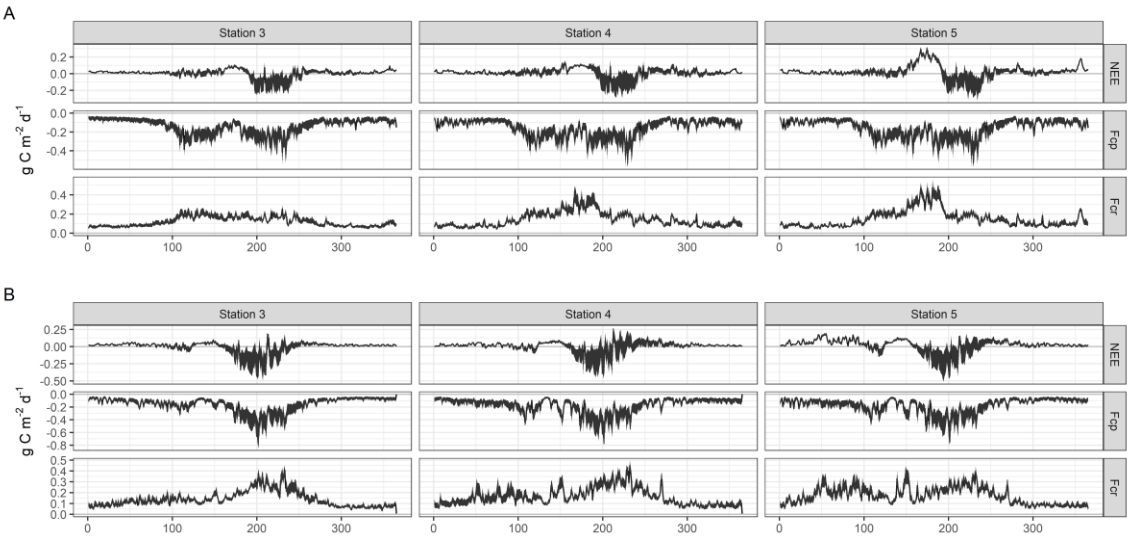

Figure 25. Daily averages for 2017 (A) and 2018 (B). The width of the lines indicates the standard error of the daily mean.

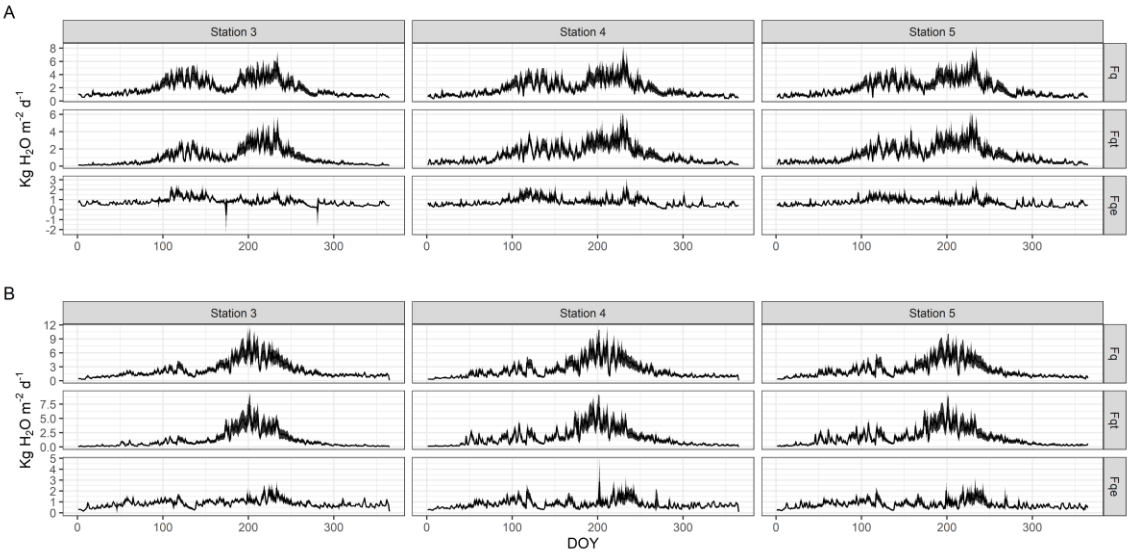

Figure 26. Daily averages for 2017 (A) and 2018 (B). The width of the lines indicates the standard error of the daily mean.

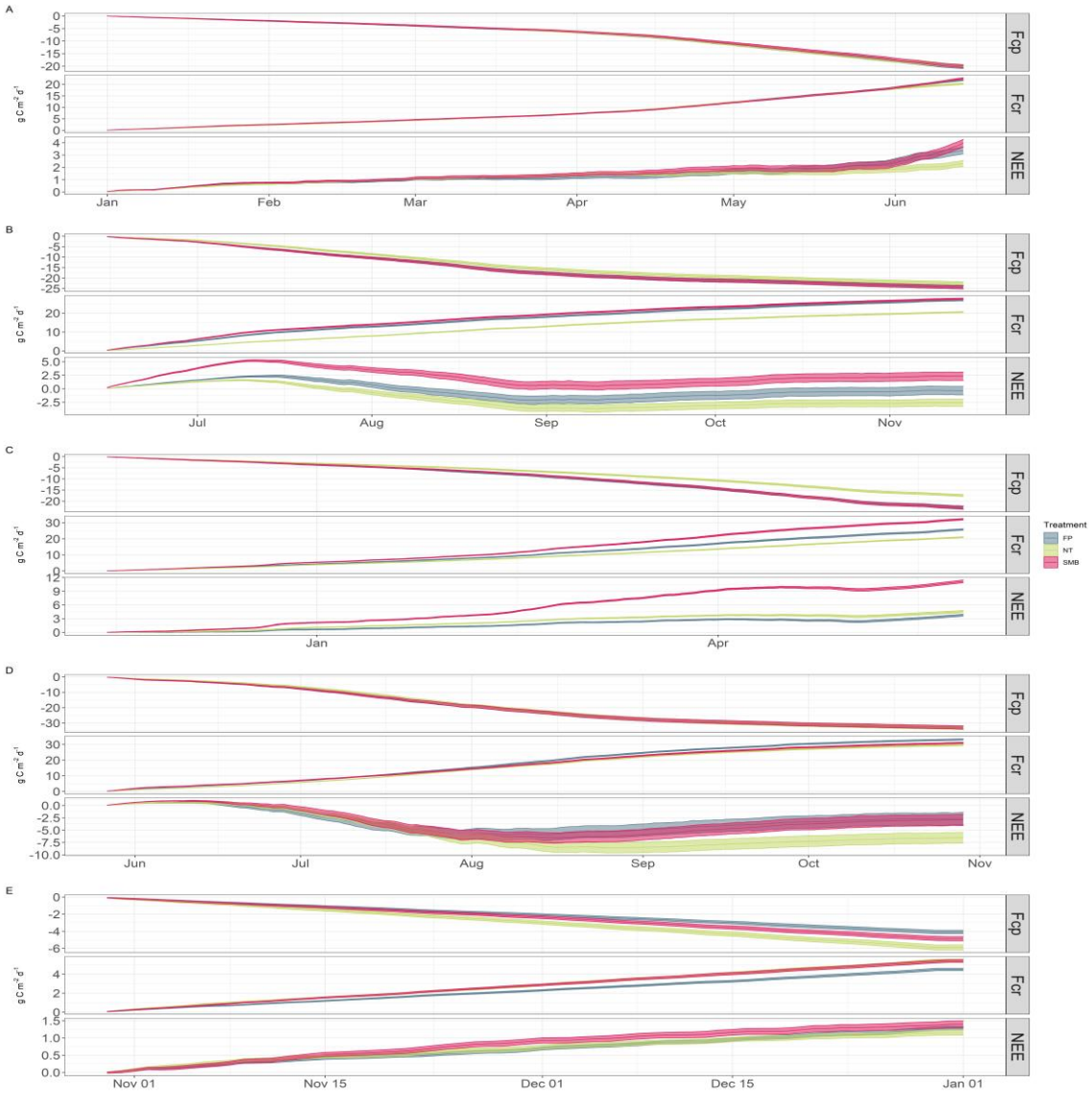

Figure 27. Cumulative sums with 95 % confidence intervals for all five seasons. A winter-spring fallow 2017, B maize growing season to harvest 2017, C Autumn to spring fallow, D 2018 maize growing season to harvest, E Autumn to Winter Fallow.

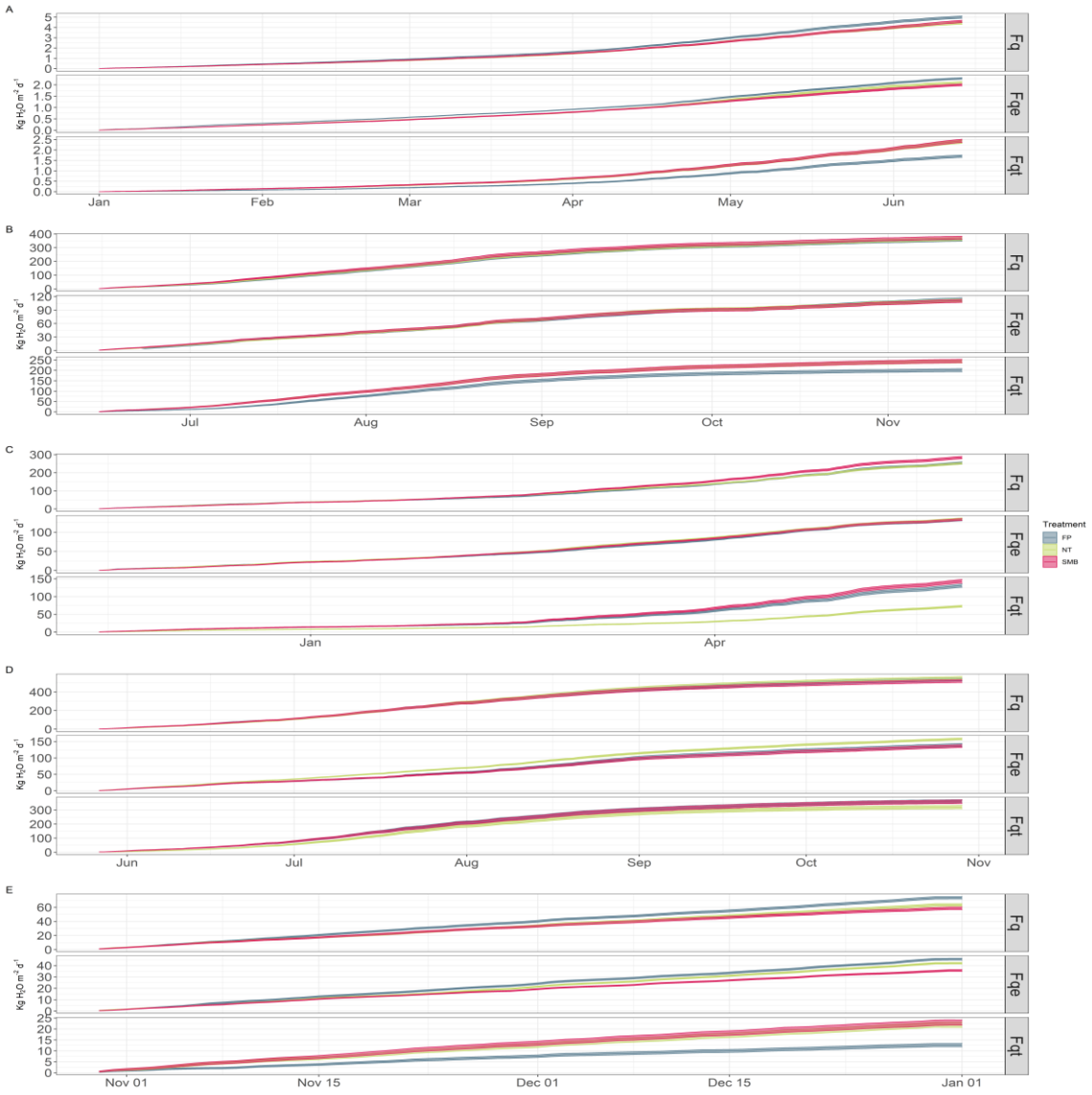

Figure 28. Cumulative sums with 95 % confidence intervals for all five seasons. A winter-spring fallow 2017, B maize growing season to harvest 2017, C Autumn to spring fallow, D 2018 maize growing season to harvest, E Autumn to Winter Fallow.

Table 5. Summary of the accumulated sums with 95 percent confidence intervals for all treatments and seasons.

		NT			FP			SMB		
Season	End Date	**Fcp** (g m^{-2} d^-1)	**NEE** (g m^{-2} d^-1)	**R_e** (g m^{-2} d^-1)	**GPP** (g m^{-2} d^-1)	**NEE** (g m^{-2} d^-1)	**R_e** (g m^{-2} d^-1)	**GPP** (g m^{-2} d^-1)	**NEE** (g m^{-2} d^-1)	**R_e** (g m^{-2} d^-1)
Fallow 1	6/14/2017	-19.82 (-20.38, -19.28)	2.32 (2.09, 2.56)	20.28 (19.97, 20.57)	-20.41 (-20.95, -19.84)	3.39 (3.1, 3.66)	21.93 (21.6, 22.23)	-20.04 (-20.63, -19.47)	3.97 (3.65, 4.28)	22.61 (22.27, 22.92)
Fallow 2	5/26/2018	-17.46 (-17.92, -17)	4.57 (4.33, 4.81)	20.98 (20.68, 21.28)	-22.76 (-23.39, -22.15)	3.77 (3.55, 4)	25.79 (25.33, 26.25)	-22.99 (-23.65, -22.35)	11.17 (10.88, 11.46)	32.16 (31.68, 32.64)
Fallow 3	1/1/2019	-4.08 (-4.28, -3.89)	1.28 (1.22, 1.34)	4.5 (4.37, 4.63)	-5.89 (-6.18, -5.6)	1.15 (1.08, 1.23)	5.42 (5.25, 5.59)	-4.86 (-5.1, -4.62)	1.4 (1.3, 1.5)	5.39 (5.24, 5.53)
Maize 1	11/14/2017	-22.44 (-23.16, -21.81)	-2.58 (-3.23, -1.9)	20.56 (20.29, 20.84)	-24.26 (-25.02, -23.52)	-0.36 (-1.11, 0.43)	26.92 (26.53, 27.3)	-24.43 (-25.19, -23.66)	2.31 (1.54, 3.1)	27.66 (27.31, 28.02)
Maize 2	10/29/2018	-33.19 (-34.27, -32.09)	-6.54 (-7.65, -5.45)	29.68 (29.31, 30.07)	-32.99 (-34.05, -31.88)	-2.66 (-3.91, -1.34)	33.28 (32.85, 33.69)	-32.84 (-33.93, -31.79)	-2.93 (-4.07, -1.79)	31.01 (30.62, 31.4)
Season	End Date	**Fq** (kg m^{-2} d^-1)	**Fqt** (kg m^{-2} d^-1)	**Fqe** (kg m^{-2} d^-1)	**Fq** (kg m^{-2} d^-1)	**Fqt** (kg m^{-2} d^-1)	**Fqe** (kg m^{-2} d^-1)	**Fq** (kg m^{-2} d^-1)	**Fqt** (kg m^{-2} d^-1)	**Fqe** (kg m^{-2} d^-1)
Fallow 1	6/14/2017	330.47 (323.2, 337.52)	112.42 (108.55, 116.24)	150.69 (148.34, 152.92)	292.43 (284.94, 299.9)	158.24 (153.17, 163.2)	137.98 (134.63, 141.25)	302.87 (295.88, 310.37)	161.17 (156.12, 166.25)	132.1 (129.3, 134.91)
Fallow 2	5/26/2018	251.53 (247.24, 256.17)	72.78 (70.28, 75.28)	135.4 (133.53, 137.29)	254.7 (248.77, 260.48)	130.7 (126.25, 135.13)	132.19 (129.99, 134.52)	283.99 (277.58, 290.55)	143.49 (138.72, 148.18)	133.16 (130.98, 135.34)
Fallow 3	1/1/2019	73.38 (71.74, 74.98)	12.66 (11.95, 13.38)	45.65 (44.86, 46.46)	63.36 (61.63, 65.1)	21.96 (20.84, 23.08)	42.08 (41.4, 42.77)	58.5 (56.82, 60.22)	23.01 (21.81, 24.14)	35.65 (34.92, 36.37)
Maize 1	11/14/2017	356.7 (347.91, 365.67)	201.13 (193.96, 208.4)	114.24 (110.87, 117.46)	363.61 (353.32 373.94)	244.34 (236.2, 252.18)	111.19 (108.04 114.37)	373.29 (362.37, 383.98)	245.46 (237.59, 253.28)	110.26 (107.1, 113.6)
Maize 2	10/29/2018	551.27 (536.66, 566.68)	320.06 (308.7, 331.38)	158 (155.39, 160.61)	534.53 (518.65, 549.8)	360.69 (348.4, 373.02)	139.99 (135.29 144.4)	517.92 (502.4, 532.77)	358.3 (346.7, 370.84)	136.12 (131.9, 140.19)

Once the maize crop achieved V6 vegetation stage in 2018, above ground biomass was obtained weekly until R4. For each treatment, four samples were randomly obtained from the treatment zones. The samples were then dried in an oven for up to ten days or when the weight stabilized at a temperature of 55 degrees C. When the maize stopped growing around VT and entered the reproductive stage an ANOVA and post-hoc test was conducted to determine whether there was a treatment effect of either tillage or soil amendment. There are some interesting trends to examine. At the halting of the sampling methods at the R4 stage, the tilled treatments appeared to have lost the most weight, while the no-tilled treatments appeared to continue gaining mass. Whether the above ground biomass was significant or not, this analysis did not account for below ground biomass nor did it measure the concentration of the carbon within the plant. Nevertheless, when paired with the partitioned fluxes, some more information on the heterotrophic soil respiration can be gleaned. The above ground biomass is an underestimation of the net ecosystem productivity (NEP). NEP is defined as $NEP = GPP - R_a$ where R_a is the autotrophic respiration. Thus, using the estimated GPP for the maize growing season and the underestimated NEP the minimum R_a can be estimated. Furthermore, once the R_a is calculated and compared to the cumulated R_e the upper bounds of the heterotrophic respiration can be estimated. This gives significant interpretive power to the behavior of the decomposition of soil organic matter.

As the ANOVA and post-hoc test did not find any significant difference at the VT stage, it can be concluded on the NEP interpretation that there are no significant differences between treatment effects. However, the aggregated fluxes do show significant differences as the tilled SMB has higher GPP values than the other two stations. Because there were no significant differences in above ground biomass between treatments, the non-linear Weibull model for growth curve data was fit to the biomass. To determine the NEP of the plants the amount of carbon in the plant was assumed to be 42 percent (Ma et al., 2018). The population of the field was measured at 24,800 ± 1970 plants per acre which yields an average 6.1 plants per square meter. From the continuous model the differences of each site GPP was calculated to estimate R_a. Heterotrophic respiration was then estimated: $R_h = R_e - R_a$. While the actual values cannot be trusted, the trends should conservatively reflect conditions in the soil. The heterotrophic respiration was lowest for the no-till strip (10.04 ±0.78 daily grams of carbon) and lower for the SMB practice (9.98 ±0.78 daily grams of carbon per square meter) the FP treatment had the highest cumulative emission of 10.91 ±0.78 daily grams of carbon. The autotrophic respiration had the inverse pattern. SMB emitted 5.55 ±0.55 daily grams of carbon. The crop on the FP treatment emitted the highest 5.58 ±0.55 daily grams of carbon while the no till emitted the lowest at 5.01 ±0.55 daily grams of carbon.

Table 6. Summary and significance testing for 2017 yield.

Fert	Tillage	Mean (kg/ha)	Standard Error of Mean	Letter Group
Fp	**NT**	3833.68	84.0377	**A**
Fp	**T**	2112.05	72.7788	**B**
SMB	**NT**	3645.78	84.0377	**A**
SMB	**T**	3779.89	72.7788	**A**

Table 7. Summary and significance testing for 2018 yield.

Fertilizer	Till age	Mean (kg/ha)	Standard Error	Letter Group
Fp	**NT**	7237.50	136.3907	**B**
Fp	**T**	6543.75	347.9687	**A**
SMB	**NT**	5763.50	198.5466	**A**
SMB	**T**	6257.50	269.2931	**A**

Table 8. Analysis of Variance Table above ground biomass.

	Df	Sum Sq	Mean Sq	F value	Pr(>F)
tillage	1	0.1838	0.1838	7.813e-05	0.9931
fertilizer	1	4223	4223	1.795	0.2033
tillage:fertilizer	1	21.52	21.52	0.009146	0.9253
Residuals	13	30587	2353	-	-

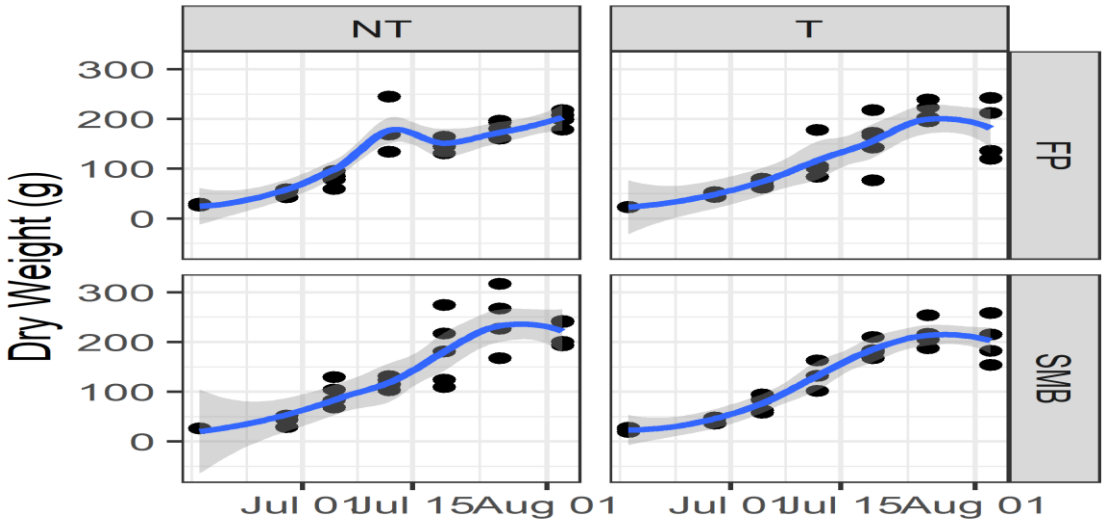

Figure 29. This figure illustrates the trend and variability of all sampled and oven dry above ground biomass for the year of 2018. NT=No Till, T= Tilled, FP= Farmer Practice, and SMB Spent Microbial Biomass.

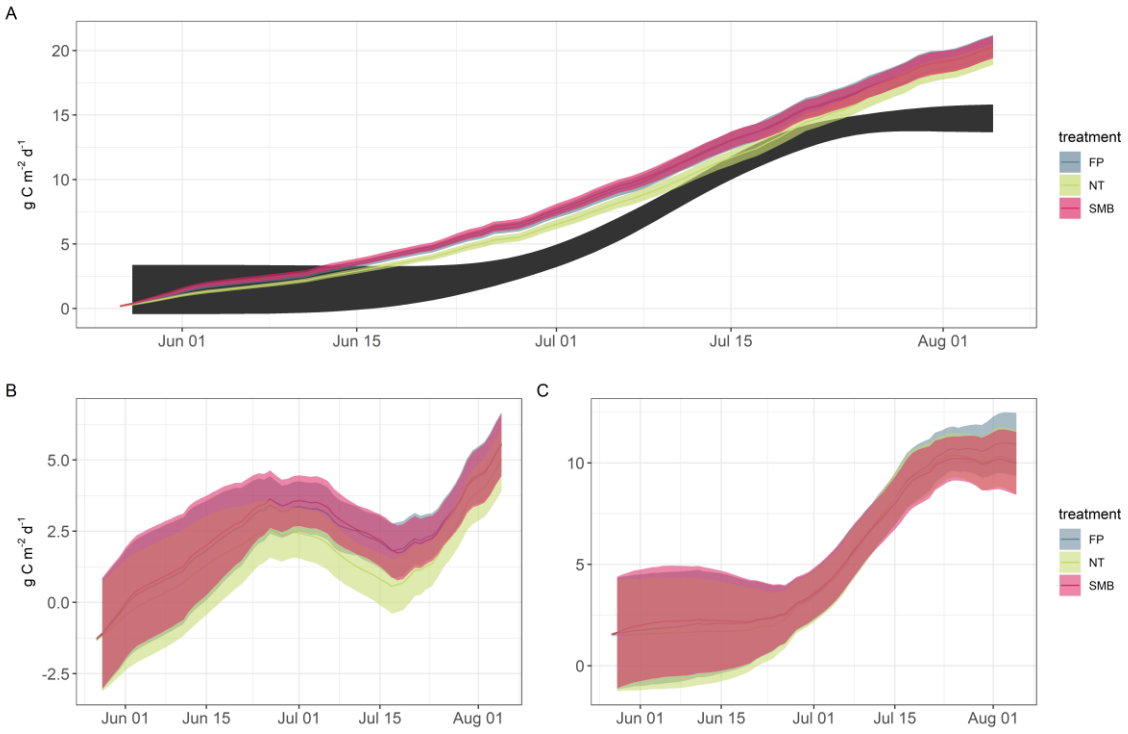

Figure 30. The fitted biomass of the canopy in terms of grams of carbon per meter squared (A) with the cumulative GPP values for each treatment. (B) Autotrophic respiration and (C) Heterotrophic respiration. Note the slightly higher values of heterotrophic respiration.

Conclusion and Discussion

The FVS approach to partitioning eddy covariance fluxes was successfully implemented. Using a deep neural network to impute missing values for the fluxes was also designed. The PNN was able to quantify the aleatoric uncertainty of the fluxes. The fluxes were aggregated and found that the SMB treatment had significantly higher NEE values than the other two treatment for the entire 2017-2018 study period. Over two years the SMB practice, emitted more 15.92 (14.46, 17.35) daily grams of carbon per square meter more than the inorganic fertilizer 5.29 (3.75, 6.78) daily grams of carbon per square meter. Over the two years the no-till strip sequestered the most NEE -0.94 (-2.32, 0.44). Over the two years the SMB emitted more R_e 118.83 (118, 119.7) than either the no- till 96 (95.34, 96.64) or the FP 113.33 (112.49, 114.17). On a GPP level the FP slightly had lower values than the SMB -105.17 (-106.65, -103.63) vs -106.3 (-107.93, -104.74) daily grams of carbon per square meter for the FP and the SMB respectively. The no-till had the highest GPP value at -96.99 (-98.43, -95.58). The no-till was the only treatment to net sequester because it gained as much carbon as it emitted. The SMB had 12 percent more R_e for every GPP gained for the no till strip while the FP was half that rate. Even though the no-till had less productive GPP, its yield was not affected. Promisingly, the no-till strip's yield was either competitive (2017) with the other treatments or it outperformed the treatments (2018).

On a more granular seasonal scale, for the two maize growing seasons, the no-till strip sequestered the most carbon dioxide at -2.58 (-3.23, -1.9) [2017] and -6.54 (-7.65, -5.45) [2018] daily grams of carbon per meter squared compared to the farmer practice of -0.36 (-1.11, 0.43) [2017] and -2.66 (-3.91, -1.34) [2018] for the farmer practice and 2.31 (1.54, 3.1) [2017] and -2.93 (-4.07, -1.79) [2018] daily grams of carbon per square meter for the SMB application. This is due by lower R_e values which is supported by the partitioning results. The lower R_e values are most likely due to a lower oxgen environment and a slower mediation of nutrients via surface dominated decomposition. While this stands in agreement to conventional literature surrounding no-till agriculture, the no-till strip had higher evaporation losses during the second maize season. However, for the rest of the seasons the tilled sites routinely had higher evaporation losses. Based on the above ground biomass sampling the farmer practice had higher heterotrophic respiration, thus because there was no additional input of carbon as in the SMB application, the FP generated the most loss of carbon dioxide via heterotrophic respiration- at least until the maize reached R4. Furthermore, the farmer practice had higher loss of water during the fallow seasons than the no till and tilled SMB (Fig. 28). The maize above ground biomass for 2018 was analyzed using an Anova and Tukey honest significance test to find that there were no significant differences between treatments. The cross contamination of the fluxes due to footprint overlap will need to be addressed.

CHAPTER 3
GEOSTATISTICAL INTERPOLATION OF HIGH-RESOLUTION REMOTE SENSING IMAGERY AND FLUX UPSCALING

Abstract

Vegetation indices were estimated from a CubeSat constellations over the treatment area. The imputation was necessary to create daily continuous time series of the vegetation index. The imputation process used spatial random forests (RFsp) to impute values for missing days for high-resolution imagery. Finally, the seasonal temporal and spatial trends were examined to determine if there was any significant differences. The hypothesis testing was conducted by PARTS (Partitioned Autoregressive Time Series) and found only one fallow season to have significant differences. This method of using RFsp is a promising and infinitely flexible model to fuse remote sensing products and create high spatial and temporal resolution images.

Introduction

The specific objective for this chapter is to produce sub-weekly high-resolution vegetation indices for further analysis to integrate them with the eddy covariance variables. While unmanned aerial vehicle imagery (UAV) would be the preferred way to derive these indices, due to research constraints the imagery used had to originate from orbital sensors.

This process of interpolating remote sensing imagery lies within the fields of image fusion and geostatistical statistics. An overview of these methods will be presented below. Followed by the justification for the choice of the statistical approach. Finally, the chapter will conclude with the results of the chosen method and spatio-temporal hypothesis tests for various treatment effects. Combining information from multiple remote sensing products is a challenging but fruitful endeavor.

Background

In the past, image fusion techniques have been used to generate high temporal and spatial resolution images for time series analysis. Th approach is dedicated to enhancing spatial resolution and to combining multimodal input images (e.g., pansharpening or intensity-hue-saturation (IHS) transform (Tu et al., 2001). Recently, the focus of these methods has changed to fusing fine spatial resolution images with high temporal frequency images. The following will review some past and future data fusion methods with a special focus on spatio-temporal interpolations.

Image fusion can be executed at various levels of data abstraction. Data fusion can be calculated at the pixel level, and the feature level (such as land cover classification). These methods use spatial information from the fine spatial resolution images and temporal information from coarse resolution satellite images to generate high spatial-temporal images. Spatio-temporal image fusion methods need some preprocessing to generate high spatiotemporal images: both coarse and fine-resolution radiance must be atmospherically corrected; the images must be co-registered; the images have to be geometrically corrected

and finally one of the existing spatiotemporal fusion methods is applied to generate images which are at an increased spatial and temporal resolution (Schmitt and Zhu, 2016). There are many types of categories and methods for spatiotemporal image fusion: reconstruction-based, unmixing, and learning-based. This paper will only discuss the reconstruction-based method.

Reconstruction-based method

Reconstruction-based spatiotemporal methods are also called filter-based methods or weighted-function-based and essentially generate synthetic spectral reflectance using the weighted sum of the neighboring pixels of the input image source (Schmitt and Zhu, 2016). A popular method is the Spatial and Temporal Adaptive Reflectance Fusion Model (STARFM) which is a reconstruction-based method (Gao et al., 2015).

STARFM predicts a fine-resolution image of the target date using a weighted neighborhood voting process. This method is effective, useful, and popular however there are some limitations. This method relies on the availability of cloud-free Landsat and MODIS images on concurrent dates. This method generates synthetic medium resolution images (30 m resolution) daily. The quality of the fused time series is dependent on the number of concurrent cloud-free course and medium resolution images. STARFM involves four main steps. First, coarse resolution images are co-registered and resampled to the resolution of the high spatial resolution images. Second, a moving window identifies spectrally similar pixels in the fine resolution images. Third, a weight is assigned to the homogeneous pixels based on the three criteria; the spectral difference between the surface reflectance of the images pair; the temporal differences in the dates of the images; finally, the Euclidean distance between the neighboring and the pixel of interest are calculated and used as dependent variables (Gao et al., 2015).

Because the quality of the fused time series is dependent on the number of concurrent cloud-free course and medium resolution images. This is very impractical and complicated. A promising method that functions as a gap-filling and image fusion model is Satellite dAta IntegRation (STAIR) (Luo et al., 2018). STAIR can ingest a time series that consists of an arbitrary number of Landsat and MODIS image pairs. It then systematically integrates the available information from the time series for missing-pixel imputation, and automatically determines the weight that each pair should contribute to the data fusion for a target date. By integrating the data in the time series, effectively their method can fuse a fine-resolution image without any unfilled pixels. This method is very promising, and it was effectively used with Landsat 7 with the infamous scan-line failure (Luo et al., 2018).

Spatio-Temporal Interpolation

STARFM has increasing difficulty in creating synthetic images when missing values (cloud cover) are present. Much like the STAIR procedure, there

have been plenty of procedures to gap-fill missing values in remote sensing imagery. The spatio-temporal interpolations do not have to be distinct from image fusion approaches they are rather complementary. For example, creating interpolated datasets can use a single platform sensor or a diverse set. Regardless, the procedures can exploit the temporal, spatial or spatio-temporal dependence structure latent in the data.

The contrasting methods of Consistent Adjustment of the Climatology to Actual Observations (CACAO) and Harmonic Analysis of Time-Series (Roerink et al., 2000; Verger et al., 2013) are united under the framework on only using the temporal information between images. CACAO was proposed as a noise reduction and a gap filler in time series by fitting the seasonal climatological patterns to the actual observations. The method looks at seasonal patterns of individual pixels and derives phenological models which is then used to fill gaps and smooth the time series. CACAO has two parameters (shift and scale) for each season which can be adjusted to quantify shifts in the timing of seasonal phenology and inter-annual variations in magnitudes. The method was originally tested on the Advanced Very High-Resolution Radiometer (AVHRR) with competitive results to widely used methods implemented in the TIMESAT toolbox (Jönsson and Eklundh, 2004). HANTS was developed to deal with time series of irregularly spaced observations and to identify and remove cloud contaminated observations and to create cloud-free images during arbitrary moments in time. HANST uses a fast Fourier transform (FFT) to identify the most significant frequencies in individual pixels. A curve-fitting procedure fits the phase and amplitude to the frequencies which then can be used to interpolate the pixel. HANTS was also tested on the AVHRR datasets (Roerink et al., 2000).
The above methods work well, especially for course resolution datasets. However, better interpolation using statistical methods such as co-kriging can use the information for neighboring pixels to improve predictions of missing values (Rossi et al., 1994; Zhu et al., 2015). Kriging can use incomplete and noisy data to obtaining optimal prediction and uncertainty estimates. Unfortunately, there are high computational costs, and it is impractical to implement for large data-sets (Zhu et al., 2015).

Combining both temporal and spatial interpolation approaches appear to be the most defensible approach since it takes into effect both the spatial and temporal correlation of the pixel values. A flexible and robust method used a hybrid Generalized Additive Model (GAM)-statistical space-time model which including the fitting of a temporal trend and a spatial component to account for local details supported by information in covariates (Poggio et al., 2012). Another approach used a window regression demonstrating superior performances to common phenotypical interpolation techniques such as mean value iteration and Savitzky-Golay techniques. The spatial window is represented by eight pixels neighboring the pixel under evaluation, and the temporal window selects a set of dates close to the date of interest. In short, the window regression, can estimate

the value of the pixel, based on regression analysis selected by a spatial-temporal window (Oliveira et al., 2014).

A third example for using spatio-temporal interpolation chooses spatio-temporal subsets around missing values, estimates empirical quantiles characterizing the missing values and predicts missing values through quantile regression (Gerber et al., 2018). This method overcomes some shortcomings of the above models. Some of the issues are that when there are large gaps of missing values (such as whole days); others such as co-kriging are difficult to scale to size and are computational and memory intensive. This improved method is available as an open-source package *gapfill* and is extremely efficient and parallelizable. The *gapfill* method was able to predict all missing, values in data sets with large proportions of missing values (up to 50%). Second, the predicted values reconstruct the spatial and temporal patterns of NDVI data sets with close to no loss of details (Gerber et al., 2018). The *gapfill* method will be one of the interpolation methods pursued for the remainder of this paper. There are a couple of limitations to this approach, first, the method assumes the data are regularly spaced through time and it requires some known values on the data with up to 50% missing values. These values will have to originate from a different platform.

Finally, a more flexible but more computationally complex method will be assessed. One such technique uses a Random Forest to generate spatial and spatiotemporal predictions competitive to traditional geostatistical techniques. This technique (RFsp) is useful and flexible as it can direct use non-spatial covariates, and it can handle irregularly spaced datasets in time as well as missing values within individual images. Furthermore, it makes direct use of geographical locations to fit the models (Hengl et al., 2018). RFsp uses buffer distances from observation points as covariates and so consequently incorporates geographical proximity effects into the prediction process. Hengl et al's. paper demonstrated RFsp obtains competitive and accurate predictions as most geostatistical kriging techniques. Furthermore, because RFsp uses random forests it is non-parametric and thus does not need to meet the same statistical assumptions needed in kriging (Hengl et al., 2018). Unfortunately, it is very inefficient for large datasets but clever ways to circumvent these limitations will be addressed.

Methodology

Data Sets and Preprocessing

The specific objective for this research is to have sub-weekly high-resolution vegetation indices for further analysis to integrate them with the eddy covariance variables. The high-resolution remote sensing images were obtained from Planet Labs (PlanetScope; Planet Labs, Inc., San Francisco, USA). The planet-scope images were orthorectified and atmospherically corrected using the 6s algorithm (Vermote et al., 1997). All images were co-registered to a 1 m NAIP

image from 2016. Further covariates to interpolate the high-resolution data will be green index time-lapse photography and photothermal time and metadata from the CubSat acquisition timing. Partial cloud contamination was manually masked and the remaining pixels were kept.

Data summary

In total, 193 images were used. Images were masked depending on the cloud cover. Solar altitude varied by from 23 to 69 degrees with median values of 47.4. View angles varied from 0 degrees (nadir) to 5 degrees with a median value of 0.7 degrees. There were approximately five days where multiple images were taken. For a graphical summary see Fig. 31.

Model fitting and interpolation

While other remote sensing products such as the 250m MOD09GQ NDVI (Vermote and Wolfe, 2015) could be used as a covariate during the time of analysis, there was too much cloud cover to impute the contaminated data. There could be other areas and seasonal trends that could make this technique practical. To make the RFsp approach practical, the space-time cube was divided into 190 overlapping circles with radii of 11 meters. The buffer distance acts as a covariate to capture the spatial autocorrelation of the NDVI values. Each circular window was individually modeled and the prediction for specific dates was constructed see Fig. 37. The outputs were mosaiced and values were averaged together using inverse variance weighting.

The Green Chromatic Coordinate (GCC) is a proportional measure of the relative brightness of the green channel. It is calculated:

$$GCC = \frac{\text{Green}_{DN}}{\text{Red}_{DN} + \text{Green}_{DN} + \text{Blue}_{DN}}$$

Where *Red* $_{DN}$, *Green* $_{DN}$, and *Blue* $_{DN}$ are the red, green, and blue color channels respectively. The trail camera represents the color as digital numbers (DN) stored in the high resolution (8 MGP) JPEG format. Figure 2**Error! Reference source not found.** illustrates the behavior of GCC over the two years of measurement (Burke and Rundquist, 2021).

Photothermal time is the product of growing degree days and day length (see Masle et al., 1989). Photothermal (K_P) time is defined as:

$$K_P = \sum_{i=1}^{n} l_i \left(\overline{(Ta_i)}\right)$$

Where *i* is the day, T_a is the average daily air temperature and *l* is the light period as a proportion of a day. Other variables were solar altitude and solar azimuth at which time the image was taken the satellites angle as well to the image plane. Finally, various terrain indices were included see Fig. 32. The hope with these variables is to standardize the predicted image to remove the confounding effects that could add to the noise of the NDVI. In effect, the hope was to correct for any Bi-directional Reflectance (BRDF) effects (see for example, Roy et al. (2016)).

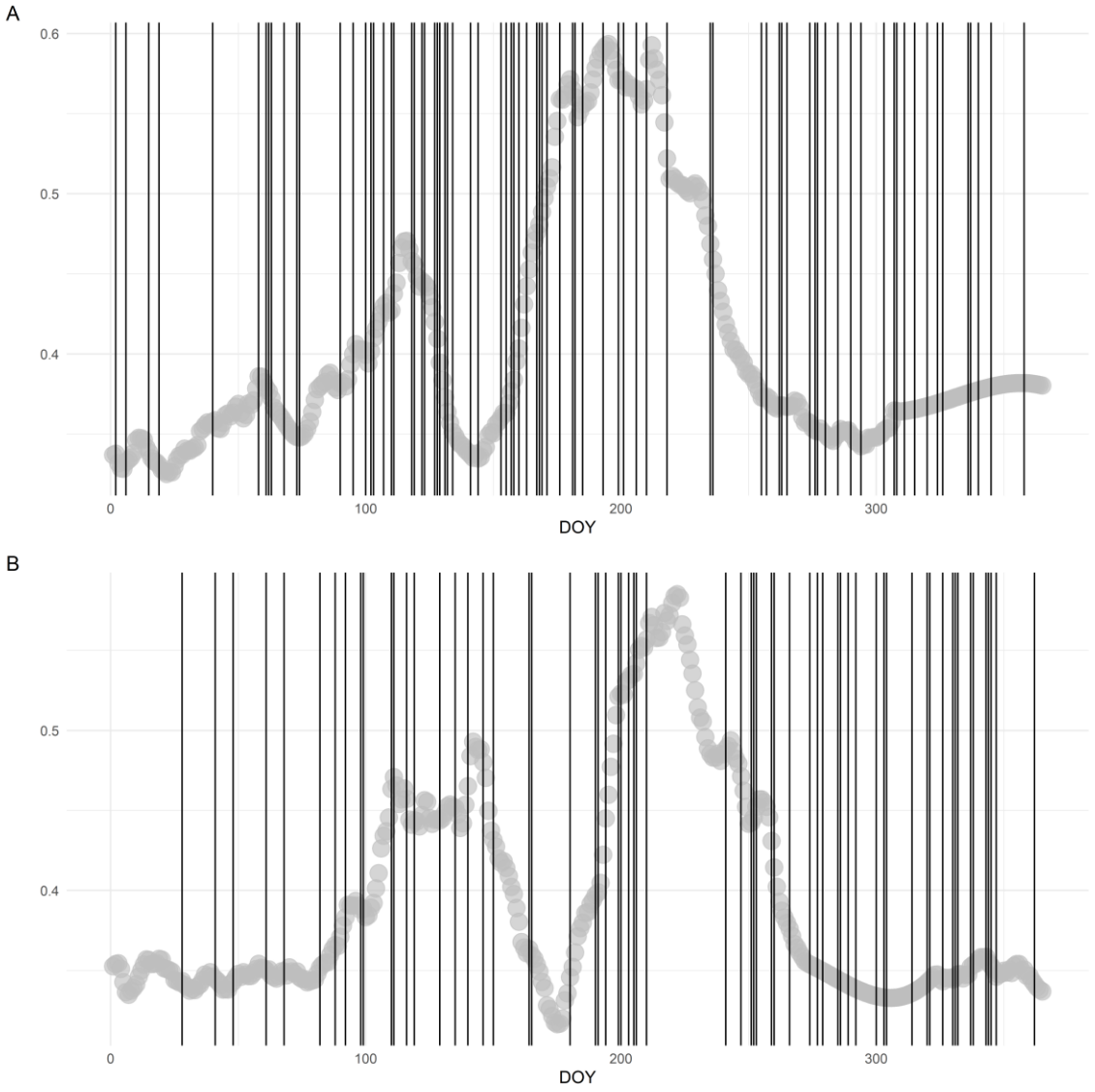

Figure 31. Graphical summary of CubeSat acquisitions (vertical lines). The GCC values are plotted in light gray for reference. A. is for 2018 and B 2017.

The variables chosen were elevation, slope, aspect, eastness, northness, topographical position index (TPI) and curvature. Aspect is defined as the compass direction or azimuth that a terrain surface faces. Curvature here estimated uses McNab's (1993) surface curvature index. The TPI measures the difference between elevation at a central point and the average elevation around it within a specified radius. When the TPI is positive the point is located higher than its average surroundings (Reu et al. (2013)). Because most surface reflection is not isotropic but rather the reflectance depends on direction of solar incident radiation and the direction at which the satellite viewed it. This can explain why two images taken on the same day but at different times and at different view angles the reflectance product will have different values. Using the terrain indices and the position of the sun and angle of the satellite, the hope was for the RFsp model to explain the induced variability. When predicting the images, the solar altitude was fixed to solar noon and the satellite view angle to be perfectly nadir.

Results of the Geospatial Random Forest

The hyperparameters such as circle radii, number random forest trees, minimal node size, and maximal tree depth were tuned via cross validation and with respect to computational ease. The average overall out of bag prediction error was 0.0017 mean square error or a root mean square (RMSE) of 0.04. The coefficient of determination ranged from 0.72 to 0.9 with a mean of 0.8.
Once the models had been fit the individual locations were predicted across time and then the 190 individual predictions were mosaiced into a final map. The outputs were mosaiced together using inverse variance weighting produced by the prediction uncertainties. The goal of this section was not to perfectly predict the images but to standardize to nadir view 'acquired' at solar noon images the actual predicted values were not needed to compare with the actual measured observations.

Spatio Temporal Statistical Inference of the Interpolated images

The procedure from, Ives et. al, (2021) will be used to assess if there were any treatment effects (the boundaries can be seen in Fig. 3). The procedure, PARTS (Partitioned Autoregressive Time Series), will be briefly explained. A common approach when studying patterns in space and time is to perform pixel scale analysis. However, with respect to Tobler's first law of geography, trends found in neighboring pixels should not necessarily be treated independently. The problem then becomes what distance are pixels independent.
PARTS separately analyzes the time series for each pixel to calculate parameter estimates that quantify the trends in time, then regression is used to analyze the spatial distribution of the parameter estimates. The regression on the temporal parameters is performed using generalized least squares (GLS) (Dielman, 1986; Ives and Zhu, 2006). First, to account for temporal

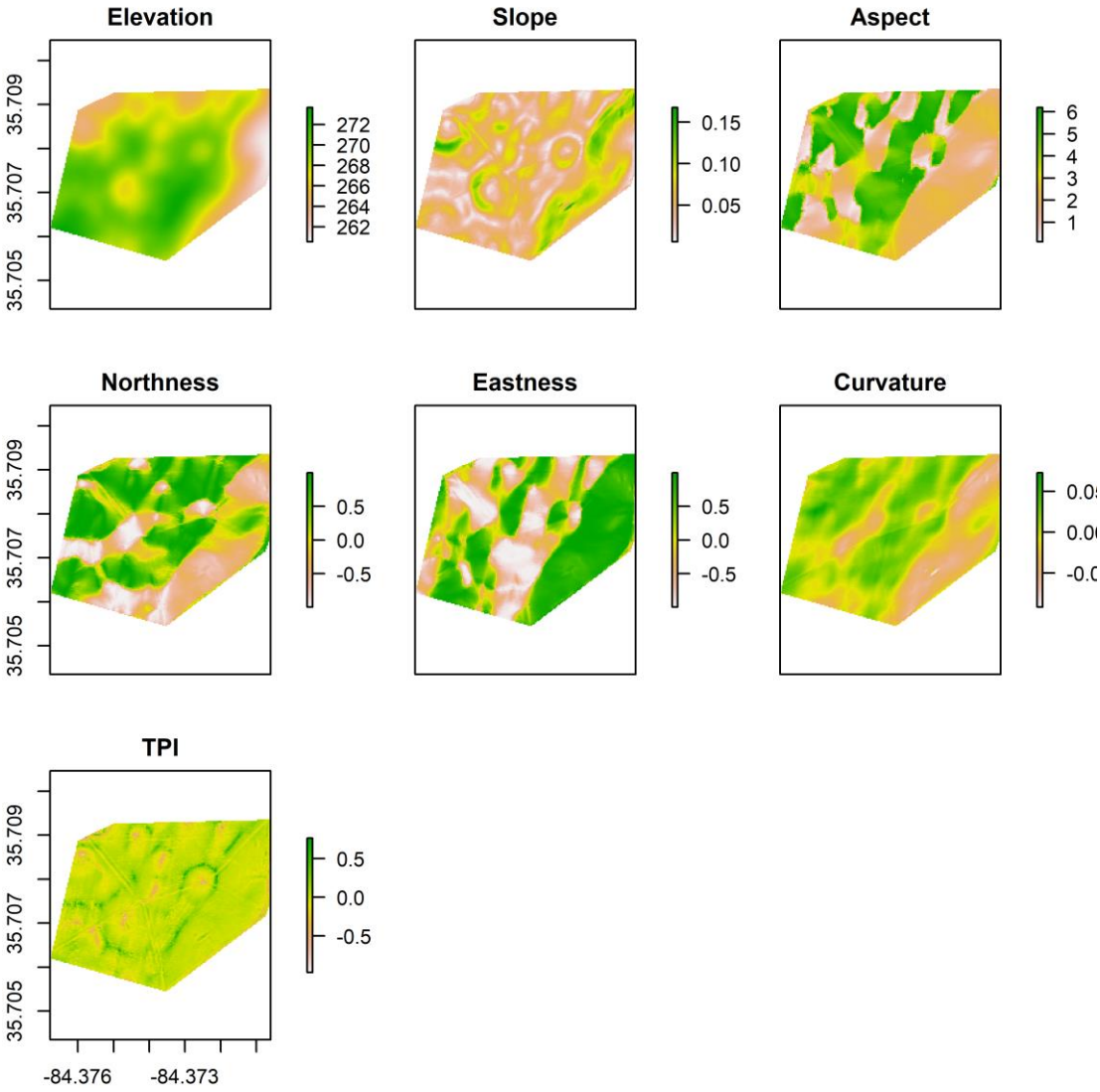

Figure 32. Visualization of additional topographical variables in the spatial random forest model. TPI: topographic position index. Elevation in meters (a.s.l), slope, aspect, eastness, and northness are in radians. TPI unitless and curvature unitless.

autocorrelation pixel-level time series were fit using a linear model with first-order Gaussian auto-regressive process errors. The coefficients of this model are then used as the values to be estimated. Next in the process the correlations between the residuals of the time-series model are used to estimate the spatial autocorrelation structure of the estimates. Using the spatial autocorrelation structure, a spatial GLS regression is performed against the temporal parameters. Hypothesis tests are conducted depending on the variables included the GLS regression. For more details, please refer to (Ives et al., 2021).

PARTS Results and Discussion

Four seasons were analyzed. The first season where the field remained under a no-tillage practice was from January 2017 to application of herbicide (5/30/2017). A subsample of estimates can be seen in Figs. 33 to 35. The second started after the crop emerged (2017/06/21) and ended when the crop pollen dropped (2017/08/12). The third season started in January of 2018 and ended prior to herbicide application. Finally, the fourth season (5/27/2018 - 7/12/2018) the second maize crop was analyzed until pollen shed and found no significant differences through time and between treatment effects (see Table 9 and 12). For season 1, the first fallow, both estimates for soil amendment vs conventional fertilizer were significantly different from zero using the test t-tests around the estimated (Table 10). However, the F-Test (Table 9) found no significant differences between treatments. While the farmer practice (FP) has a slightly higher trend than the SMB application but, according to the F-test, the treatments do not differ among each other. Examining Fig. 33, there are certainly difference in variability during the first season. For example, the eastern facing slope toward the southwest had higher NDVI values, as well as at the boundary of the SMB application. Regardless the variability between groups must have been lower then within the treatment groups. During the first maize growth, (Fig. 34) there was no differences (Table 9 and 11). This is rewarding as the adding fertilizer and amendments enough nutrient supply to sufficiently satisfy the nutrient demands of the crop. Applying fertilizer and the TilthMax3G were thus able to supply nutrients to the crop at competitive rates as the tilled surfaces. This results also agrees with the partitioning analysis. As the no till treatments had a slightly less cumulative sum, than the other treatments, the overlap of the confidence intervals was at its greatest. The third season (Fig. 35) possessed the only significant difference between treatments (Table 9 and 12). The differences are clearly visible in Fig 35. First the no-till is visible up until April 2018, with higher NDVI values, however no significance was found within the no-till treatment rather or the interaction effect, however differences within SMB and FP were deemed significant. The SMB was much greener, with a patchy surface in contrast to the FP treatment. This response is supported by the partitioning results, where the GPP (see Fig 27c) was higher for the second fallow season.

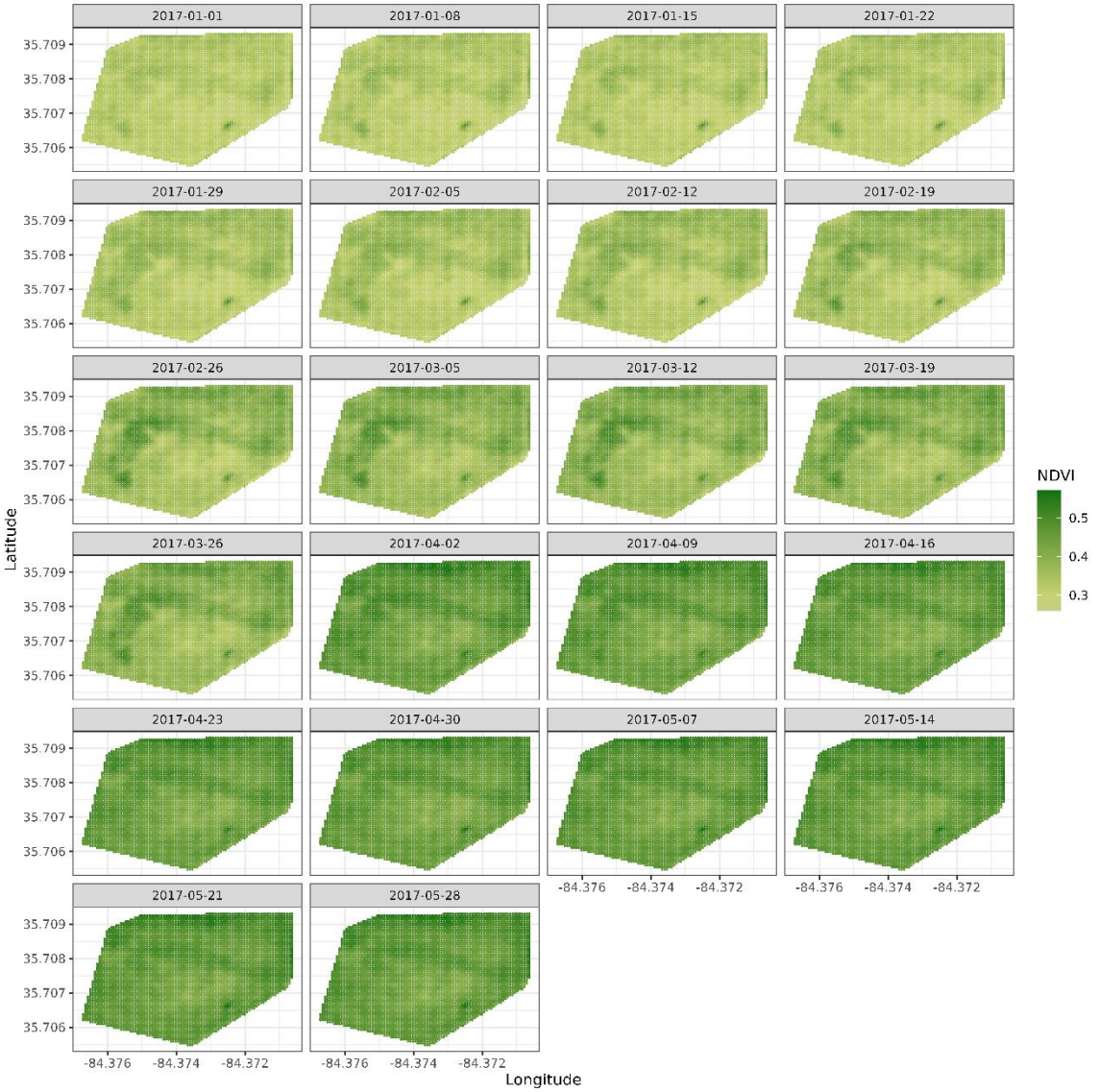

Figure 33. Samples from the predicted NDVI for the first season (Fallow) (1/1/2017-5/30/2017).

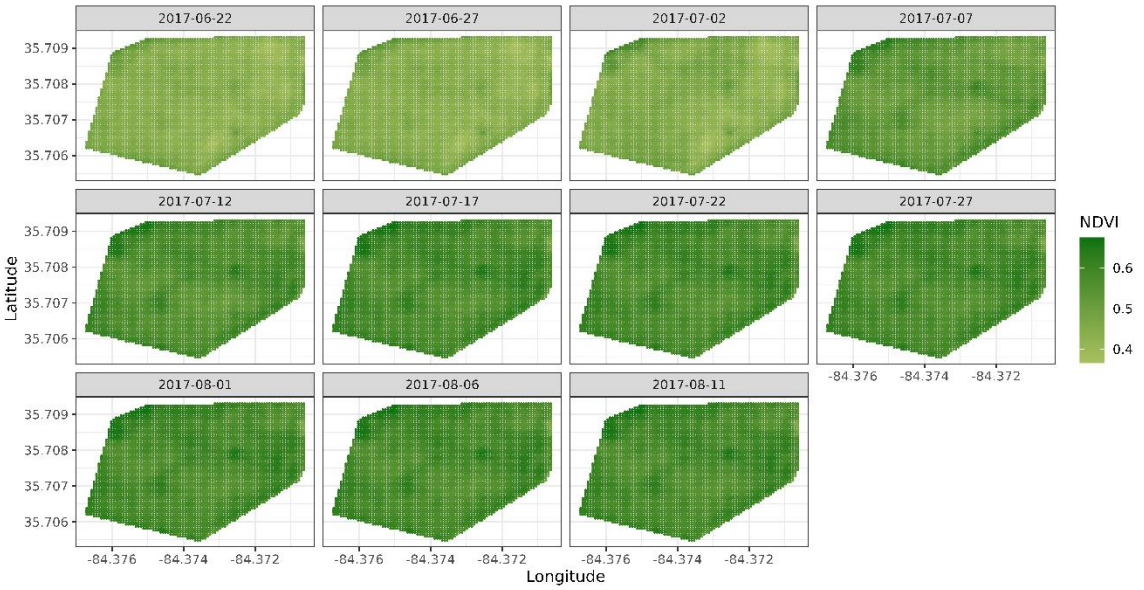

Figure 34. Samples from the predicted NDVI for the second season (Maize) (6/21/2017-8/12/2017).

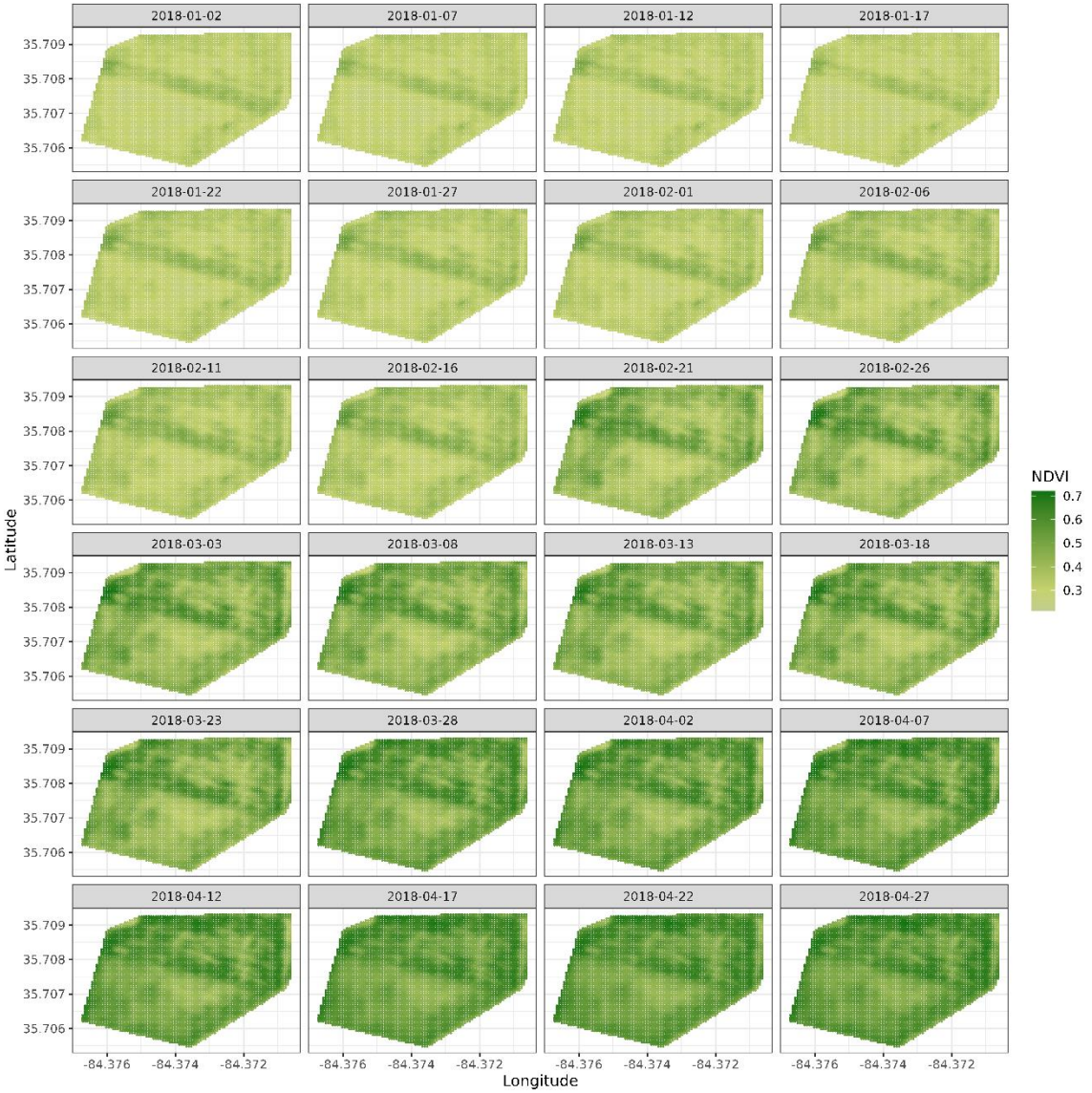

Figure 35. Samples from the predicted NDVI for the third season (Fallow) (1/1/2018-4/27/2018).

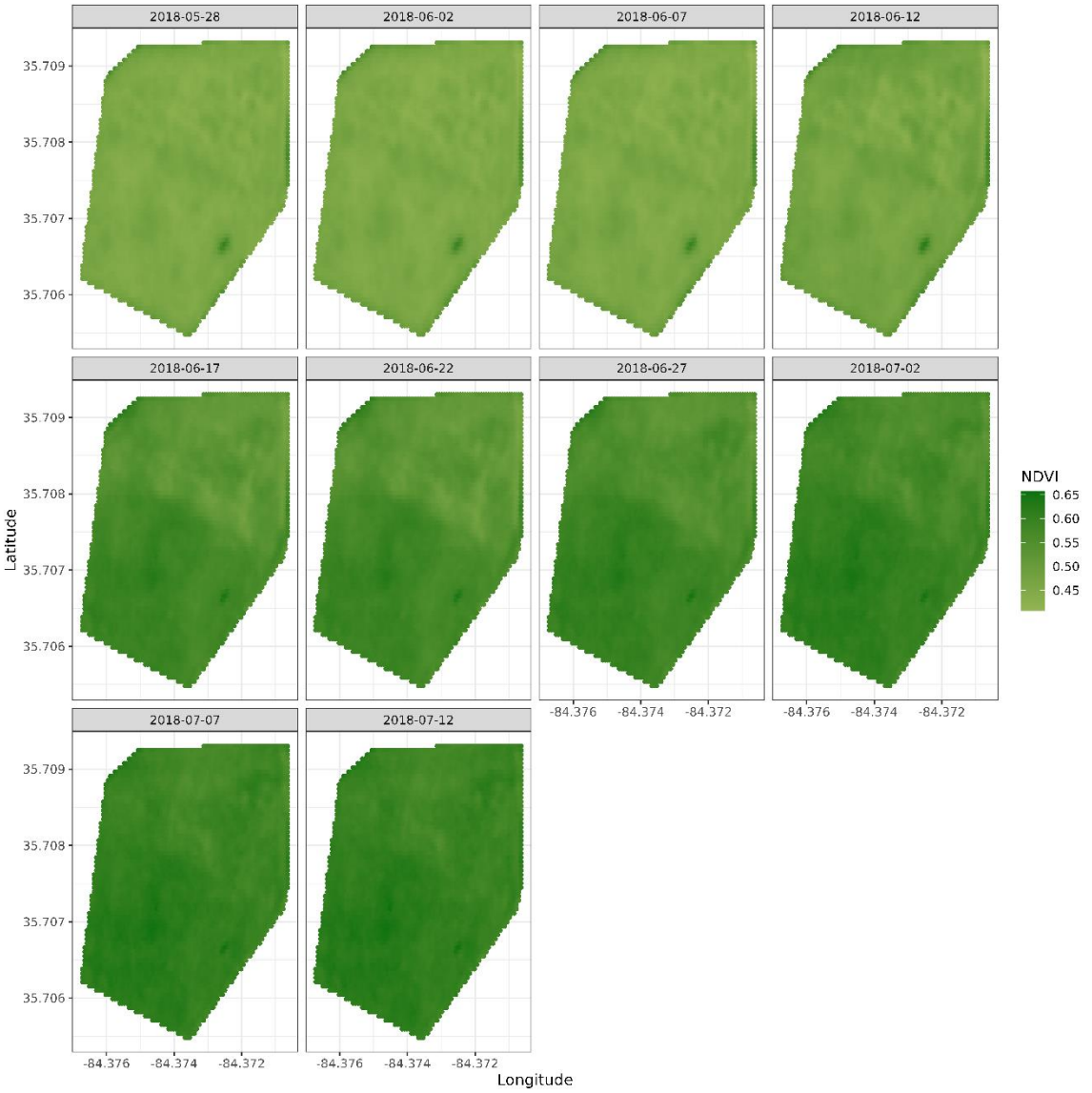

Figure 36. Samples from the predicted NDVI for the fourth season or second season of Maize (5/27/2018-7/12/2018).

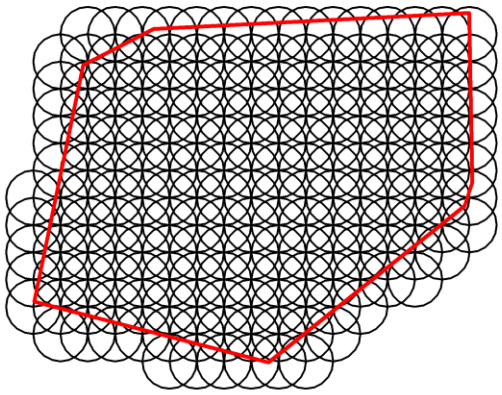

Figure 37. The 190 segments used to individual train multiple RFsp models. The radii of the circles are approximately 11 meters.

Table 9. F values to test significance. Only season 3 (the second fallow) demonstrated differences within groups.

	Df	Sum Sq	Mean Sq	F value	Pr(>F)
Season 1	1	0.39	$8.18\ 10^{-5}$	2.11	0.1464
Season 2	3	4.054	$8.6\ 10^{-4}$	2.83	0.03681
Season 3	3	0.3425	$7.242\ 10^{-5}$	2.93	0.0323
Season 4	3	1.039	$2.2\ 10^{-4}$	2.282	0.07707

Table 10. T test for coefficients for Season 1. Both estimates are significantly different from zero meaning that there are significant temporal trends. The farmer practice (FP) has a slightly higher trend than the SMB application but according to the F-test table

Treatment	Estimate	t value	Pr(>t)
FP	0.01607	2.111	0.0348
SMB	0.01584	2.082	0.03739

Table 11. T test for season 2 where there was the first crop of maize. There coefficients were not significantly different from zero.

Treatment	Estimate	t value	Pr(>t)
FP	-0.0112381	-0.3928	0.69451
SMB	-0.0105490	-0.3687	0.71237
NT	-0.0001013	-0.4281	0.66863
SMB*NT	-0.0005575	-1.6752	0.09395

Table 12. T test for coefficients for Season 3 when there was a second of Fallow growth. Only the FP and SMB are significant. And according to the F Test they are statistically different from each other.

Treatment	Estimate	t value	Pr(>t)
FP	0.02092	3.4748	0.0005159
SMB	0.02109	3.5036	0.0004633
NT	$-1.422\ 10^{-4}$	-0.7284	0.4663899
SMB*NT	$-3.734\ 10^{-4}$	-1.3963	0.1626754

Table 13. T test for coefficients for Season 4 when there was a second of Maize growth. There is no trend in time and none of the treatments are significantly different.

Treatment	Estimate	t value	Pr(>t)
FP	$-5.988\ 10^{-3}$	-0.4789	0.6320
SMB	$-5.411\ 10^{-3}$	-0.4328	0.6652
NT	$-2.526\ 10^{-4}$	-1.0291	0.3035
SMB*NT	$-9.564\ 10^{-5}$	-0.2844	0.7761

Finally, for the second maize season (see Fig. 34) there were no statistical differences between treatments. Again, supporting the results from the above ground biomass and the overlapping confidence intervals for GPP, R_e and NEE in Fig. 27D around beginning of July 2018.

Conclusion

Using spatial random forests to impute values for missing days for high-resolution imagery is promising. This study could be improved by assessing and potentially correcting where systematic biases occur. This method of using RFsp is a promising and infinitely flexible model to fuse remote sensing products and create high spatial and temporal resolution images. The RFsp model was able to empirically account for BRDF effects. The predicted images then can be used in many other models. Furthermore, the predicted farm was used with spatio-temporal hypothesis tests. Using PARTS hypothesis testing effectively found only one season where the NDVI values differ through time and treatment. As noted in the Introduction, this difference can be more of a function of the lower pH values and its imposition on vegetation structure.

CONCLUSION

The first chapter on developing a segmented planar fit found that variables such as day of the year and wind direction indicated greater explanatory power for some coordinate systems while other variables such as stability and wind speed had inconsistent impacts on coordinate system sheds light on the effects of these systems. Most importantly it found that even in complex landscapes, using simple unrotated fluxes or the segmented planar fit is preferable to double rotation.

Once the proper coordinate system was found, the fluxes were then partitioned using the flux variance similarity approach. To find continuous sums, a probabilistic deep neural network was developed and successfully trained to impute missing values for the fluxes. Over the two years, the no-till was the only treatment to net sequester because it gained as much carbon as it lost. The SMB had 12 percent more R_e for every GPP gained for the no till strip while the FP was half that rate. Because the SMB emitted the most carbon over the two years, we do see the paradoxical effect that application of TilthMax3G increases emissions due to higher microbial turnover rates and plant production.

For the two maize growing seasons, the no-till strip sequestered the most carbon at -2.58 (-3.23, -1.9) [2017] and -6.54 (-7.65, -5.45) [2018] daily grams of carbon compared to the farmer practice of -0.36 (-1.11, 0.43) [2017] and -2.66 (-3.91, -1.34) [2018] for the farmer practice and 2.31 (1.54, 3.1) [2017] and -2.93 (-4.07, -1.79) [2018] daily grams of carbon per square meter for the SMB application. According to the FVS results this is due by lower R_e values. The lower R_e values are most likely due to a lower oxygen environment and a slower mediation of nutrients via surface dominated decomposition. While this stands in agreement to conventional literature surrounding no-till agriculture, the no-till strip oddly had higher evaporation losses during the second maize season. However, for the rest of the seasons the tilled sites routinely had higher evaporation losses. Based on the above ground biomass sampling the farmer practice had higher heterotrophic respiration, thus because there was no additional input of carbon as in the SMB application, the FP generated the most loss of carbon dioxide via heterotrophic respiration at least until the maize reached R4. Furthermore, the farmer practice had higher loss of water during the fallow seasons than the no till and tilled SMB. The cross contamination of the fluxes due to footprint overlap will need to be addressed.

Vegetation indices was estimated from a CubeSat constellation over the treatment area. The imputation process used spatial random forests to impute values for missing days for high-resolution imagery is promising. Using PARTS (Partitioned Autoregressive Time Series) to determine any treatment effects, found only the 2018 spring fallow season had significantly different NDVI values between the SMB and FP. The SMB was much greener (higher NDVI values), with a patchier surface in contrast to the FP treatment. This response is supported by the partitioning results, where the GPP (see Fig 27c) was higher for

the second fallow season. The simplest explanation is caused by the lower soil pH values on the SMB treatment encouraging a different vegetation community.

The remaining research topics within this small area agricultural situations with contrasting site management, is to integrate the, high resolution NDVI and partitioned fluxes to upscale the fluxes to daily field scale fluxes. This research will address the cross contamination of the fluxes due to footprint overlap. The personal research of the author found that given an analytical footprint dispersion model and the NDVI, a conditional variational autoencoder can successfully infer the source flux area. PARTS can be used to conduct further hypothesis tests to see if the different treatment effects can be detected than the results found here.

This dissertation provides novel application of remote sensing, probabilistic deep learning imputation, flux partitioning and proper coordinate rotation of wind velocities to support that no-till systems with added soil amendments are the best ways to preserve soil organic matter on a two-year basis. The study also highlights possible sources of errors and deficiencies when using eddy covariance to monitor sequestration of carbon dioxide over agricultural fields.

REFERENCES

Abadi, M., Agarwal, A., Barham, P., Brevdo, E., Chen, Z., Citro, C., Corrado, G.S., Davis, A., Dean, J., Devin, M., Ghemawat, S., Goodfellow, I., Harp, A., Irving, G., Isard, M., Jia, Y., Jozefowicz, R., Kaiser, L., Kudlur, M., Levenberg, J., Mané, D., Monga, R., Moore, S., Murray, D., Olah, C., Schuster, M., Shlens, J., Steiner, B., Sutskever, I., Talwar, K., Tucker, P., Vanhoucke, V., Vasudevan, V., Viégas, F., Vinyals, O., Warden, P., Wattenberg, M., Wicke, M., Yu, Y., Zheng, X., 2015. TensorFlow: Large-scale machine learning on heterogeneous systems.

Abdar, M., Pourpanah, F., Hussain, S., Rezazadegan, D., Liu, L., Ghavamzadeh, M., Fieguth, P., Cao, X., Khosravi, A., Acharya, U.R., Makarenkov, V., Nahavandi, S., 2021. A review of uncertainty quantification in deep learning: Techniques, applications and challenges. Information Fusion 76, 243–297. https://doi.org/10.1016/j.inffus.2021.05.008

Abdar, M., Pourpanah, F., Hussain, S., Rezazadegan, D., Liu, L., Ghavamzadeh, M., Fieguth, P., Cao, X., Khosravi, A., Acharya, U.R., Makarenkov, V., Nahavandi, S., 2021. A review of uncertainty quantification in deep learning: Techniques, applications and challenges. Information Fusion 76, 243–297. https://doi.org/10.1016/j.inffus.2021.05.008

Baldocchi, D., 2014. Measuring fluxes of trace gases and energy between ecosystems and the atmosphere - the state and future of the eddy covariance method. Global Change Biology 20, 3600–3609. https://doi.org/10.1111/gcb.12649

Baldocchi, D., 2014. Measuring fluxes of trace gases and energy between ecosystems and the atmosphere - the state and future of the eddy covariance method. Global Change Biology 20, 3600–3609. https://doi.org/10.1111/gcb.12649

Baldocchi, D.D., Hincks, B.B., Meyers, T.P., 1988. Measuring biosphere-atmosphere exchanges of biologically related gases with micrometeorological methods. Ecology 69, 1331–1340. https://doi.org/10.2307/1941631

Bowden, R.D., Davidson, E., Savage, K., Arabia, C., Steudler, P., 2004. Chronic nitrogen additions reduce total soil respiration and microbial respiration in temperate forest soils at the harvard forest. Forest Ecology and Management 196, 43–56. https://doi.org/10.1016/j.foreco.2004.03.011

Burke, M.W.V., Rundquist, B.C., 2021. Scaling phenocam GCC, NDVI, and EVI2 with harmonized landsat-sentinel using gaussian processes. Agricultural and Forest Meteorology 300, 108316. https://doi.org/10.1016/j.agrformet.2020.108316

Burton, A.J., Pregitzer, K.S., Crawford, J.N., Zogg, G.P., Zak, D.R., 2004. Simulated chronic NO3 deposition reduces soil respiration in northern

hardwood forests. Global Change Biology 10, 1080–1091. https://doi.org/10.1111/j.1365-2486.2004.00737.x
Campbell, G.S., Norman, J.M., 2000. An introduction to environmental biophysics. Springer Science & Business Media.
Cheng, K., Ogle, S.M., Parton, W.J., Pan, G., 2013. Simulating greenhouse gas mitigation potentials for chinese croplands using the DAYCENT ecosystem model. Global Change Biology 20, 948–962. https://doi.org/10.1111/gcb.12368
Clemmensen, K.E., Bahr, A., Ovaskainen, O., Dahlberg, A., Ekblad, A., Wallander, H., Stenlid, J., Finlay, R.D., Wardle, D.A., Lindahl, B.D., 2013. Roots and associated fungi drive long-term carbon sequestration in boreal forest. Science 339, 1615–1618. https://doi.org/10.1126/science.1231923
Cowan, I.R., IR, C., GD, F., 1977. Stomatal function in relation to leaf metabolism and environment.
Craine, J.M., Morrow, C., Fierer, N., 2007. MICROBIAL NITROGEN LIMITATION INCREASES DECOMPOSITION. Ecology 88, 2105–2113. https://doi.org/10.1890/06-1847.1
Diacono, M., Montemurro, F., 2010. Long-term effects of organic amendments on soil fertility. A review. Agronomy for Sustainable Development 30, 401–422. https://doi.org/10.1051/agro/2009040
Dielman, T.E., 1986. Elsevier.
Dupont, S., Patton, E.G., 2012. Influence of stability and seasonal canopy changes on micrometeorology within and above an orchard canopy: The CHATS experiment 157, 11–29. https://doi.org/10.1016/j.agrformet.2012.01.011
Farquhar, G.D., Von Caemmerer, S., Berry, J.A., 2001. Models of photosynthesis. Plant physiology 125, 42–45.
Finnigan, J., 2008. An introduction to flux measurements in difficult conditions. Ecological Applications 18, 1340–1350.
Gao, F., Hilker, T., Zhu, X., Anderson, M., Masek, J., Wang, P., Yang, Y., 2015. Fusing landsat and MODIS data for vegetation monitoring. IEEE Geoscience and Remote Sensing Magazine 3, 47–60. https://doi.org/10.1109/mgrs.2015.2434351
Gerber, F., Jong, R. de, Schaepman, M.E., Schaepman-Strub, G., Furrer, R., 2018. Predicting missing values in spatio-temporal remote sensing data. IEEE Transactions on Geoscience and Remote Sensing 56, 2841–2853. https://doi.org/10.1109/tgrs.2017.2785240
Glorot, X., Bordes, A., Bengio, Y., 2011. Deep sparse rectifier neural networks, in: Gordon, G., Dunson, D., Dudík, M. (Eds.), Proceedings of the Fourteenth International Conference on Artificial Intelligence and Statistics, Proceedings of Machine Learning Research. PMLR, Fort Lauderdale, FL, USA, pp. 315–323.
Goulden, M.L., Munger, J.W., Fan, S.-M., Daube, B.C., Wofsy, S.C., 1996. Measurements of carbon sequestration by long-term eddy covariance:

Methods and a critical evaluation of accuracy. Global change biology 2, 169–182.
Gove, J.H., Hollinger, D.Y., 2006. Application of a dual unscented kalman filter for simultaneous state and parameter estimation in problems of surface-atmosphere exchange. Journal of Geophysical Research 111. https://doi.org/10.1029/2005jd006021
Hansen, B.E., Seo, B., 2002. Testing for two-regime threshold cointegration in vector error-correction models. Journal of econometrics 110, 293–318.
Hanson, P., Edwards, N., Garten, C.T., Andrews, J., 2000. Separating root and soil microbial contributions to soil respiration: A review of methods and observations. Biogeochemistry 48, 115–146.
Hastie, T., Tibshirani, R., Friedman, J.H., Friedman, J.H., 2009. The elements of statistical learning: Data mining, inference, and prediction. Springer.
Hengl, T., Nussbaum, M., Wright, M.N., Heuvelink, G.B.M., Gräler, B., 2018. Random forest as a generic framework for predictive modeling of spatial and spatio-temporal variables. PeerJ 6, e5518. https://doi.org/10.7717/peerj.5518
Hicks, B.B., Baldocchi, D.D., 2020. Measurement of fluxes over land: Capabilities, origins, and remaining challenges 177, 365–394. https://doi.org/10.1007/s10546-020-00531-y
Hothorn, T., Hornik, K., Zeileis, A., 2006. Unbiased recursive partitioning: A conditional inference framework. Journal of Computational and Graphical statistics 15, 651–674.
Hui, D., Wan, S., Su, B., Katul, G., Monson, R., Luo, Y., 2004. Gap-filling missing data in eddy covariance measurements using multiple imputation (MI) for annual estimations. Agricultural and Forest Meteorology 121, 93–111.
Ives, A.R., Zhu, J., 2006. Statistics for correlated data: Phylogenies, space, and time. Ecological applications 16, 20–32.
Ives, A.R., Zhu, L., Wang, F., Zhu, J., Morrow, C.J., Radeloff, V.C., 2021. Statistical inference for trends in spatiotemporal data. Remote Sensing of Environment 266, 112678. https://doi.org/10.1016/j.rse.2021.112678
Janzen, H.H., 2014. Beyond carbon sequestration: Soil as conduit of solar energy. European Journal of Soil Science 66, 19–32. https://doi.org/10.1111/ejss.12194
Jarvis, P., Massheder, J., Hale, S., Moncrieff, J., Rayment, M., Scott, S., 1997. Seasonal variation of carbon dioxide, water vapor, and energy exchanges of a boreal black spruce forest. Journal of Geophysical Research: Atmospheres 102, 28953–28966.
Jastrow, J.D., Miller, R.M., Owensby, C.E., 2000. Plant and Soil 224, 85–97. https://doi.org/10.1023/a:1004771805022
Jenkinson, D., 1966. The priming action. The Use of Isotopes in Soil Organic Matter Studies.

Jenkinson, D.S., Fox, R.H., Rayner, J.H., 1985. Interactions between fertilizer nitrogen and soil nitrogen-the so-called 'priming' effect. Journal of Soil Science 36, 425–444. https://doi.org/10.1111/j.1365-2389.1985.tb00348.x
Jenkinson, D.S., Fox, R.H., Rayner, J.H., 1985. Interactions between fertilizer nitrogen and soil nitrogen-the so-called 'priming' effect. Journal of Soil Science 36, 425–444. https://doi.org/10.1111/j.1365-2389.1985.tb00348.x
Jenkinson, D.S., Rayner, J.H., 1977. The turnover of soil organic matter in some of the rothamsted classical experiments. Soil Science 123, 298–305. https://doi.org/10.1097/00010694-197705000-00005
Johnson, D.W., Curtis, P.S., 2001. Effects of forest management on soil c and n storage: Meta analysis. Forest Ecology and Management 140, 227–238. https://doi.org/10.1016/s0378-1127(00)00282-6
Johnson, M.G., Levine, E.R., Kern, J.S., 1995. Soil organic matter: Distribution, genesis, and management to reduce greenhouse gas emissions. Water, Air, &amp$\mathsemicolon$ Soil Pollution 82, 593–615. https://doi.org/10.1007/bf00479414
Jönsson, P., Eklundh, L., 2004. TIMESATa program for analyzing time-series of satellite sensor data. Computers &amp$\mathsemicolon$ Geosciences 30, 833–845. https://doi.org/10.1016/j.cageo.2004.05.006
Katul, G.G., PALMROTH, S., OREN, R., 2009. Leaf stomatal responses to vapour pressure deficit under current and CO₂-enriched atmosphere explained by the economics of gas exchange. Plant, Cell &amp$\mathsemicolon$ Environment 32, 968–979. https://doi.org/10.1111/j.1365-3040.2009.01977.x
Keenan, T.F., Migliavacca, M., Papale, D., Baldocchi, D., Reichstein, M., Torn, M., Wutzler, T., 2019. Widespread inhibition of daytime ecosystem respiration. Nature Ecology &amp$\mathsemicolon$ Evolution 3, 407–415. https://doi.org/10.1038/s41559-019-0809-2
Kingma, D.P., Ba, J., 2014. Adam: A method for stochastic optimization. arXiv preprint arXiv:1412.6980.
Klosterman, S.T., Hufkens, K., Gray, J.M., Melaas, E., Sonnentag, O., Lavine, I., Mitchell, L., Norman, R., Friedl, M.A., Richardson, A.D., 2014. Evaluating remote sensing of deciduous forest phenology at multiple spatial scales using PhenoCam imagery. Biogeosciences 11, 4305–4320. https://doi.org/10.5194/bg-11-4305-2014
Kopf, J., Augustin, T., Strobl, C., 2013. The potential of model-based recursive partitioning in the social sciences: Revisiting ockham's razor, in: Contemporary Issues in Exploratory Data Mining in the Behavioral Sciences. Routledge, pp. 97–117.
Kucera, C., Kirkham, D.R., 1971. Soil respiration studies in tallgrass prairie in missouri. Ecology 52, 912–915.
Kuzyakov, Y., 2006. Sources of CO2 efflux from soil and review of partitioning methods. Soil Biology and Biochemistry 38, 425–448. https://doi.org/10.1016/j.soilbio.2005.08.020

Kwon, H., Ugarte, C.M., Ogle, S.M., Williams, S.A., Wander, M.M., 2017. Use of inverse modeling to evaluate CENTURY-predictions for soil carbon sequestration in US rain-fed corn production systems. PLOS ONE 12, e0172861. https://doi.org/10.1371/journal.pone.0172861

Ladha, J.K., Reddy, C.K., Padre, A.T., Kessel, C. van, 2011. Role of nitrogen fertilization in sustaining organic matter in cultivated soils. Journal of Environmental Quality 40, 1756–1766. https://doi.org/10.2134/jeq2011.0064

Lal, R., 2007. World soils and global issues. Soil and Tillage Research 97, 1–4. https://doi.org/10.1016/j.still.2007.04.002

Larionova, A., Yevdokimov, I., Kurganova, I., Sapronov, D., Kuznetsova, L., Lopes de Gerenju, V., 2003. Root respiration and its contribution to the CO2 emission from soil. Eurasian soil science 36, 173–184.

Lazcano, C., Gómez-Brandón, M., Revilla, P., Domínguez, J., 2012. Short-term effects of organic and inorganic fertilizers on soil microbial community structure and function. Biology and Fertility of Soils 49, 723–733. https://doi.org/10.1007/s00374-012-0761-7

Lee, X., Finnigan, J., others, 2004. Coordinate systems and flux bias error, in: Handbook of Micrometeorology. Springer, pp. 33–66.

Liljeroth, E., Kuikman, P., Veen, J.A.V., 1994. Carbon translocation to the rhizosphere of maize and wheat and influence on the turnover of native soil organic matter at different soil nitrogen levels. Plant and Soil 161, 233–240. https://doi.org/10.1007/bf00046394

Lin, H., 2011. Three principles of soil change and pedogenesis in time and space. Soil Science Society of America Journal 75, 2049–2070. https://doi.org/10.2136/sssaj2011.0130

Loescher, H.W., Law, B.E., Mahrt, L., Hollinger, D.Y., Campbell, J., Wofsy, S.C., 2006. Uncertainties in, and interpretation of, carbon flux estimates using the eddy covariance technique. Journal of Geophysical Research 111. https://doi.org/10.1029/2005jd006932

Luo, Y., Guan, K., Peng, J., 2018. STAIR: A generic and fully-automated method to fuse multiple sources of optical satellite data to generate a high-resolution, daily and cloud-/gap-free surface reflectance product. Remote Sensing of Environment 214, 87–99. https://doi.org/10.1016/j.rse.2018.04.042

Ma, S., He, F., Tian, D., Zou, D., Yan, Z., Yang, Y., Zhou, T., Huang, K., Shen, H., Fang, J., 2018. Variations and determinants of carbon content in plants: A global synthesis. Biogeosciences 15, 693–702. https://doi.org/10.5194/bg-15-693-2018

Mammarella, I., Kolari, P., Rinne, J., Keronen, P., Pumpanen, J., Vesala, T., 2007. Determining the contribution of vertical advection to the net ecosystem exchange at hyytiälä forest, finland. Tellus B: Chemical and Physical Meteorology 59, 900–909. https://doi.org/10.1111/j.1600-0889.2007.00306.x

Masle, J., Doussinault, G., Farquhar, G.D., Sun, B., 1989. Foliar stage in wheat correlates better to photothermal time than to thermal time. Plant, Cell & Environment 12, 235–247. https://doi.org/https://doi.org/10.1111/j.1365-3040.1989.tb01938.x

McNab, W.H., 1993. A topographic index to quantify the effect of mesoscale landform on site productivity. Canadian Journal of Forest Research 23, 1100–1107.

Medlyn, B.E., Duursma, R.A., Eamus, D., Ellsworth, D.S., Prentice, I.C., Barton, C.V.M., Crous, K.Y., Angelis, P.D., Freeman, M., Wingateton, L., 2011. Reconciling the optimal and empirical approaches to modelling stomatal conductance. Global Change Biology 17, 2134–2144. https://doi.org/10.1111/j.1365-2486.2010.02375.x

Meng, L., Ding, W., Cai, Z., 2005. Long-term application of organic manure and nitrogen fertilizer on N2O emissions, soil quality and crop production in a sandy loam soil. Soil Biology and Biochemistry 37, 2037–2045. https://doi.org/10.1016/j.soilbio.2005.03.007

Mo, J., Brown, S., Xue, J., Fang, Y., Li, Z., 2006. Response of litter decomposition to simulated n deposition in disturbed, rehabilitated and mature forests in subtropical china. Plant and Soil 282, 135–151. https://doi.org/10.1007/s11104-005-5446-7

Mo, J., Brown, S., Xue, J., Fang, Y., Li, Z., 2006. Response of litter decomposition to simulated n deposition in disturbed, rehabilitated and mature forests in subtropical china. Plant and Soil 282, 135–151. https://doi.org/10.1007/s11104-005-5446-7

Monaco, S., Hatch, D.J., Sacco, D., Bertora, C., Grignani, C., 2008. Changes in chemical and biochemical soil properties induced by 11-yr repeated additions of different organic materials in maize-based forage systems. Soil Biology and Biochemistry 40, 608–615. https://doi.org/10.1016/j.soilbio.2007.09.015

Moncrieff, J.B., Massheder, J.M., Bruin, H. de, Elbers, J., Friborg, T., Heusinkveld, B., Kabat, P., Scott, S., Soegaard, H., Verhoef, A., 1997. A system to measure surface fluxes of momentum, sensible heat, water vapour and carbon dioxide. Journal of Hydrology 188-189, 589–611. https://doi.org/10.1016/s0022-1694(96)03194-0

Morison, J.I., Gifford, R.M., 1983. Stomatal sensitivity to carbon dioxide and humidity: A comparison of two C3 and two C4 grass species. Plant physiology 71, 789–796.

Nardi, S., Morari, F., Berti, A., Tosoni, M., Giardini, L., 2004. Soil organic matter properties after 40 years of different use of organic and mineral fertilisers. European Journal of Agronomy 21, 357–367. https://doi.org/10.1016/j.eja.2003.10.006

O'Dell, D., Eash, N.S., Hicks, B.B., Oetting, J.N., Sauer, T.J., Lambert, D.M., Logan, J., Wright, W.C., Zahn, J.A., others, 2018. Reducing CO2 flux by

decreasing tillage in ohio: Overcoming conjecture with data. J. Agric. Sci 10, 1–15.
Oliveira, J. de, Epiphanio, J., Rennó, C., 2014. Window regression: A spatial-temporal analysis to estimate pixels classified as low-quality in MODIS NDVI time series. Remote Sensing 6, 3123–3142. https://doi.org/10.3390/rs6043123
Palatella, L., Rana, G., Vitale, D., 2014. Towards a flux-partitioning procedure based on the direct use of high-frequency eddy-covariance data. Boundary-Layer Meteorology 153, 327–337. https://doi.org/10.1007/s10546-014-9947-x
Papale, D., Reichstein, M., Aubinet, M., Canfora, E., Bernhofer, C., Kutsch, W., Longdoz, B., Rambal, S., Valentini, R., Vesala, T., others, 2006. Towards a standardized processing of net ecosystem exchange measured with eddy covariance technique: Algorithms and uncertainty estimation. Biogeosciences 3, 571–583.
Reichstein, M., Falge, E., Baldocchi, D., Papale, D., Aubinet, M., Berbigier, P., Bernhofer, C., Buchmann, N., Gilmanov, T., Granier, A., Grunwald, T., Havrankova, K., Ilvesniemi, H., Janous, D., Knohl, A., Laurila, T., Lohila, A., Loustau, D., Matteucci, G., Meyers, T., Miglietta, F., Ourcival, J.-M., Pumpanen, J., Rambal, S., Rotenberg, E., Sanz, M., Tenhunen, J., Seufert, G., Vaccari, F., Vesala, T., Yakir, D., Valentini, R., 2005a. On the separation of net ecosystem exchange into assimilation and ecosystem respiration: Review and improved algorithm. Global Change Biology 11, 1424–1439. https://doi.org/10.1111/j.1365-2486.2005.001002.x
Reichstein, M., Falge, E., Baldocchi, D., Papale, D., Aubinet, M., Berbigier, P., Bernhofer, C., Buchmann, N., Gilmanov, T., Granier, A., others, 2005b. On the separation of net ecosystem exchange into assimilation and ecosystem respiration: Review and improved algorithm. Global change biology 11, 1424–1439.
Reu, J.D., Bourgeois, J., Bats, M., Zwertvaegher, A., Gelorini, V., Smedt, P.D., Chu, W., Antrop, M., Maeyer, P.D., Finke, P., Meirvenne, M.V., Verniers, J., Crombé, P., 2013. Application of the topographic position index to heterogeneous landscapes. Geomorphology 186, 39–49. https://doi.org/10.1016/j.geomorph.2012.12.015
Roerink, G.J., Menenti, M., Verhoef, W., 2000. Reconstructing cloudfree NDVI composites using fourier analysis of time series. International Journal of Remote Sensing 21, 1911–1917. https://doi.org/10.1080/014311600209814
Ross, Andrew.N., Grant, E.R., 2015. A new continuous planar fit method for calculating fluxes in complex, forested terrain. Atmospheric Science Letters 16, 445–452. https://doi.org/10.1002/asl.580
Ross, Andrew.N., Grant, E.R., 2015. A new continuous planar fit method for calculating fluxes in complex, forested terrain. Atmospheric Science Letters 16, 445–452. https://doi.org/10.1002/asl.580

Rossi, R.E., Dungan, J.L., Beck, L.R., 1994. Kriging in the shadows: Geostatistical interpolation for remote sensing. Remote Sensing of Environment 49, 32–40. https://doi.org/10.1016/0034-4257(94)90057-4
Roy, D.P., Zhang, H.K., Ju, J., Gomez-Dans, J.L., Lewis, P.E., Schaaf, C.B., Sun, Q., Li, J., Huang, H., Kovalskyy, V., 2016. A general method to normalize landsat reflectance data to nadir BRDF adjusted reflectance. Remote Sensing of Environment 176, 255–271. https://doi.org/10.1016/j.rse.2016.01.023
Scanlon, T.M., Sahu, P., 2008. On the correlation structure of water vapor and carbon dioxide in the atmospheric surface layer: A basis for flux partitioning. Water Resources Research 44. https://doi.org/10.1029/2008wr006932
Scanlon, T.M., Schmidt, D.F., Skaggs, T.H., 2019. Correlation-based flux partitioning of water vapor and carbon dioxide fluxes: Method simplification and estimation of canopy water use efficiency. Agricultural and Forest Meteorology 279, 107732. https://doi.org/10.1016/j.agrformet.2019.107732
Scanlon, T.M., Schmidt, D.F., Skaggs, T.H., 2019. Correlation-based flux partitioning of water vapor and carbon dioxide fluxes: Method simplification and estimation of canopy water use efficiency. Agricultural and Forest Meteorology 279, 107732. https://doi.org/10.1016/j.agrformet.2019.107732
Schmitt, M., Zhu, X.X., 2016. Data fusion and remote sensing: An ever-growing relationship. IEEE Geoscience and Remote Sensing Magazine 4, 6–23. https://doi.org/10.1109/mgrs.2016.2561021
Srivastava, N., Hinton, G., Krizhevsky, A., Sutskever, I., Salakhutdinov, R., 2014. Dropout: A simple way to prevent neural networks from overfitting. Journal of Machine Learning Research 15, 1929–1958.
Swift, R.S., 2001. SEQUESTRATION OF CARBON BY SOIL. Soil Science 166, 858–871. https://doi.org/10.1097/00010694-200111000-00010
Swift, R.S., 2001. SEQUESTRATION OF CARBON BY SOIL. Soil Science 166, 858–871. https://doi.org/10.1097/00010694-200111000-00010
Thomas, C., Martin, J.G., Goeckede, M., Siqueira, M.B., Foken, T., Law, B.E., Loescher, H.W., Katul, G., 2008. Estimating daytime subcanopy respiration from conditional sampling methods applied to multi-scalar high frequency turbulence time series. Agricultural and Forest Meteorology 148, 1210–1229. https://doi.org/10.1016/j.agrformet.2008.03.002
Tibshirani, R.J., Efron, B., 1993. An introduction to the bootstrap. Monographs on statistics and applied probability 57, 1–436.
Tilman, D., Balzer, C., Hill, J., Befort, B.L., 2011. Global food demand and the sustainable intensification of agriculture. Proceedings of the National Academy of Sciences 108, 20260–20264. https://doi.org/10.1073/pnas.1116437108

Tu, T.-M., Su, S.-C., Shyu, H.-C., Huang, P.S., 2001. A new look at IHS-like image fusion methods. Information fusion 2, 177–186.
Verger, A., Baret, F., Weiss, M., Kandasamy, S., Vermote, E., 2013. The CACAO method for smoothing, gap filling, and characterizing seasonal anomalies in satellite time series. IEEE Transactions on Geoscience and Remote Sensing 51, 1963–1972. https://doi.org/10.1109/tgrs.2012.2228653
Vermote, E., Wolfe, R., 2015. MOD09GQ MODIS/terra surface reflectance daily L2G global 250m SIN grid V006. https://doi.org/10.5067/MODIS/MOD09GQ.006
Vickers, D., Mahrt, L., 1997. Quality control and flux sampling problems for tower and aircraft data. Journal of Atmospheric and Oceanic Technology 14, 512–526. https://doi.org/10.1175/1520-0426(1997)014<0512:qcafsp>2.0.co;2
Vitousek, P.M., Aber, J.D., Howarth, R.W., Likens, G.E., Matson, P.A., Schindler, D.W., Schlesinger, W.H., Tilman, D.G., 1997. Human alteration of the global nitrogen cycle: Sources and consequences. Ecological applications 7, 737–750.
Vose, J.M., Elliott, K.J., Johnson, D.W., Walker, R.F., Johnson, M.G., Tingey, D.T., 1995. Effects of elevated CO2 and n fertilization on soil respiration from ponderosa pine (pinus ponderosa) in open-top chambers. Canadian Journal of Forest Research 25, 1243–1251.
Wang, C., Guo, L., Li, Y., Wang, Z., 2012. Systematic comparison of C3 and C4 plants based on metabolic network analysis. BMC Systems Biology 6, S9. https://doi.org/10.1186/1752-0509-6-s2-s9
Webb, E.K., Pearman, G.I., Leuning, R., 1980. Correction of flux measurements for density effects due to heat and water vapour transfer. Quarterly Journal of the Royal Meteorological Society 106, 85–100. https://doi.org/10.1002/qj.49710644707
Wesely, M.L., 1970. Eddy correlation measurements in the atmospheric surface layer over agricultural crops. The University of Wisconsin-Madison.
Wilczak, J.M., Oncley, S.P., Stage, S.A., 2001. Sonic anemometer tilt correction algorithms. Boundary-Layer Meteorology 99, 127–150.
Wutzler, T., Lucas-Moffat, A., Migliavacca, M., Knauer, J., Sickel, K., Šigut, L., Menzer, O., Reichstein, M., 2018. Basic and extensible post-processing of eddy covariance flux data with REddyProc. Biogeosciences 15, 5015–5030. https://doi.org/10.5194/bg-15-5015-2018
Xu, L., Baldocchi, D.D., Tang, J., 2004. How soil moisture, rain pulses, and growth alter the response of ecosystem respiration to temperature. Global Biogeochemical Cycles 18, n/a–n/a. https://doi.org/10.1029/2004gb002281
Zeeman, M.J., Tuzson, B., Emmenegger, L., Knohl, A., Buchmann, N., Eugster, W., 2009. Conditional CO&amp$\mathsemicolon$lt$\mathsemicolon$sub&amp$\mathsemicolon$gt$\mathsemicolon$2&amp$\mathsemicolon$lt$\mathsemicolon$/sub&a

mp$\mathsemicolon$gt$\mathsemicolon$ flux analysis of a managed grassland with the aid of stable isotopes. https://doi.org/10.5194/bgd-6-3481-2009
Zeileis, A., 2006. Object-oriented computation of sandwich estimators. Journal of Statistical Software 16, 1–16. https://doi.org/10.18637/jss.v016.i09
Zeileis, A., Hornik, K., 2007. Generalized m-fluctuation tests for parameter instability. Statistica Neerlandica 61, 488–508. https://doi.org/10.1111/j.1467-9574.2007.00371.x
Zeileis, A., Hothorn, T., Hornik, K., 2008. Model-based recursive partitioning. Journal of Computational and Graphical Statistics 17, 492–514. https://doi.org/10.1198/106186008x319331
Zeileis, A., Hothorn, T., Hornik, K., 2008. Model-based recursive partitioning. Journal of Computational and Graphical Statistics 17, 492–514. https://doi.org/10.1198/106186008x319331
Zhang, H.H., Poissant, L., Xu, X., Pilote, M., Beauvais, C., Amyot, M., Garcia, E., Laroulandie, J., 2006. Air-water gas exchange of mercury in the bay saint françois wetlands: Observation and model parameterization. Journal of Geophysical Research: Atmospheres 111.
Zhu, Y., Kang, E., Bo, Y., Tang, Q., Cheng, J., He, Y., 2015. A robust fixed rank kriging method for improving the spatial completeness and accuracy of satellite SST products. IEEE Transactions on Geoscience and Remote Sensing 53, 5021–5035. https://doi.org/10.1109/tgrs.2015.2416351

VITA

Joel Oetting was born in 1992 in Honolulu, HI. He attended the University of Tennessee-Knoxville and graduated with an undergraduate degree in environmental soil science.